Spectroscopic measurement of volatile organic compounds as biomarkers for human breath analysis

(Article begins on next page)

19 January 2025

Politecnico di Bari

LIBERATORIA PER L'ARCHIVIAZIONE DELLA TESI DI DOTTORATO

Al Magnifico Rettore
del Politecnico di Bari

Il sottoscritto Paciolla Francesco nato a Bari il 04/11/1997

residente a Bari in via G. Zanardelli 63/F a Bari e-mail francesco.paciolla@poliba.it

iscritto al 3° anno di Corso di Dottorato di Ricerca in INDUSTRIA 4.0 ciclo XXXVII

ed essendo stato ammesso a sostenere l'esame finale con la prevista discussione della tesi dal titolo:

"SPECTROSCOPIC MEASUREMENT OF VOLATILE ORGANIC COMPOUNDS AS BIOMARKERS FOR HUMAN BREATH ANALYSIS"

DICHIARA

1) di essere consapevole che, ai sensi del D.P.R. n. 445 del 28.12.2000, le dichiarazioni mendaci, la falsità negli atti e l'uso di atti falsi sono puniti ai sensi del codice penale e delle Leggi speciali in materia, e che nel caso ricorressero dette ipotesi, decade fin dall'inizio e senza necessità di nessuna formalità dai benefici conseguenti al provvedimento emanato sulla base di tali dichiarazioni;
2) di essere iscritto al Corso di Dottorato di ricerca INDUSTRIA 4.0 ciclo XXXVII, corso attivato ai sensi del *"Regolamento dei Corsi di Dottorato di ricerca del Politecnico di Bari"*, emanato con D.R. n.286 del 01.07.2013;
3) di essere pienamente a conoscenza delle disposizioni contenute nel predetto Regolamento in merito alla procedura di deposito, pubblicazione e autoarchiviazione della tesi di dottorato nell'Archivio Istituzionale ad accesso aperto alla letteratura scientifica;
4) di essere consapevole che attraverso l'autoarchiviazione delle tesi nell'Archivio Istituzionale ad accesso aperto alla letteratura scientifica del Politecnico di Bari (IRIS-POLIBA), l'Ateneo archivierà e renderà consultabile in rete (nel rispetto della Policy di Ateneo di cui al D.R. 642 del 13.11.2015) il testo completo della tesi di dottorato, fatta salva la possibilità di sottoscrizione di apposite licenze per le relative condizioni di utilizzo (di cui al sito http://www.creativecommons.it/Licenze), e fatte salve, altresì, le eventuali esigenze di "embargo", legate a strette considerazioni sulla tutelabilità e sfruttamento industriale/commerciale dei contenuti della tesi, da rappresentarsi mediante compilazione e sottoscrizione del modulo in calce (Richiesta di embargo);
5) che la tesi da depositare in IRIS-POLIBA, in formato digitale (PDF/A) sarà del tutto identica a quelle **consegnate**/inviate/da inviarsi ai componenti della commissione per l'esame finale e a qualsiasi altra copia depositata presso gli Uffici del Politecnico di Bari in forma cartacea o digitale, ovvero a quella da discutere in sede di esame finale, a quella da depositare, a cura dell'Ateneo, presso le Biblioteche Nazionali Centrali di Roma e Firenze e presso tutti gli Uffici competenti per legge al momento del deposito stesso, e che di conseguenza va esclusa qualsiasi responsabilità del Politecnico di Bari per quanto riguarda eventuali errori, imprecisioni o omissioni nei contenuti della tesi;
6) che il contenuto e l'organizzazione della tesi è opera originale realizzata dal sottoscritto e non compromette in alcun modo i diritti di terzi, ivi compresi quelli relativi alla sicurezza dei dati personali; che pertanto il Politecnico di Bari ed i suoi funzionari sono in ogni caso esenti da responsabilità di qualsivoglia natura: civile, amministrativa e penale e saranno dal sottoscritto tenuti indenni da qualsiasi richiesta o rivendicazione da parte di terzi;
7) che il contenuto della tesi non infrange in alcun modo il diritto d'Autore né gli obblighi connessi alla salvaguardia di diritti morali od economici di altri autori o di altri aventi diritto, sia per testi, immagini, foto, tabelle, o altre parti di cui la tesi è composta.

Luogo e data BARI, 13/12/2024   Firma *Francesco Paciolla*

Il sottoscritto, con l'autoarchiviazione della propria tesi di dottorato nell'Archivio Istituzionale ad accesso aperto del Politecnico di Bari (POLIBA-IRIS), pur mantenendo su di essa tutti i diritti d'autore, morali ed economici, ai sensi della normativa vigente (Legge 633/1941 e ss.mm.ii.),

CONCEDE

- al Politecnico di Bari il permesso di trasferire l'opera su qualsiasi supporto e di convertirla in qualsiasi formato al fine di una corretta conservazione nel tempo. Il Politecnico di Bari garantisce che non verrà effettuata alcuna modifica al contenuto e alla struttura dell'opera.
- al Politecnico di Bari la possibilità di riprodurre l'opera in più di una copia per fini di sicurezza, back-up e conservazione.

Luogo e data BARI, 13/12/2024   Firma *Francesco Paciolla*

Department of Electrical and Information Engineering
ELECTRICAL AND INFORMATION ENGINEERING
INDUSTRY 4.0 Ph.D. Program
SSD: PHYS-03/A – MATERIAL PHYSICS

Final Dissertation

SPECTROSCOPIC MEASUREMENT OF VOLATILE ORGANIC COMPOUNDS AS BIOMARKERS FOR HUMAN BREATH ANALYSIS

by

Paciolla Francesco:

Supervisors:

Prof. PATIMISCO Pietro

Prof. AMOROSO Nicola

Prof. PASCUZZI Simone

Coordinator of Ph.D. Program:

Prof. ssa Ciminelli Caterina

Course n°37, 01/11/2021-31/10/2024

Politecnico di Bari

Department of Electrical and Information Engineering
ELECTRICAL AND INFORMATION ENGINEERING
INDUSTRY 4.0 Ph.D. Program
SSD: PHYS-03/A – MATERIAL PHYSICS

Final Dissertation

SPECTROSCOPIC MEASUREMENT OF VOLATILE ORGANIC COMPOUNDS AS BIOMARKERS FOR HUMAN BREATH ANALYSIS

by

Francesco Paciolla:

Referees:

Prof. BORRI Simone

Prof. ssa VICET Aurore

Supervisors:

Prof. PATIMISCO Pietro

Prof. AMOROSO Nicola

Prof. PASCUZZI Simone

Coordinator of Ph.D Program:

Prof. ssa Ciminelli Caterina

Course n°37, 01/11/2021-31/10/2024

Acknowledgements

Abstract

BTEX compounds - benzene, toluene, ethylbenzene, and xylenes - are among the most hazardous Volatile Organic Compounds (VOCs), thus their highly sensitive and selective detection can provide key information in many applications, ranging from environmental monitoring to breath analysis. Optical sensors based on laser absorption spectroscopy (LAS) techniques can represent a viable solution for BTEX detection since these compounds show strong and distinct absorption features in the spectral region 13 - 15 μm. Among these techniques, Quartz-Enhanced Photoacoustic Spectroscopy (QEPAS) and Light-Induced Thermoelastic Spectroscopy (LITES) represent two effective techniques. The research activity carried out during my Ph.D. program in Industry 4.0 at the Polytechnique University of Bari was focused on the development of optical sensors based on QEPAS and LITES techniques for benzene detection, targeting the absorption band centred at $14.85\ \mu m$ using a non-commercial Quantum Cascade Laser (QCL) source. The developed QEPAS and LITES sensors showed an excellent linear response and estimated minimum detection limits (MDL) of $13\ ppb$ and 105 ppb, respectively, were obtained with a lock-in time constant of $100\ ms$.

Summary

Introduction

Volatile Organic Compounds (VOCs) are a wide class of chemical compounds characterized by their high volatility at room temperature and standard atmospheric pressure. Within this group, the BTEX compounds - benzene, toluene, ethylbenzene, and xylenes - have been extensively studied due to their widespread production and use in industrial processes, transportation, and several other applications. BTEX compounds have been identified as important contributors to air pollution with serious risks to both human health and the environment. Among them, benzene is classified as a human carcinogen, and prolonged exposure to it has been linked to various diseases, including leukaemia, neurological diseases, and respiratory illnesses. BTEX compounds are often present in trace amounts, ranging from part-per millions (ppm) to part-per-billion (ppb) or even lower, making highly sensitive and specific detection methods essential for their accurate detection and monitoring.

BTEX analysis has conventionally relied on well-established analytical techniques, such as the combination of gas chromatography and mass spectrometry, which is regarded as the gold standard technique. While this method offers high accuracy and sensitivity, it has limitations, including slow-response time, large instrumental footprint, and the need for skilled operators. To overcome these challenges, different kinds of sensors, including nonselective chemical sensors, electronic noses and sensors based on other analytical techniques have been developed. However, the stability, lifetime, and performances of these sensors are significantly affected by environmental conditions as well as hysteresis and cross-interferences from non-target molecules.

Optical detection techniques based on laser absorption spectroscopy (LAS) represent a viable solution for trace gas detection, being able to provide a real time response with high selectivity and sensitivity. The selectivity is provided by laser sources with emission wavelengths resonant with energetic transitions of the target molecules. Among LAS techniques, Quartz-Enhanced Photoacoustic Spectroscopy (QEPAS) and Light-Induced Thermoelastic Spectroscopy (LITES) represent two effective techniques. QEPAS technique is based on the detection of acoustic waves generated by the absorption of modulated laser light in a specific target gas, using a Quartz Tuning Fork (QTF) as piezoelectric transducer. On the other hand, the LITES technique exploits the thermo-elastic conversion occurring when modulated laser light, after passing through an absorption cell containing the target gas, is focused directly onto the QTF surface.

In the context of BTEX analysis, the advent of commercial laser sources in the mid-IR allowed the exploration of the spectral window around 3.3 μm. However, this region is marked by poor

selectivity due to the spectral overlapping absorption features of many hydrocarbons. To address this issue, a shift to longer wavelength in the spectral region 13 μm - 15 μm is strongly recommended, where BTEX compounds exhibit strong and distinct absorption features. Despite the potential of this spectral region, research has been constrained by the absence of suitable laser sources and the limited performance of commercial detectors. Recently, advancements in InAs-based technology have led to the development long wavelength Quantum Cascade Lasers (QCLs) capable to cover the spectral range beyond 10 μm, allowing the development of highly performant optical sensors operating in this region.

During my Ph.D. program in Industry 4.0 at the Polytechnique University of Bari, my research, conducted at Polysense Laboratories, was focused on the development of optical sensors based on QEPAS and LITES techniques for the detection of benzene employing a custom-made QCL emitting at $\lambda = 14.85\ \mu m$ fabricated at University of Montpellier.

The thesis work is organized as follows:

- Chapter 1 provides an overview of VOCs and BTEX compounds, outlining their sources and the key applications in VOCs detection. The state of the art of the analytical detection techniques and the most employed optical techniques for VOCs detection are also discussed.

- Chapter 2 delves into the principles of QEPAS and LITES techniques. For QEPAS technique, the resonance properties of the fundamental flexural mode of a quartz tuning fork, together with the wavelength modulation detection technique, are described. For LITES technique, the use of the QTF as infrared photodetector and its thermo-elastic properties are fully covered.

- Chapter 3 begins by detailing the selected benzene absorption features. It then provides an in-depth description of the components used in the QEPAS and LITES experimental setups for benzene detection.

- Chapter 4 presents the results of the developed QEPAS and LITES sensors for benzene detection. This includes a full characterization of the QCL as well as the resonance properties of the QTF, along with the optimization of the operating parameters, sensors calibration, and long-term stability analysis for both sensors. The chapter concludes with a discussion of potential future developments, including the integration of a portable QEPAS sensor onto a mobile rover.

Chapter 1:
Volatile Organic Compounds detection

1.1 Description of VOCs

1.1.1 What are VOCs

Volatile Organic Compounds (VOCs) are chemical compounds with high vapor pressure at room temperature and standard atmospheric pressure. This property allows them to readily evaporate into a gaseous phase at room temperature (Wolkoff, 1995). The legal definition of VOC in the European Union is given in the Solvent Emissions Directive (SED 1999/13/EC), which has been later included into the Industrial Emission Directive (IED 2010/75/EU) and defines a VOC as: "any organic compound as well as the fraction of creosote, having at $293.15\,K$ a vapour pressure of $0.01\,kPa$ or more, or having a corresponding volatility under the particular conditions of use" (Ojala et al., 2011). The European Directive 2004/42 gives a slightly different definition, based on their boiling point and defines a VOC as: "any organic compound having an initial boiling point of $250\,°C$ or less, measured at a standard pressure of $101.3\,kPa$" (Anand et al., 2014). VOCs are emitted as gases from certain solids or liquids and include a variety of chemicals, such as aromatic hydrocarbons, alcohols, alkenes, aldehydes esters, ketones, olefins, and chlorinated VOCs with different functional groups (Williams et al., 2007). Since the volatility of a compound generally increases, lowering its boiling point temperature, organic compounds are classified by the World Health Organisation (WHO) by their volatility in three classes (Bandehali et al., 2021): very volatile organic compounds (VVOCs), with a boiling point from $<\ 0\,°C$ to $50-100\,°C$ (such as methyl chloride, propane, and butane); volatile organic compounds (VOC), with a boiling point from $50-100\,°C$ to $240-260\,°C$ (common VOCs are acetaldehyde formaldehyde, hexane, isoprene, benzene, toluene, ethylbenzene, xylenes, styrene and acetone); semi-volatile organic compounds (SVOCs), with a boiling point from $240-260\,°C$ to $380-400\,°C$ (such as pesticides).

Other important properties of VOCs include low water solubility and resistance to degradation; thus, they can persist as ground-water contaminants, have a long mean lifetime in atmosphere (can vary from hours to months) and can be transported to long distances in the environment (David et al., 2021). Moreover, since VOCs are highly radical, they can easily react with any particle or substance immediately after their emission. They rapidly undergo many physical and

chemical transformations, releasing organic and inorganic derivatives as unwanted products into the atmosphere (Talapatra et al., 2011). VOCs are rather inert lipophilic compounds capable of passing through biological membranes, with a toxicity level that depends on their biotransformation within the body. In the last decade, several studies have demonstrated that some VOCs have a strong negative impact on the environment and may have short- and long-term adverse health effects because are toxic, carcinogenic, and mutagenic to humans (Zhou et al., 2023). Nowadays, the count of novel VOCs is consistently increasing and is fundamental, for the research community as well as for government and regulatory bodies, to monitor VOCs exposure and their possible associated risks for people's health.

1.1.2 VOC sources

VOCs can be divided mainly into two categories depending on their sources: biogenic VOCs and anthropogenic VOCs (Michanowicz et al., 2022). Biogenic VOCs make up the largest part of these compounds in the atmosphere, nevertheless, anthropogenic activities have become important sources of VOCs emissions, indeed they account for about the 25% of VOCs in atmosphere. Biogenic VOCs are largely emitted by plants, but also by animals and microorganisms, and are the result of metabolic or decomposition processes. They are extremely diversified, the most common VOC produced by plants is isoprene, others are terpenoids, alcohols, and carbonyls (Kesselmeier et al., 1999). Biogenic VOCs play an important role in communications between animals and plants and in inter-plants interactions. Many of them are employed as attractants for pollinators or for plant defence against herbivory (Farré-Armengol et al., 2013). Not counting methane, an estimation of biogenic VOCs emissions is about $760\ teragrams$ ($7.6 \times 10^{11}\ kg$) of carbon per year (Sindelarova et al., 2014). The worldwide data reveal that tropical areas are the most prominent VOCs emitters, followed by extra-tropical regions.

Anthropogenic VOCs stem from domestic and industrial human activities, they are present both in indoor and outdoor environments, but their concentrations are consistently higher indoor. Petroleum and natural gas extraction, burning of fossil fuels, vehicle engine combustion exhausts (cars, trucks, motorcycles, ships, and airplanes) and industrial processes have significantly increased in the past decade and are considered the major contributors of anthropogenic VOCs (Friedrich et al., 1999). These activities primarily emit aromatic, alkane, and alkene-based derivatives, aliphatic and aromatic hydrocarbon-based petrochemicals VOCs. Other important sources of anthropogenic VOCs are chemical processes (manufacturing of

colour paints, lubricants, adhesives, oil derivatives), mining, cleaning supplies, plastic production, tobacco smoke, decomposition of biological and non-biological wastes, gas leaks, and use of pesticides in agriculture. An estimation of anthropogenic VOCs emissions is about 142 $teragrams$ ($1.42 \times 10^{11}\ kg$) of carbon per year (Goldstein et al., 2007).

1.1.3 BTEX group

BTEX is a commonly monitored group of VOCs which include Benzene, Toluene, Ethylbenzene and Xylenes. BTEX compounds are aromatic hydrocarbons that are considered the most harmful compounds among the VOCs (Chauchan et al., 2014). These compounds can be found in indoor and outdoor environments, but their levels are typically greater in indoor environments because they tend to accumulate. BTEX detection and monitoring provide a well-rounded picture of VOCs found in urban areas, hence they are employed as a reference to evaluate environmental levels of VOCs exposure (Aung et al., 2020). Their monitoring is also fundamental for safety and health applications. Photochemical reactions of BTEX pollutants can generate secondary pollutants, such as ozone and secondary aerosol via gas-to-particle conversion processes (Yang et al., 2022).

In outdoor environments, the natural sources of BTEX are mainly soil and oceans. Anthropogenic BTEX give a great indication of VOC emissions from a wide range of sources, indeed they are released into atmosphere through industrial plants, combustion of fossil fuels from vehicles, evaporation of petroleum products, processing and storage of crude oil and cigarette smoking (Rajabi et al., 2020). Moreover, BTEX compounds are largely employed by the chemical industry to prepare raw material to manufacture pesticides, plastic, synthetic fibres, solvents, paints, foundries, electronics, and pharmaceuticals (Martins et al., 2019). Current data show that the most widespread source of anthropogenic BTEX in outdoor ambient air is the burning of fuels in motor vehicles, stationary engines, and other equipment; only the $5-10\%$ of BTEX emissions in outdoor air come from non-mobile sources (Bolden et al, 2015). BTEX in indoor environments can volatilize from several products, including household cleaners, fabric and leather treatments, and paints. Further, their use in household cleaning products results in sorption to various indoor surfaces (e.g., carpets, pillows, flooring), which contributes to persistent background levels post cleaning. The molecular structures of the compounds included in the BTEX group are presented in Fig. 1.1.
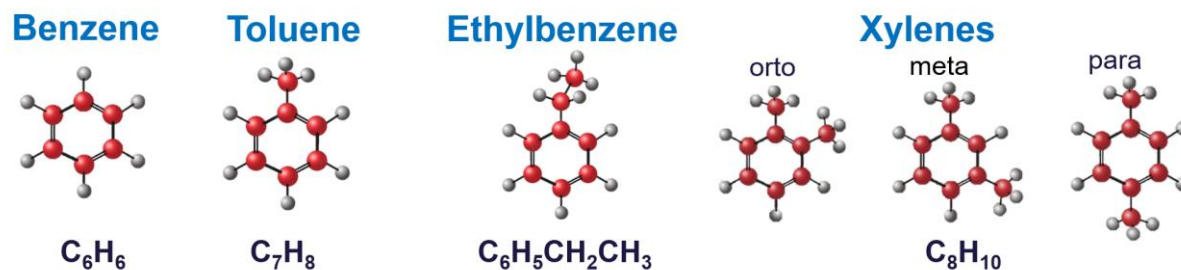
Fig. 1.1 Molecular structure of benzene, toluene, ethylbenzene, and xylenes. The red spheres represent the carbon atoms, the grey spheres the hydrogen atoms.

Benzene

Benzene (C_6H_6) is a clear, colourless, and flammable liquid with a sweet petrol-like smell. It is commonly found in ambient air because of vehicle exhausts and burning fuels, because it is added in unleaded fuel as a substitute for lead. Benzene is classified by the International Agency for Research on Cancer (IARC) as toxic and carcinogenic to humans (Group 1) and there is no safe level of exposure (Loomis et al., 2017). Prolonged exposure to high concentrations of benzene impacts blood production, the lymphatic system, and the central nervous system. The World Health Organization estimates that concentrations of $17 \, \mu g/m^3$ ($5 \, ppb$) of airborne benzene can be associated to an excess lifetime risk of leukemia of 10^{-4} (World Health Organization, 2019). Less severe health impacts can occur at lower concentrations causing narcosis, headache, dizziness, drowsiness, confusion, tremor, and loss of consciousness.

Toluene

Toluene (C_7H_8), also known as methylbenzene, is a colourless liquid, with a strong, solvent-like smell. Toluene is inexpensive and simple to produce and is widely used in industrial processes as a solvent. In non-industrial uses, toluene can be found in petrol as an octane booster and in glues, solvents, and resins. Toluene is classified as Group 3 carcinogens or non-carcinogenic by the IARC (World Health Organization, 1985). Long- term exposure to toluene can affect the reproductive and the central nervous system, but also the liver, the kidney, and the skin (Morakinyo et al., 2017).

Ethylbenzene

Ethylbenzene ($C_6H_5CH_2CH_3$) is a colourless liquid, with a petrol-like aroma. Ethylbenzene is widely used in industrial processes for the manufacture of styrene, which is then employed for polystyrene manufacture; it is also used as a solvent in inks, dyes and in petrol. Ethylbenzene is recognized as a potential carcinogen by the IARC (Group 2B) (Henderson et al., 2007).

Xylenes

Xylenes (C_8H_{10}) comprise three isomers of dimethyl benzene: m-xylene, p-xylene, and o-xylene. Usually, their concentrations are summed up as total xylenes. Xylenes is refined from crude oil and is widely employed in production of plastic bottles, polyester clothing and as a solvent in a wide range of applications, from circuit board cleaning to thinning paints and varnishes. Xylenes is classified as Group 3 carcinogens or non-carcinogenic by the IARC, but long-term exposure to xylenes at a low level can cause fatigue, tremor, nervous system, respiratory, kidney and cardiovascular-related problems (Sarigiannis et al., 2011).

BTEX are commonly found in blood but also in exhaled breath of men, children, pregnant women, and people who are occupationally exposed (Montero-Montoya et al., 2018). Several studies have detected and quantified the level of BTEX in indoor and outdoor air samples of people of different ages and countries (Ghaffari et al., 2021). It is important to highlight that prolonged exposure of professionals who work with paints, glues and solvents is one of the major factors in the deterioration of workers' health (Nordling Nilson et al., 2007). BTEX compounds are considered the most hazardous pollutants among VOCs, thus their highly sensitive and selective detection can provide key information in many fields of application, such as environmental monitoring and breath analysis.

1.2   Applications of VOC detection

1.2.1 Environmental Monitoring

The rapid development of industrialization and the ongoing global warming have significantly increased VOCs emissions. These factors give a significant contribution to atmospheric ozone formation, acid deposition, organic aerosol formation, and photochemical smog formation in atmosphere, contributing to the increasing pollution rate and climate changes (Bauguitte et al., 2010). The light-assisted chemical reactions of VOCs principally take place with carbon dioxide, nitric oxide, and even with many other VOCs. Chemical transformations of VOCs lead to the production of highly reactive volatile substances. Since many studies have related allergic, carcinogenic, mutagenic, and toxic properties of many VOCs to some diseases, it is imperative to monitor the impact of exposure to these compounds, both in indoor and outdoor environments, to ensure a better quality of life. Their impact depends on the class of the compound, time and level of exposure and type of environment. Up to now, the United States Environmental Protection Agency (USEPA) has classified about 189 air pollutants, 97 being VOCs (David et al., 2021). The analysis and characterization of VOCs play a crucial role in environmental monitoring for the evaluation of air quality and the identification of sources of pollution and chemicals in consumer products.

The correct evaluation of outdoor and indoor air quality is not an easy task because air is a quite complicated system, subjected to changes even in a short period of time. VOCs constitute an important fraction of gaseous outdoor pollutants over urbanized areas, in particular BTEX compounds comprises over 60% of the found VOCs. In residential areas bordered by manufacturing industries, BTEX monitoring is useful for assessing the impact of industries on air quality of the surrounding communities. In 2020 in China during the Covid 19 pandemic a scientific study, which performed the assessment of the concentration of several commonly found VOCs, was carried out. In that period, traffic on roads was significantly limited and the functioning of hundreds of industrial plants was temporarily halted. The study found that the concentration of over thirty VOCs was reduced to the half during the lockdown period compared to the concentration before Covid pandemic, highlighting as industrial processes and vehicles' exhaust gases are important sources of VOCs in outdoor environments (Jensen et al., 2021).

Regarding indoor environments, the WHO has recognized VOCs as the most important pollutants of indoor air. Harmless air is defined as the one in which the total content of VOCs is lower than 100 g/m^3. Among about 500 identified VOCs in indoor air, only few of them

have been proved pathogenic. Many of them are contributors to symptoms as: allergies, headaches, loss of concentration, drying and irritation of mucous membrane of nose, throat, and eyes (World Health Organization, 2000). The set of such symptoms is named "Sick Building Syndrome". Indoor air quality strongly depends on indoor emitters such as construction materials, finishing products (colour paints, primers, varnish), burning processes, tobacco smoking and cleaning products (Joshi, 2008).

People who live in Central Europe spend most of their lifetime indoor, indeed a statistic adult spends about 80% of their life at home, workplace, school, restaurant, cinema, public transport; elder people and children spent even more time. Hence, even relatively low concentrations of VOCs can constitute health hazard due to long time of exposure. VOCs emissions in indoor environments have a multi-exponential decay trend, with the most volatile compounds decaying with a time-constant of a few days, and the least volatile compounds decaying with a time-constant of a few years (Holøs et al., 2019). A scientific study carried out by Wang et al. in 2020 showed strong seasonal variations in indoors VOC emissions, with increasing rates especially in summer.

VOCs are substantially present not only in air but also in other environmental sources, including soil and water. Several reports from toxicological societies are concerned about the toxic levels of VOCs in drinking water and river water (Jin et al., 2022). This type of contamination not only impacts on ecological sources, but also affects humans when frequently exposed. In 2021, an Italian research team attempted to find out whether the imposition of lockdown during the Covid 19 pandemic resulted in the improvement of seawater quality of the Lagoon of Venice (Cecchi, 2021). Before the lockdown period about 40 VOCs were detected in seawater samples, whereas the analysis of the samples collected after the lockdown revealed the presence of only 17 VOCs and their concentrations were lower compared to the previous levels. This study highlighted as mass tourism increases marine litter, water traffic emissions, and solid waste release contaminants into the seawater.

VOCs are a wide and heterogeneous class of compounds which include multiple chemicals such as aromatic hydrocarbons, alcohols, alkenes, aldehydes esters, ketones, olefins, and chlorinated VOCs. The most representative VOCs found in the environment for each category, with their sources and the associated environmental impact are presented in Tab. 1.1. This list is compiled from all literature references cited in this paragraph.

Tab. 1.1 Most representative compounds for each VOC category, with the associated sources and their environmental impact.

Category	Representative VOCs	Source	Environmental impact
Alkane	- Methane - Butane - Hexane	Part-combusted gas Fuel addictive Refrigerant solvent Gasoline consumption	Greenhouse gas Marine ecological damage Haze
Alcohol	- Methanol - Ethanol	Petrochemical derivative Cosmetics Pharmaceuticals	Large amounts of waste water and gas during production Photochemical smog
Aldehyde Esters	- Formaldehyde - Acetaldehyde	Building and decorative materials Cosmetics decomposition	Predecessor of ozone Detrimental to vegetation
Olefins	- Ethylene - Isoprene	Petrochemical derivative Product of perfumes and Pharmaceutical	Photochemical ozone Water and soil pollution
BTEX	- Benzene - Toluene - Ethylbenzene - Xylenes	Petroleum products Part-combusted liquid fuels Adhesives Production of paints	Photochemical smog Damage the ozone layer Marine ecological damage
CI-VOCs	- Carbon Tetrachloride - Chlorobenzene - Tetrachloroethane - Trichloroethylene	Solvent Insecticide Dye industry Pharmaceutical Adhesives Sewage disposal	Damage of the ozone layer Cause greenhouse gas
Ketones	- Acetone	Paints, Cleaning agents, Diluents	Oxygen depletion in aquatic system

Alkanes, alcohols, olefins and BTEX are largely emitted by vehicles' exhausts and petrochemical products and are VOCs mostly found in outdoor environments. Their environmental impact is mainly related to the formation of photochemical smog and greenhouse gases. On the other hand, aldehyde esters, CI-VOCs and ketone are mostly associated to indoor environments, indeed they are generated mainly by building materials, paints, cleaning agents and cosmetic products. Their environmental influence includes ozone formation, detrimental to

vegetation, water and soil pollution and oxygen depletion in aquatic systems.

Nowadays, several countries and organizations, such as the National Institute of Occupational Safety and Health (NIOSH) and the Occupational Safety and Health Administration (OSHA), have started to set more stringent legislations and regulations for exposure limits to harmful VOCs. The established exposure limits to different VOCs are summarized in Tab. 1.2 (Khan et al., 2020).

Tab. 1.2 Established exposure limits of different VOCs based on limit values imposed by the National Institute of Occupational Safety and Health (NIOSH), the Occupational Safety and Health Administration (OSHA) and the American Conference of Governmental and Industrial Hygienists (ACGIH).

Compound	NIOSH-Recommended Exposure Limit (ppm)[a]	OSHA-Permissible Exposure Limit (ppm)[b]	ACGIH-Threshold Limit Value (ppm)[c]
Benzene	0.1	1	0.5
Toluene	100	200	20
Ethylbenzene	10	10	10
Xylene	100	100	100
Formaldehyde	0.016	0.75	0.3
Acetone	250	1000	250
Ethanol	1000	1000	1000
Methanol	200	200	250

[a] Recommended exposure limit, it is an exposure limit for 8 or 10-hr time-weighted average.

[b] Permissible exposure limit expressed as a time-weighted average; the concentration of a substance to which most workers can be exposed without adverse effect averaged over a normal 8-hr workday or a 40-hr workweek.

[c] Threshold limit value expressed as a time-weighted average; the concentration of a substance to which most workers can be exposed without adverse effects.

The effects of long-term exposure to BTEX compounds are described in detail in Section 1.1.3. Formaldehyde is widely employed in industry due to its high reactivity and low cost, but it is toxic and allergenic (Talaiekhozani et al., 2013). High-level exposure to formaldehyde can cause nasopharyngeal cancer and can damage cells and tissues. Inhalation of acetone is associated with headache, dizziness, and dermatitis (Wigaeus et al., 1981). Long-term ethanol and methanol exposure can cause nausea, abdominal pain, shortness of breath and dizziness (Moon, 2017).

1.2.2 Breath Analysis

Human exhaled breath consists largely of nitrogen (74%), oxygen (reduced from 21% inhaled to about 15% exhaled), carbon dioxide (4%-5%), inert gases (0.9%) and water vapor (saturated at $37\,°C$, about 6%) (Das et al., 2017). The residue consists of a mixture of more than 3500 VOCs with concentrations in the range of parts per million (ppm) to parts per trillion (ppt) by volume (Popov, 2011). Many of them are systemic or endogenous, being produced in physiological processes, but the metabolic routes behind their production are known only for few of them. Other VOCs are exogenous and result from external contaminations, through inhaled air or ingested foods or drinks. These are considered as pollution or background noise (Pereira et al., 2015). Exhaled breath contains inorganics VOCs such as nitric oxide $(10-50\,ppb)$, nitrous oxide $(1-20\,ppb)$, ammonia $(0.5-2\,ppm)$, carbon monoxide $(0-6\,ppm)$, hydrogen sulphide $(0-1.3\,ppm)$ and organic VOCs such as acetone $(0.3-1\,ppm)$, ethanol $(\sim 100\,ppb)$, isoprene $(\sim 105\,ppb)$, ethane $(0-10\,ppb)$, methane $(2-10\,ppm)$, pentane $(0-10\,ppb)$ (Das et al., 2020; Lindinger et al., 1997).

Breath analysis is one of the oldest forms of diagnosis, indeed this technique was used since the time of Hippocrates as indicator of several diseases because the exhaled breath could be characterized by a distinctive smell, given by the combination of the present VOCs (Dent et al., 2013). These intuitive observations were later proved by using classical analytical methods. In 1971 Linus Pauling demonstrated that breath is a complex gas containing no less than 200 VOCs, marking the beginning of the modern breath testing (Pauling et al., 1971).

The inhaled air goes into the alveoli in the lungs, where the metabolic excretable products diffuse into the inhaled air, which is then rejected in form of exhaled air. The exhaled air carries the fingerprint of metabolic processes going on endogenously, becoming a rich source for disease diagnosis and health monitoring.

The abundance of CO_2 and water vapour in exhaled air makes breath analysis particularly challenging because water condensation interferes with the quantification of low abundant VOCs. Moreover, the influence of the subject is very pronounced because exhaled breath composition is highly dependent on metabolism and therefore on clinical characteristics of the patient such as age, gender, weight, diet, smoking habits, lifestyle and physical condition and existence of other diseases (Amann et al., 2014). To develop a diagnostic breath test, it is necessary to unravel the baseline physiological levels of VOCs present in human breath which are strictly related to the aforesaid factors. Moreover, it is important to highlight that exhaled

breath composition reflects the composition of the bloodstream, although it must be considered that some VOCs are originated in the airways, not being present in the blood.

Nowadays, traditional medical techniques for the diagnosis of diseases such as oncological diseases, diabetes and pulmonary complications are invasive, relatively expensive, and require highly skilled medical staff. In this context, breath analysis is becoming an important area of research which has gained extreme interest, owing to advances in sensing techniques. It is a non-invasive diagnostic tool for different disease, by analysing the VOCs present in the exhaled breath (Risby et al., 2015). Breath analysis has several advantages being cost-effective, rapid, and qualitative/quantitative, hence it has the potentiality of becoming a mass screening diagnostic tool capable of replacing traditional diagnostic tools. Regarding analytical aspects, there are many bottlenecks in exhaled breath analysis; the most important is the lack of standardization of experimental procedures for sampling and storage operations of the breath sample.

One of the most important and delicate steps in breath analysis is breath sampling because there are some parameters to consider for avoiding wrongful assumptions about the origin of identified compounds. Breath collection can be achieved through a single breath or multiple breaths. For breath analysis, multiple breaths method is required since it ensures a better reproducibility in terms of composition of the sample (Amann et al., 2010). Exhaled breath can be sampled in its full composition or, alternatively, considering only alveolar air. The first choice is more prone to contaminations with exogenous compounds from the oral cavity and dilutions in dead space that may compromise the analysis. In contrast, alveolar air sampling is more accurate because alveolar air is richer in volatile blood-borne compounds and gives consistent sample quality useful for subject comparisons (Miekisch et al., 2008).

Exhaled breath sampling can be performed through Tedlar® bags and canisters. The former are made from chemically inert materials and are easy to use but are vulnerable to punctures and can generate biased results. Canisters are stainless steel recipients with an electropolished inner surface. They are robust with long shelf life, but their use is not suitable for sample collection due to their costs, and storage space (Beauchamp et al., 2008).

The suitability of breath analysis for diagnostic purpose strongly depends on the sensitivity and selectivity of the methodology employed for VOCs detection and on the discriminatory ability of the test to classify patients according to the diseases affecting them. Breath analysis has the potential to assess not only the disease, but also its severity, progression, and therapeutic monitoring, although many improvements must be done at the methodological level to achieve these goals.

Table 1.3 reports the most detected VOCs in the field of breath analysis, their concentration range, some possible clinical applications and their metabolic pathway (Das et al., 2016). This list is compiled from all literature references cited in this paragraph.

Tab. 1.3 Most detected VOCs for breath analysis, their concentration range, their metabolic pathway, and possible associated diseases.

Compound	Concentration Range	Clinical Application	Metabolic Pathway
Acetaldehyde	ppb	Hepatic function, lung cancer	Ethanol metabolism
Acetone	ppb	Diabetes, lung cancer, asthma	Rise of blood sugar level and intensive lipolysis
Ammonia	ppb	Renal function, hepatic function, urea cycle disorder	Protein metabolism
Carbon dioxide	%	CO_2 production, alveolar ventilation	Respiration
Carbon monoxide	ppm	Host response to infection	Heme catabolism
Ethane	ppb	Lung cancer, pulmonary diseases	Oxidative stress
Ethanol	ppb	Gastrointestinal and liver function	Anaerobic fermentation products by gut bacteria
Hydrogen	ppm	Gastroenteric disease	Gut bacterial metabolism of carbohydrates
Isoprene	ppb	Cholesterol biosynthesis, lung cancer, renal failure	Oxidative stress
Methane	ppm	Gastrointestinal diagnose	Bacterial overgrowth
Methanol	ppb	Liver dysfunction	Anaerobic fermentation

			products by gut bacteria
Nitric oxide	ppb	Asthma, cystic fibrosis, lung cancer	Pulmonary inflammation
Isotopes of carbon (^{13}C or ^{14}C)	ppb	Duodenal ulcer, gastric cancer	Helicobacter pylori infection
Hydrocarbons (Toluene, Benzene, Octane)	ppb	Colorectal, breast, lung cancer	Lipid peroxidation

Regarding oncologic diseases, lung cancer is the world leading cause of cancer mortality, accounting for the 19% of the total cancer deaths. The diagnosis of early-stage lung cancer is critical for the life expectancy of patients, as its five-year survival is around 58% – 73% when is diagnosed in stage I. Several VOCs, such as acetaldehyde, acetone, and isoprene can be considered potential biomarkers for this type of cancer (Buszewski et al, 2012). Colorectal cancer is the second leading cause of cancer-related death in Europe. Altomare et al. in 2013 compared exhaled breath samples of patients with this type of cancer with healthy patients. The study identified 15 discriminating VOCs between the two classes of patients. Another worldwide common cause of death is gastric cancer because its diagnosis is often delayed due to the lack of defined risk factors and unspecific clinical symptoms (Mustafa et al., 2017). High levels of hydrogen, ethanol, methane, and isotopes of carbon can be considered potential biomarkers for gastric disorders (Pham et al., 2021).

Breast cancer is the most prevalent form of cancer diagnosed in women, hydrocarbons can be considered biomarkers for this kind of cancer, as well as for colorectal and lung cancer (Phillips et al., 2010).

Regarding other diseases, high levels of acetaldehyde and ammonia could be considered potential markers of renal disorder (Krishnan et al., 2017); isoprene and acetone can be directly linked to cholesterol metabolism and diabetes, respectively and their measurement can be used to monitor these diseases (Li et al., 2015). Several other pulmonary complications, such as airways inflammation, asthma, chronic obstructive pulmonary disease, and cystic fibrosis can be assessed using breath analysis (Zhou et al., 2012). Some studies reported elevated levels of acetone and nitric oxide in the exhaled breath of asthmatic patients (Hansel et al., 2003); high

ethane levels, correlated with high levels of carbon monoxide, were found in patients with cystic fibrosis and airway obstruction (Paredi et al., 2000).

Unfortunately, it is not possible to correlate a specific disease with the presence of a determined VOC in exhaled breath because only the coexistence of different VOCs in a pattern can represent a first warning sign to the patient to make more specific diagnostic tests (Dima et al., 2021).

1.3 VOCs detection techniques

1.3.1 State of the art of VOCs detection techniques

VOCs detection and quantification are challenging because they are found in very low concentrations in environment and in breath samples, hence highly sensitive and accurate sensing methods are required. Additionally, challenges related to the sampling and storage process of VOCs samples and interferences caused by matrix effects can make difficult the detection process. Different sensing techniques have been reported to detect and monitor VOCs and each of them has its advantages and shortcomings, depending upon the nature of the molecules to detect, the environment, and the application field (Khatib et al., 2022). The gold standard technique in analytical chemistry for VOCs detection is gas chromatography/mass spectrometry (GC/MS) (Langford et al., 2014). However, on-site and real-time detection of VOCs is gaining interest in many fields of research such as environmental monitoring, breath analysis, food analysis and security. For those reasons, in the last decade other methods have been studied and developed, such as nonselective chemical sensors, which include several different types of devices, Electronic Noses, compact GC and MS and sensors based on other promising techniques.

Gas Chromatography/Mass Spectrometry (GC/MS)

The combined use of GC–MS can be employed to separate volatiles within a complex mixture, structurally elucidate analytes, and quantify them in biological samples. This technique is the most widespread, however it has some challenges and limitations. Some difficulties are related to the sampling process of VOCs from gaseous and liquid headspace samples, their transport and preservation from possible contaminations. The concentration of VOCs is very low and some interfering compounds could affect the analytical results, hence in many cases a preconcentration step, to increase the concentration of the target analyte, is required. There are several available enrichment techniques, such as cryogenic trapping, adsorption in thermal desorption tubes (TD-tubes), sorbent traps and coated fibers (Ras et al., 2009). Trapped VOCs are then released from the substrate by using thermal desorption and passed to the GC/MS sample injector. The GC utilizes a capillary column, whose properties for molecule separation depend on the column's dimensions (length, diameter, film thickness) as well as phase properties. Differences in chemical properties among the molecules in a mixture and their relative affinity for the stationary phase of the column will promote the separation of the molecules as the sample travels along the column. In this way, the molecules elute from the

column at different times. This allows the MS downstream to capture, ionize, accelerate, deflect, and detect the ionized molecules using their mass-to-charge ratio. Through this process it is possible to identify and quantify the amount of each specific VOC in the sample (Sahil et al., 2011). The schematic diagram of the main components of GC–MS instruments for VOCs analysis is depicted in Fig. 1.2.
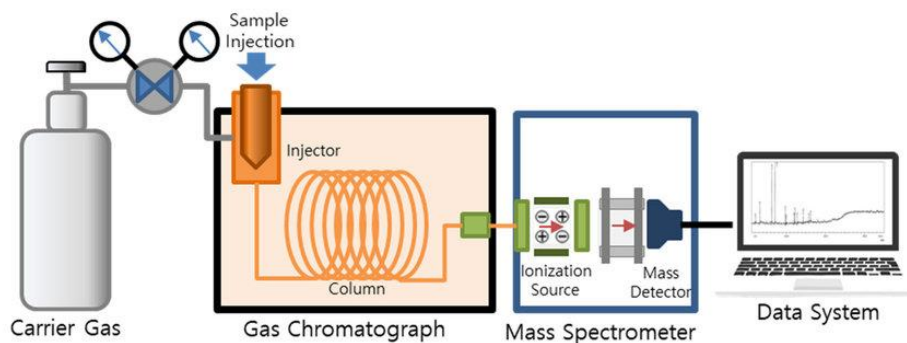

Fig. 1.2 Schematic diagram of the main components of GC–MS instruments for VOCs analysis (Kim et al., 2020).

It is important to highlight that reliable measurements using GC/MS require frequent calibrations across the measurement range. Many VOCs have been detected and quantified with this technique in several application (Wu et al., 2004). This technique is very accurate but at the same is laboratory-based, time-consuming (a typical GC-MS analysis can take up to an hour), costly and requires skilled operators (Gałuszka et al., 2015).

Nonselective Chemical Sensors

Nonselective gas sensors are mostly employed to measure the total VOCs content because, due to their nonselective nature, they can just detect their presence and concentrations but cannot speciate them (Epping et al., 2023). These sensors can provide reliable information on air quality in indoor and outdoor environments; some examples of their applications are measurement of vehicles' exhaust gases and air quality in workplaces.

The most employed types of sensors that can be included in this category are photoionization detectors, electrochemical sensors and metal oxide sensors, but there are also other sensors types available on the market.

Photoionization detectors (PID) and flame ionization detectors (FID)

The principle of functioning of photoionization sensors consists in the ionization of neutral molecules of chemical compounds. These sensors employ electrodeless ultraviolet (UV) lamps (wavelength $10 - 400\ nm$) to ionize gas molecules. The energy of the photons is enough to ionize most VOCs but not the main constituents of air, thus when VOCs molecules enter the region of impact of the UV lamp they are ionized. The formed ions are then directed between two polarized electrodes; the ions move towards these electrodes in an electric field generated by an electrometer (Szulczynski et al., 2017). In this way, an electric current is generated by the ions and is then converted into a voltage signal proportional to the concentration of the compound subjected to ionization. They are commonly used to monitor the exposure of workers to VOCs in different settings (Agbroko et al., 2018).

A flame ionization detector (FID) uses a hydrogen flame to ionize VOCs. FIDs are most known as GC detectors but can also be utilized as stand-alone instruments. The generated signal is proportional to the number of non-oxidized carbon atoms. Measurable VOCs include cyclopentane, cyclohexane, cyclooctane and VOCs in alcoholic beverages (de Blas et al.,2011).

Electrochemical (Amperometric) sensors

Electrochemical sensors (ECSs) consist of two electrodes, a working electrode suitably polarized and a reference electrode, respectively. They are in contact with a liquid electrolyte within an electrochemical cell. The working electrode is exposed to analyte particles entering the cell, either directly or through a diffusion barrier. If these particles are electrochemically active or if react with an electrolyte component, an electrochemical reaction occurs at the working electrode, giving rise to an electric current. The generated electric signal is analysed to identify the analytes composing the gas sample and retrieve their concentrations. In principle these sensors are nonselective, but an ECS can be optimized for specific analytes altering the membrane and the electrode material, the electrolyte, or the electrical state of the cell (Baranwal et al., 2022). VOCs air pollutants commonly detected by electrochemical sensors are nitrogen oxides (NO_x), sulfur oxides (SO_x), and hydrogen sulfide (H_2S) (Kumar et al., 2019).

Metal Oxide (Potentiometric) Sensors

Metal oxide sensors (MOS) are composed of a metal oxide thin film. They are the most widespread VOC sensors. In these sensors, analyte particles diffuse towards the receptor surface, which is a metal oxide (maintained at suitable temperature using a heater), where they undergo chemisorption. The process of signal generation is not fully understood but depends

on the interaction of the VOC compounds with chemisorbed oxygen contained in air on the metal oxide layer, which either liberates or removes electrons from the semiconductor surface. This interaction results in a change of resistance of the receptor element. Depending on the metal oxide, oxidizing or reducing compounds can be measured (Dey et al., 2018). Two types of metal oxide semiconductors are employed: i) N-type MOS (e.g., ZnO, SnO$_2$), that experiences an increase in conductivity interacting with reducing VOCs and a reduction in conductivity with oxidizing VOCs; ii) P-type MOS (e.g., NiO, CoO), that work in the opposite way.

The performances of these sensors can be influenced by several factors such as their composition, surface area, doping level, temperature, humidity, and morphology. Consequently, a lot of research is focused on fabrication methods and nanostructured sensors. Some VOCs detected in indoor environments with this technique include formaldehyde, benzene, and naphthalene (Leidinger et al., 2014).

Pellistors, Surface Acoustic Wave, Quartz Crystal Microbalance and Other Sensors

Other sensors that belong to the group of nonselective VOC sensors are pellistors, or thermal sensors. These sensors measure the changing resistance of a catalytically coated ceramic, while combustible volatiles move towards them by diffusion. The heat increasing due to the combustion reaction, leads to an increase in electrical resistance. Due to their nature, they are used to detect explosives.

Besides these more established and widely used sensors, there is a wide range of emerging sensors that may play a prominent role in the future. Among them, there are surface acoustic wave (SAW) sensors. In these sensors, an acoustic wave travels through an adsorbent polymer film on a piezoelectric substate. When a VOC is adsorbed onto the film, its mass increases and a small change in the phase of the propagating acoustic wave occurs. These sensors have been employed for the detection of VOCs such as acetone, ethanol, cyclohexane, and isoprene, that are considered possible biomarkers of some diseases (Ho et al., 2013).

Another class of sensors that works on a similar principle is represented by quartz crystal microbalance (QCM) sensors. A voltage is applied to a quartz crystal, causing its oscillation and the crystal is coated with a polymer film. When a VOC is adsorbed onto the film's surface, its mass changes resulting in a change in the oscillation frequency of the quartz crystal. QCM sensors have been employed to detect VOCs emitted by food-borne pathogens, mycotoxins, and pesticides (Bragazzi, 2015).

Several other sensor types can be counted towards the class of microelectromechanical systems (MEMS). The basic mechanism for all these sensors is the presence of an active layer which

interacts with the target VOC and a transduction mechanism that convert the interaction into a detectable signal. The transduction mechanism can be optical, acoustic, calorimetric, amperometry, conductometric, potentiometric or biological (Ollé et al., 2020).

Electronic Noses

Electronic Noses (ENs) or e-noses are among the most promising sensors for odor discrimination. They mimic our olfactory system and exploit the principle of sensor array; indeed, several simple and low-cost nonselective sensors are bundled together to form an array. While an individual sensor is rather nonselective, each sensor of the array has a slightly different selectivity towards a VOCs mixture. Through machine learning algorithms information obtained from the array of sensors are combined to create a fingerprint of the analysed VOCs mixture (Epping et al., 2023). These sensors are usually employed to compare VOCs samples with a reference or with each other. These devices need to be portable, low power consuming and fast in response. ENs have been employed in food safety, agriculture, military, security, medical or industrial applications (Wilson et al., 2009).

Compact GC and MS

Nowadays, there is a lot of interest in miniaturizing GC and MS instruments. "Compact" GC and MS instruments are smaller versions of lab instruments that have similar performances as their full-size equivalents, but consume less power, materials, and space. Moreover, for in-field applications, it is also necessary to cut down the complexity of operating such a system. In a compact GC system, all the main components such as injector, column, and detector, are shrunken to achieve better portability. These components are chip-based machined on silicon wafers. Traditional columns may be replaced by etched channels on a semiconductor chip or a multiple capillary column (Witkiewicz et al., 2019).

Regarding MS systems, there has been a lot of innovation in terms of ion source, but they are difficult to become portable due to the need for vacuum conditions and space to separate ions. Some prototypes of compact GC and MS systems have been developed and used to detect VOCs, including BTEX group, isoprene, and styrene useful for environmental monitoring (Sanchez et al., 2007).

Other Promising Techniques

A promising variant of MS for the analysis of VOCs is represented by the direct injection mass spectrometry (DIMS). These instruments can identify and quantify VOCs without any sample

preparation and, in some cases, even without proper calibration. In this technique, the quantitative ion generation is achieved through controlling the ionization. One advantage of this method is the measurement time (few seconds), still ensuring great selectivity and sensitivity.

Another promising technique is the ion mobility spectrometry (IMS), which can be seen as a hybrid between GC and MS. IMS uses an external electric field at ambient pressure to separate, according to their mobility, different ions formed from the target analyte. Sensors based on IMS can be used as a stand-alone method or in conjunction with GC.

Sensors based on these techniques have been employed in several applications, ranging from food analysis, biogenic VOCs monitoring, and breath analysis (Lebrón-Aguilar et al., 2016; Guo et al., 2022).

1.3.2 Comparison among different techniques

The most important criteria to compare different sensing techniques for VOCs detection are (Prichard et al., 2007):

- Sensitivity: Ratio between the sensor's output change and the input change under steady state working conditions;
- Selectivity: Ability to discriminate the target from interferent molecules, obtaining a target-specific sensor response;
- Stability: Degree to which sensor's characteristics remain constant over time, ensuring reproducibility of results;
- Operating conditions: Conditions in which the system can operate (temperature, humidity);
- Response time and frequency: Time employed to make a measure and number of measurements in a given time;
- Limit of detection (LOD): Lowest concentration of the analyte that can be detected;
- Dynamic range: Concentration range in which the technique can be applied;
- Portability: Quality of being light and small enough to be easily carried or moved;
- Cost: Cost of the device and its functioning.

Table 1.4 summarizes the most employed analytical techniques for VOCs detection, highlighting advantages and limitations for each method. The average properties of the different

presented methods are reported; these may not be true for every single device that belongs to a particular technique. This list is compiled from all literature references cited in Section 1.3.1.

Tab. 1.4 Most employed analytical techniques for VOCs detection, highlighting the advantages and the limitations for each method.

Detection Technique	Applications	Analytes	Advantages	Limitations
PID	- Industrial safety monitoring - Soil contamination - Leak detection - Emissions monitoring	VOCs with high ionization potential	- Instantaneous response - Inexpensive and simple to use - High measuring range	- Nonselective - Halogenate species not detectable
ECS	- Breath analysis - Environmental monitoring	Most VOCs	- Broadband sensors - Low costs and not affected by other gases	- Limited sensitivity and detection range - Limited temperature range and shelf life
MOS	- Urban air monitoring - Indoor air quality - Industrial measurement	Oxidizing compounds and most reducing compounds	- Small, low cost, easy to use	- Cross sensitivity of VOCs - Influenced by temperature and humidity - High working temperatures
Pellistors	- Combustible gas leak detection	Combustible volatiles	- Small and inexpensive	- Low selectivity and high LOD - Baseline drift - Sensitive to environmental conditions
SAW	- Environmental monitoring	Depends on film material on the sensor	- High sensitivity and fast response - Small and long lifetime	- Limited selectivity - Poor reproducibility - Sensitive to environmental conditions
QCM	- Industrial processes	Depends on film material	- Good sensitivity and reproducibility	- Limited selectivity

	- Food quality and safety	on the sensor	- Fast response	- Sensitive to environmental conditions - Complexity
Compact GC and MS	- Emissions monitoring - Indoor air quality	Depending on the detector	- Good selectivity and sensitivity - Portable	- Discontinuous measurement - Instrument maintenance
E-Nose	- Food quality and safety - Environmental monitoring - Breath analysis	Almost all VOCs, depending on the sensors in the array	- Detection of multiple compounds - Good selectivity	- Expensive - Quantification is difficult
DIMS	- Food quality and safety - Environmental monitoring - Breath analysis	All VOCs with proton affinity	- Good selectivity - Fast response	- Expensive - Limited portability - High energy consumption
IMS	- Drugs detection - Combustible gas leak detection	Depending on the ionization source	- Good selectivity and sensitivity - Portable and fast response	- Expensive - High energy consumption

In recent years, nonselective sensors have done considerable progresses in terms of performance. They have the advantage of being typically relatively cheap, small (mm to cm range of dimension), portable and commercially available, but they still lack selectivity, have a short lifetime, and suffer of drift. Moreover, data processing stage can be challenging. Their LOD ranges from ppb to ppm levels.

PIDs are the simplest devices, with high measuring ranges and short measuring times. However, with these sensors not all VOCs can be detected. In comparison, ECSs are less sensitive and have a more limited detection range but they can detect a broader range of analytes. A measurement typically takes more than 2 minutes due to the slowness of the diffusion process. On the other hand, they can be better tuned to measure specific VOCs because they are not affected by the presence of interferents.

MOS sensors are typically very small and light. Their selectivity may be influenced by dopants or filters. Since they usually operate at high temperature, they have a high-power consumption. The performance of these sensors are affected by some interferent gases such as CO or NO_x and by temperature and humidity.

Pellistors are small and inexpensive sensors, however they are employable only to detect combustible volatiles; moreover, they show low selectivity, and their performance depends on environmental conditions.

The VOCs species that can be detected by SAWs and QCMs depend on the applied film material on the sensor; moreover, they are complex to realize and have limited selectivity and are influenced by environmental conditions.

Compact GC and MS instruments are portable and have a good selectivity and sensitivity, but they are complex, perform discontinuous measurements, and the instrument maintenance costs are very high.

Through the combination of multiple nonselective detectors, E-Noses can produce fingerprints of complex VOCs mixtures. The capability of E-Nose devices largely depends on the sensors used in the array and the signal processing technique. However, they are not capable of identifying and speciate a single VOC in a mixture.

For this purpose, IMS and DIMS technologies are well suited, hence they show good selectivity and sensitivity. However, these techniques have a limited portability and high costs.

One of the most important criteria which often represent a limiting factor for the use of analytical techniques are the LODs and the measurement ranges. In Fig. 1.3, (Epping et al., 2023) the dynamic ranges of the presented detection techniques are compared. The given ranges are approximations and represent the average behaviour for each method, indeed these values are influenced by factors such as humidity, temperature, interferents and others.
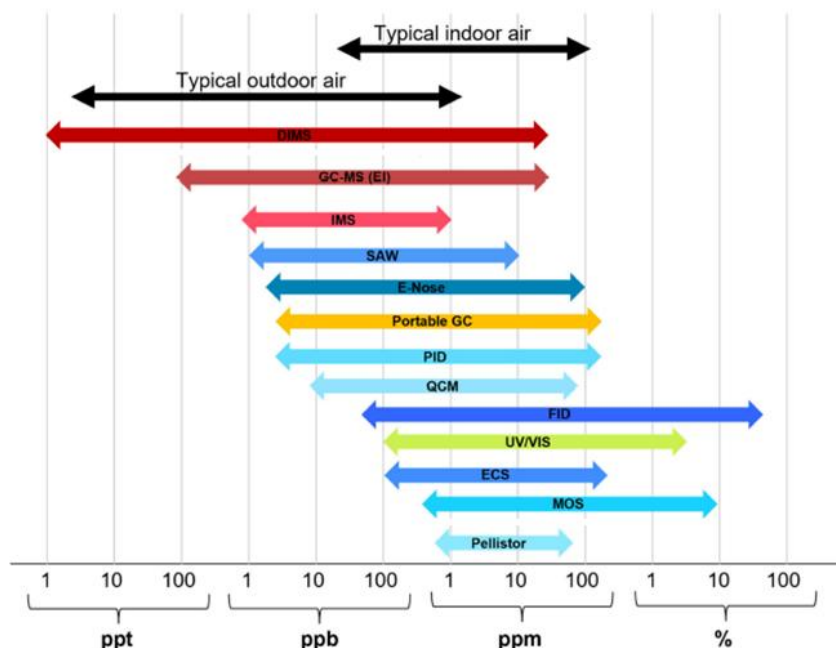
Fig. 1.3 Measurement range of the described analytical techniques compared to typical concentrations of VOCs in indoor and outdoor air. The given ranges are approximations and represent the average properties of each technique (Epping et al., 2023).

VOCs are typically found in outdoor air in concentrations that range from ppb to some ppm. In this range, the most sensitive devices are based on the DIMS and the GC-MS techniques, that can achieve LODs of some ppt with a measurement range up to some ppm. In indoor environments, VOCs concentrations are higher, from hundreds ppb to hundreds ppm. Several techniques, such as IMS, SAW, EN, portable GC, PID and QCM, can be employed for the realization of sensors that can achieve LODs in the range of some ppb with measurement ranges that can reach hundreds ppm. Devices based on FID, UV and ECs can achieve LOD of hundreds ppb. Their measurement range greatly varies, indeed FID and UV based sensors can detect VOCs up to low percentages and tens of percentage points, respectively; regarding ECs, they have a measurement range up to hundreds of ppm. MOS and pellistors have a LOD of some ppm and their measurement range reaches dozens of percentages and hundreds of ppm, respectively.

1.3.3 Novel approaches: Optical techniques

During the last few decades, important progresses have been made in the development of optical sensors for gas detection applications. Optical techniques are well suited for VOCs detection because one of their key advantages is the high selectivity. Moreover, optical sensors offer high sensitivity and little cross-response, with the possibility to detect multiple species at the same time. Compared to other sensing techniques, they show lower instrumental drift and faster response, with the additional benefit of being non-destructive (Xing et al., 2022). However, to date they are not as portable as nonselective sensors and are more expensive. Nowadays, real-time and in situ monitoring of VOCs concentration represents a challenging topic, particularly in environmental, health and industrial applications.

The principle of molecular absorption is based on the transitions that an electromagnetic wave causes in a chemical species. If a molecule is irradiated by infrared (IR) light, it is excited to a rotational-vibrational energy level manifold. Absorption lines are specific for each chemical species (Patimisco et al., 2014). Absorption spectroscopy techniques are divided into direct and indirect. Direct absorption techniques measure directly the absorption starting from the light transmitted by the sample, instead indirect techniques measure the effect that an optical absorption produces within a gas sample when it is photothermally excited by a light source.

Direct absorption techniques include Laser Absorption Spectroscopy (LAS), optical fibers, interferometric methods, chemiluminescence, Raman Spectroscopy, and Light-Induced Thermoelastic Spectroscopy (LITES). Among indirect techniques, Photoacoustic Spectroscopy (PAS) represents an important group of indirect absorption techniques based on the photoacoustic effect. Among the different PAS techniques, one of the most promising is Quartz-Enhanced Photoacoustic Spectroscopy (QEPAS).

In Chapter 2 the attention will be focused on the description of QEPAS and LITES techniques that have been employed in this thesis work.

Laser Absorption Spectroscopy (LAS)

In standard absorption spectroscopy, the radiation sources typically employed are lamps that have a wide continuous emission spectrum. In contrast, in Laser Absorption Spectroscopy (LAS), the employed light sources are lasers. They can be tuned in wavelength and can cover a wide spectral region, from UV to IR, with extremely narrow line widths. In addition, their spectral power density is higher compared to that of broadband sources, thus the detector noise

is typically negligible. Finally, thanks to the excellent collimation of the beam reachable with laser sources, long optical paths can be achieved.

LAS is based on the Lambert- Beer law, which expresses the relation between the incident light and the light transmitted after passing through an optical path of a given length. A typical setup of a LAS-based system includes a laser source operating in the IR range, a gas cell, and a photodetector. The compactness and robustness of the sensor are determined by the employed gas cell and the capacity of preserving the optical alignment between the laser beam and the gas cell over long times (de Palo et al., 2023).

Tunable Diode Laser Absorption Spectroscopy (TDLAS) technique is by far the most common LAS technique. A basic TDLAS setup consists of a tunable diode laser source (such as VCSEL, DFB, etc.), transmitting and receiving optics, a gas cell, and a detector (Fig 1.4).
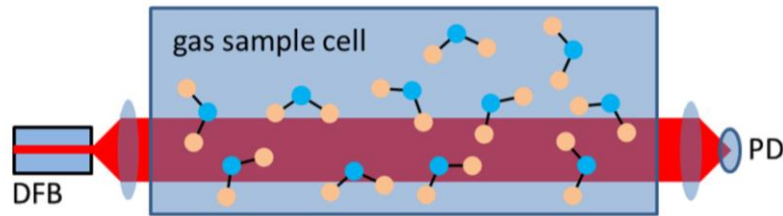
Fig. 1.4 Schematic of a typical TDLAS setup.

The basic principle behind the TDLAS technique is that the emission wavelength of a diode laser can be finely tuned by controlling the temperature or injection current, over the characteristic absorption lines of a specific target gas present in the gas cell. A detector records the transmitted laser intensity as the laser wavelength is repetitively scanned through the central frequency of an absorption line of the target gas. Then, the intensity of the transmitted radiation can be related to the concentration of the gas.

Allowing the radiation to travel longer distances enable the detection of small concentrations of absorbing molecules and thus, increase the ultimate sensitivity of detection. The correct approach is to increase the total optical path by forcing the radiation to remain confined within a small and constant volume. One way to increase the light absorption path length is the use of a multi-pass cell, which guarantees high stability and long effective path lengths. It traps the radiation through multiple reflections between two large convex mirrors positioned opposite each other, so that with each reflection on a mirror the beam travels a different optical path to reach the other mirror. Effective optical path lengths of several tens of meter can be reached with gas cell lengths of few tens of centimetres (Graf et al., 2018). Highly performant multipass cells are commercially available, however they are expensive, delicate, and labour-intensive. Moreover, they must be used with expensive and fast photodetector to obtain highly sensitive

sensors in narrow wavelength ranges. In literature, two of the most detected VOCs with this technique are acetone and acetylene (Nadeem et al., 2018; Lindley et al., 2006).

Another way to increase the light absorption path length is the use of cavity enhanced techniques, such as cavity ring-down spectroscopy (CRDS) and incoherent broadband cavity-enhanced absorption spectroscopy (IBBCEAS), that are based on high finesse optical cavities. The absorption optical path length is improved through multiple reflections of the light on highly reflective mirrors, greatly improving the detection sensitivity. In CRDS, light intensity leaking out from the cavity decreases exponentially. The measurements of the ring-down times, with and without the target gas sample inside the cavity, allow to deduce the absorption coefficient of the sample. This technique has been widely employed for measurement of VOCs species such as acetylene, ethylene, methyl iodide and dimethyl disulfide (Schmidt et al., 2010). IBBCEAS sensors, using a broad-band light emitting diode (LED) or Xe lamp as light source, offer the capability of broadband detection. Some VOCs detected with this technique are naphthalene and acetylene (Fiedler et al., 2003).

Optical fibers

A significant part of the research has focused the attention on the development of optical fiber-based sensors; they are considered attractive for their high sensitivity and selectivity and for the low limit of detection. These sensors are low cost, small, multiplexing, immune to electromagnetic interferences, and able to operate remotely. A typical setup includes a light source, an optical fiber, and a detector. The light emitted from the source is coupled into the fiber and propagates along the fiber by total internal reflections (TIR). Generally, the optical fiber is composed of a silica cladding and a germanium-doped silica core. The core has a slightly higher refractive index compared to the cladding, allowing a strong confinement of the light inside the core and its propagation with minimum transmission losses. Most of the fiber-based sensors for VOCs detection are based on the phenomenon of evanescent wave excitation (Pathak et al., 2022). One of the most effective methods to monitor VOCs concentration is to deposit a highly selective VOC material on top of the fiber. It changes one of its properties, such as its refractive index, conductivity or volume, with the presence of the target VOC (Jiao et al., 2020). This change affects the light propagation inside the fiber, causing a variation in terms of intensity, phase, or wavelength which can be detected by the photodetector and then demodulated. There are different categories of optical fiber-based sensors for VOCs detection; they can be classified into: interferometry based, Bragg grating based, microstructured based

and absorption based. Optical fibers-based sensors for VOCs detection have been employed especially to assess air quality and for environmental monitoring (Pathak et al., 2022).

Interferometric methods

Interferometry has been applied to several applications for highly sensitive measurements because it is an in-situ, non-contact, and non-destructive technique (Khan et al., 2020). The most employed interferometric method is represented by the Fourier Transform Infrared (FTIR) Spectroscopy. In this technique the IR beam is usually generated by a heated ceramic source (broadband light source). The heart of every FTIR instrument is the interferometer; the most common type is the Michelson interferometer. A collimating mirror is employed to collimate the beam, which is then directed to a beamsplitter that transmits approximately half of the light incident upon it and reflects the remaining half. A fraction of the transmitted light travels to a fixed mirror, while the other fraction travels to a moving mirror. The beams are reflected by the two mirrors back to the beamsplitter, where they are recombined into a single beam. The resulting beam interacts with the target gas contained in a gas cell and finally strikes the detector. A multi reflection cell is used to increase the optical path length. Because the path of the first beam is fixed in length and the other changes as the moving mirror moves, the signal exiting from the interferometer is the result of these two beams "interfering" with each other (Fig. 1.5).
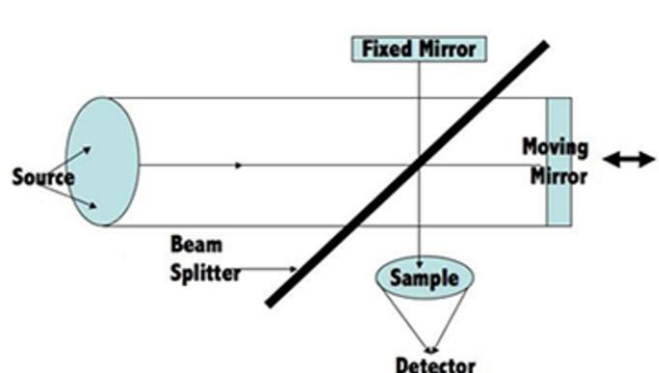

Fig. 1.5 Schematic representation of the functioning of an FTIR.

The measured interferogram signal cannot be interpreted directly, hence a means of "decoding" is required (Giechaskiel et al., 2021). This can be accomplished via the Fourier transformation. This technique ensures high resolution over a wide spectral range, meeting the needs of simultaneous measurement of different target gases. The FTIR technique faces several difficulties related to the collection of appropriate background reference spectra, the analysis of measured spectra, the calibration, and the effects of spectral resolution on the detection

sensitivity. With this technique several VOCs related to domestic emissions and vehicles' exhaust have been detected and measured (Lechner et al., 2001).

Another interferometric method applied for VOCs detection is the film-mediated sensing method. When a target VOC interacts with the gas sensing film, it changes volume (i.e. thickness) and/or its optical properties (i.e. refractive index) due to absorption/adsorption. The most employed sensing materials are films of polymer or microporous silicates that are selected according to the desired target molecules. These perturbations imply a change in the optical path length that leads to a quantifiable phase shift, which demodulated, gives the concentration of the target VOC. VOCs species detected with this technique include H_2, CO_2, ammonia, N_2O and HS (Hao et al., 2017).

Chemiluminescence

Chemiluminescence (CL) is the emission of photons when chemically excited molecules decay to ground state following a chemical reaction. While there are several liquid-based chemiluminescence reactions, the reaction with ozone is a gas phase reaction and thus can be used for VOCs detection and analysis (Toby, 1984). Ozone can react in a chemiluminescence reaction with nitric oxide (typically found in vehicles' exhaust measurements), with reduced sulfur compounds (found in the atmospheric sulfur cycle) and with compounds containing double bonds (Hills et al., 1990). Since CL has a very low background and the wavelengths for each reaction are different, this technique can achieve very low detection limits, also in the ppt range. A CL detector can be used as a stand-alone device or as a sulfur or nitrogen specific detector in conjunction with a GC, where all compounds are reduced in a hydrogen flame before the detector.

Raman Spectroscopy

Raman spectroscopy is a versatile analytical tool that can reveal vibrational fingerprints of molecular structures and identify chemical compounds with high selectivity thanks to sharp features in the Raman spectra. However, conventional Raman spectroscopy is not very sensitive, but it can be enhanced using different approaches. One approach is the Surface-enhanced Raman spectroscopy (SERS) which employs nano-structured substrates sensitive to a specific VOC, but they are fragile and difficult to manufacture (Yuan et al., 2022). Another approach to enhance the sensitivity of the technique is to tightly confine both the optical excitation and the target VOC within an optical waveguide. In this way, the Raman signal is significantly increased through an increased interaction volume. Silicon nitride (SiN)

waveguides are well-established for Waveguide-enhanced Raman spectroscopic (WERS) technique (Wang et al., 2022). These sensors have been used to measure traces of VOCs in water and air, mainly for environmental applications (Park et al., 2015).

1.4   Spectral ranges of VOCs

Infrared (IR) spectroscopy provides opportunities for highly selective and sensitive detection of several VOCs, due to the presence of a lot of strong absorption molecular lines and bands of these compounds in the IR spectral range. One of the main challenges of working with IR spectroscopy is the interpretation of the spectra. Interpreting the frequencies of IR light absorbed by a molecule, it is possible to identify bond-stretching motions, and therefore gain information about the structure of the molecule. Absorption of IR radiation by an organic compound causes the stretching of chemical bonds (Smith, 2018). In order for a vibrational mode to absorb IR radiation, it must result in a periodic change in the dipole moment of the molecule. Such vibrations are said to be IR active. In general, the greater the polarity of the bond is, the stronger is its IR absorption; for instance, the carbonyl bond is very polar and thus strongly adsorb. The peak locations of some functional groups of VOCs are presented in Fig. 1.6 (Johnson et al., 2023).
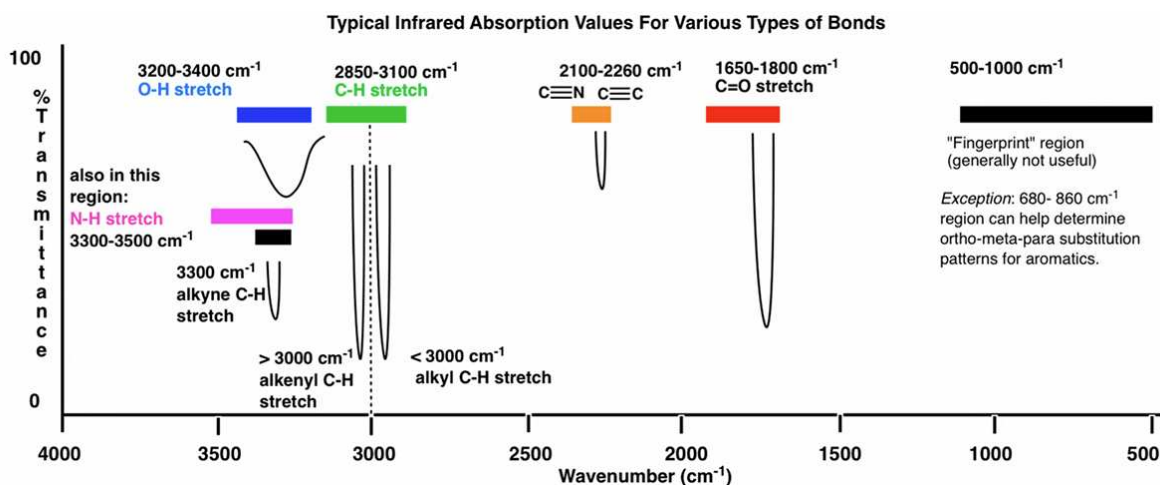

Fig. 1.6 Locations of some major absorption bands in the mid-IR region (Johnson et al., 2023).

Most organic functional groups adsorb in the region of the spectrum $1500 \sim 4000 \ cm^{-1}$. In the range $4000 \sim 2500 \ cm^{-1}$, there is the stretch of X-H bond (where X include C, N, O), which is found in alkanes, aromatic rings, alcohols, and amine. In the range $2500 \sim 2000 \ cm^{-1}$, the alkene functional group (C≡C) and C≡N stretches bonds are found. Carbonyl functional

group (C=O) typically shows up around $1750\ cm^{-1}$ and is present in compounds such as esters, alkenes, and aromatic rings. Some low-energy bond stretch and other molecular movements, such as bending and rotations, adsorb at wavenumber below $1000\ cm^{-1}$ in a unique way for each molecule. For this region this spectral region can be used to distinguish the different compounds.

The C-H out-of-plane bending vibrations, related to aromatic rings, show up in the region $680 - 860\ cm^{-1}$.

To-date LAS techniques have been mostly employed in the spectral region $3 - 12\ \mu m$, which covers a substantial spectral range of fundamental transitions. Several works report the development of IR sensors that exploit the roto-vibrational band of BTEX centred at $3.3\ \mu m$ ($3040\ cm^{-1}$) through different techniques such as cavity-enhanced spectroscopy and multi-pass absorption sensing via difference frequency generation. Additionally, the ν_{14} band centred at $1023\ cm^{-1}$ ($9.7\ \mu m$) has been investigated using tunable diode laser spectroscopy by employing a multipass Herriott cell with a path length of $472\ cm$ (Kinjalk et al., 2024). The BTEX absorption spectra in the spectral region $600 - 4000\ cm^{-1}$ are reported in Fig. 1.7. The roto-vibrational band of BTEX around $3040\ cm^{-1}$ ($3.3\ \mu m$) is shown in the inset of Fig. 1.7 (Mhanna, et al., 2024).
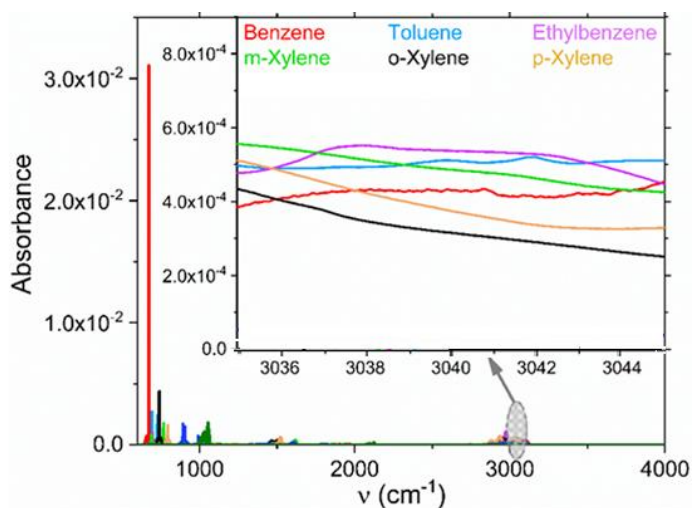

Fig. 1.7 BTEX absorption spectra taken from the PNNL database in the spectral region 600 – 4000 cm^{-1}, simulated at T = 25 °C, P = 1 atm, L = 30 cm, χ = 1000 ppm. The inset shows a close-up view of the range 3035 – 3045 cm^{-1} (Mhanna, et al., 2024).

However, as can be seen in Fig. 1.7, the spectral region around $3040\ cm^{-1}$ is characterized by low selectivity, due to the strong overlap between BTEX compounds and light hydrocarbons,

as they share the same class of molecular vibrations (C-H stretching around 3.3 μm) (Sy et al., 2022).

For BTEX detection, an alternative to these spectral ranges is represented by the region $12 - 15\ \mu m$, where intense and well-separated BTEX spectral features occur (Fig. 1.8). The spectroscopic scenario in the range $12.1 - 15.4\ \mu m$, involving the absorption bands of BTEX and the most relevant atmospheric interferents such as water vapor and carbon dioxide, is represented in Fig. 1.8.
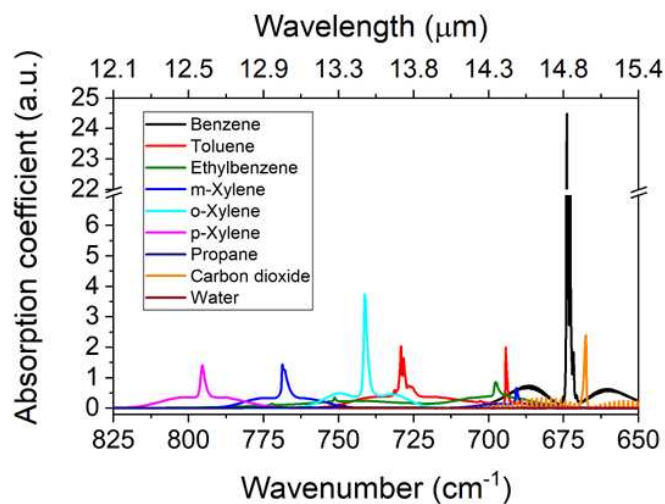

Fig. 1.8 Comparison of absorption cross-section at atmospheric pressure of pure BTEX compounds, water vapor and carbon dioxide in the in the range $12.1 - 15.4\ \mu m$, from HITRAN database (Kinjalk et al., 2024).

The cross-sections have been simulated for pure compounds just for comparing shape and potential overlap of the absorption bands, regardless from the realistic concentration ranges of specific applications. Water vapor absorption lines are almost completely absent in this range, or at least irrelevant, while CO_2 spectrum, although present, exhibits sharp lines that can be perfectly discriminated from the other VOCs of interest. However, in the long-wavelength IR spectral region the state-of-the-art for coherent light sources is meager. The lack of laser sources suitable above $12\ \mu m$ is due to fundamental performance limitations of long wavelength semiconductor lasers. Interband lasers are currently not available at all in the considered spectral range. This problem can be overcome employing intersubband transitions, exploited by Quantum Cascade Lasers (QCLs), but these devices exhibit poor performances above $10\ \mu m$ (Kinjalk et al., 2024).

Bibliography

Agbroko, S.O., & Covington, J. (2018). A novel, low-cost, portable PID sensor for the detection of volatile organic compounds. Sens. Actuators B Chem. 275, 10–15.

Altomare, D.F., Di Lena, M., Porcelli, F., Trizio, L., Travaglio, E., Tutino, M., Dragonieri, S., Memeo, V., & de Gennaro, G. (2013). Exhaled volatile organic compounds identify patients with colorectal cancer. Br. J. Surg. 100, 144–150.

Amann, A., Miekisch, W., Schubert, J., Buszewski, B., Ligor, T., Jezierski, T., & Risby, T. (2014). Analysis of exhaled breath for disease detection. Annual review of analytical chemistry, 7, 455-482.

Amann, A., Miekisch, W., Pleil, J., Risby, T., & Schubert, J. (2010). Methodological issues of sample collection and analysisofexhaledbreath. European Respiratory Monograph, 49.

Anand, S.S., Philip, B.K., & Mehendale, H.M. Volatile Organic Compounds, Editor(s): Philip Wexler, Encyclopedia of Toxicology (Third Edition), Academic Press, 2014, Pages 967-970, ISBN 9780123864550.

Aung, W. Y., Noguchi, M., Yi, E. E. P. N., Thant, Z., Uchiyama, S., Win-Shwe, T. T., ... & Mar, O. (2020). Traffic-related pollutants in roadside environment of Yangon, Myanmar. In IOP Conference Series: Earth and Environmental Science, 496, 1, 012001.

Bandehali, S., Miri, T., Onyeaka, H., & Kumar, P. (2021). Current State of Indoor Air Phytoremediation Using Potted Plants and Green Walls. Atmosphere. In Press

Baranwal, J., Barse, B., Gatto, G., Broncova, G., & Kumar, A. (2022). Electrochemical Sensors and Their Applications: A Review. Chemosensors. 10(9):363.

Barreto, G., Madureira, D., Capani, F., Aon-Bertolino, L., Saraceno, E., & Alvarez-Giraldez, L.D. (2009). The role of catechols and free radicals in benzene toxicity: An oxidative DNA damage pathway. Environ Mol Mutagen. 50: 771–80.

Beauchamp, J., Herbig, J., Gutmann, R., & Hansel, A. (2008). On the use of tedlar(r) bags for breath-gas sampling and analysis. J. Breath Res. 2, 046001.

Bauguitte, S. B., Brough, N., Frey, M. M., Jones, A. E., Maxfield, D. J., Roscoe, H. K., & Wolff, E. W. (2010). A network of autonomous surface ozone monitors in Antarctica: technical description and first results. Atmospheric Measurement Techniques Discussions, 3(6), 5795-5831.

Bragazzi, N.L., Amicizia, D., Panatto, D., Tramalloni, D., Valle, I., & Gasparini, R. (2015). Chapter Six - Quartz-Crystal Microbalance (QCM) for Public Health: An Overview of Its Applications, Advances in Protein Chemistry and Structural Biology, Volume 101,149-211.

Buszewski, B., Ulanowska, A., Kowalkowski, T., & Cieśliński, K. (2012). Investigation of lung cancer biomarkers by hyphenated separation techniques and chemometrics. Clinical chemistry and laboratory medicine, 50(3), 573-581.

Cecchi, T. (2021). Analysis of volatiles organic compounds in Venice lagoon water reveals COVID 19 lockdown impact on microplastics and mass tourism related pollutants. Sci. Total Environ. 783, 146951.

Chauhan, S. K., Saini, N., & Yadav, V. B. (2014). Recent trends of volatile organic compounds in ambient air and its health impacts: A review. Int. J. Technol. Res. Eng, 1(8), 667.

de Blas, M., Navazo, M., Alonso, L., Durana, N., & Iza, J. (2011). Automatic on-line monitoring of atmospheric volatile organic compounds: Gas chromatography–mass spectrometry and gas chromatography–flame ionization detection as complementary systems. Science of the total environment, 409(24), 5459-5469.

De Palo, R., Elefante, A., Biagi, G., Paciolla, F., Weih, R., Villada, V., Zifarelli, A., Giglio, M., Sampaolo, A., Spagnolo, V. & Patimisco, P. (2023), Quartz-Enhanced Photoacoustic Sensors for Detection of Eight Air Pollutants. Adv. Photonics Res., 4: 2200353.

Das, S., & Pal, M. (2020). Non-invasive monitoring of human health by exhaled breath analysis: A comprehensive review. Journal of The Electrochemical Society, 167(3), 037562.

Das, S., Pal, S., & Mitra, M. (2016). Significance of exhaled breath test in clinical diagnosis: a special focus on the detection of diabetes mellitus. Journal of medical and biological engineering, 36, 605-624.

David, E., & Niculescu, V. C. (2021). Volatile Organic Compounds (VOCs) as Environmental Pollutants: Occurrence and Mitigation Using Nanomaterials. International journal of environmental research and public health, 18(24), 13147.

Dent, A. G., Sutedja, T. G., & Zimmerman, P. V. (2013). Exhaled breath analysis for lung cancer. J. Thoracic Dis., 5, S540.

Dey, A. (2018). Semiconductor metal oxide gas sensors: A review. Mater. Sci. Eng. B, 229, 206–217.

Dima, A. C., Balaban, D. V., & Dima, A. (2021). Diagnostic Application of Volatile Organic Compounds as Potential Biomarkers for Detecting Digestive Neoplasia: A Systematic Review. Diagnostics (Basel, Switzerland), 11(12), 2317.

Epping, R., & Koch, M. (2023). On-Site Detection of Volatile Organic Compounds (VOCs). Molecules.; 28(4):1598. https://doi.org/10.3390/molecules28041598

Fiedler, S. E., Hese, A., & Ruth, A. A. (2003). Incoherent broad-band cavity-enhanced absorption spectroscopy, Chemical Physics Letters, 371, 284-294.

Filella, I., Llusia, J., & Penuelas, J. (2013). Floral volatile organic compounds: Between attraction and deterrence of visitors under global change. Perspectives in Plant Ecology, Evolution and Systematics, 15(1), 56-67.

Friedrich, R., & Obermeier, A. (1999). Anthropogenic emissions of volatile organic compounds. In Reactive hydrocarbons in the atmosphere (pp. 1-39). Academic Press.

Gałuszka, A., Migaszewski, Z. M., & Namieśnik, J. (2015). Moving your laboratories to the field–Advantages and limitations of the use of field portable instruments in environmental sample analysis. Environmental research, 140, 593-603.

Ghaffari, H. R., Kamari, Z., Hassanvand, M. S., Fazlzadeh, M., & Heidari, M. (2021). Level of air BTEX in urban, rural and industrial regions of Bandar Abbas, Iran; indoor-outdoor relationships and probabilistic health risk assessment. Environmental research, 200, 111745.

Giechaskiel, B., & Clairotte, M. (2021). Fourier transform infrared (FTIR) spectroscopy for measurements of vehicle exhaust emissions: A review. Applied Sciences, 11(16), 7416.

Goldstein, Allen, H., & Galbally, I.E. (2007). Known and Unexplored Organic Constituents in the Earth's Atmosphere. Environmental Science & Technology. 41 (5): 1514–21

Graf, M., Emmenegger, L., & Tuzson, B. (2018). Compact, circular, and optically stable multipass cell for mobile laser absorption spectroscopy. Opt. Lett.,43, 2434.

Guo, X., Schwab, W., Ho, C. T., Song, C., & Wan, X. (2022). Characterization of the aroma profiles of oolong tea made from three tea cultivars by both GC–MS and GC-IMS. Food Chemistry, 376, 131933.

Henderson, L., Brusick, D., Ratpan, F., & Veenstra, G. (2007). A review of the genotoxicity of ethylbenzene. Mutation Research/Reviews in Mutation Research, 635(2-3), 81-89.

Hansel, T. T., Kharitonov, S. A., Donnelly, L. E., Erin, E. M., Currie, M. G., Moore, W. M., & Barnes, P. J. (2003). A selective inhibitor of inducible nitric oxide synthase inhibits exhaled breath nitric oxide in healthy volunteers and asthmatics. The FASEB Journal, 17(10), 1298-1300.

Hao, T. & Chiang, K. S. (2017). Graphene-Based Ammonia-Gas Sensor Using In-Fiber Mach-Zehnder Interferometer. IEEE Photonics Technol. Lett., 29, 23, 2035–2038.

Hill, H.H., Siems, W.F., & St. Louis, R.H. (1990). Ion mobility spectrometry. Anal. Chem. 62, 1201A–1209A.

Hills, A.J., & Zimmerman, P.R. (1990). Isoprene measurement by ozone-induced chemiluminescence. Anal. Chem. 62, 1055–1060.

Ho, C.K., Lindgren, E.R., Rawlinson, K.S., McGrath, L.K., & Wright, J.L. (2003). Development of a surface acoustic wave sensor for in-situ monitoring of volatile organic compounds. Sensors, 3, 236–247.

Holm, S., & Åstrand, I. (1981). Exposure to acetone: uptake and elimination in man. Scandinavian Journal of Work, Environment & Health, 84-94.

Holøs, S. B. (2019). "VOC emission rates in newly built and renovated buildings, and the influence of ventilation – a review and meta-analysis". Int. J. Of Ventilation. 18 (3): 153–166.

Jensen, A., Liu, Z., Tan, W. (2021). Measurements of Volatile Organic Compounds During the COVID-19 Lockdown in Changzhou, China. Geophys Res Lett. 48(20):e2021GL095560.

Jin, X., Wu, Y., Santhamoorthy, M., Le, T.T.N., Le, V.T., Yuan, Y., & Xia, C. (2022). Volatile organic compounds in water matrices: Recent progress, challenges, and perspective. Chemosphere 308, 136182.

Johnson, J.B., Walsh, K.B., Naiker, M., Ameer, K. (2023). The Use of Infrared Spectroscopy for the Quantification of Bioactive Compounds in Food: A Review. Molecules, 28, 3215. https://doi.org/10.3390/molecules28073215

Joshi, S. M. (2008). The sick building syndrome. Indian journal of occupational and environmental medicine, 12(2), 61–64.

Kesselmeier, J., & Staudt, M. (1999). Biogenic Volatile Organic Compounds (VOC): An Overview on Emission, Physiology and Ecology. Journal of Atmospheric Chemistry. 33 (1): 23–88.

Khan, S., Le Calvé, S., & Newport, D. (2020). A review of optical interferometry techniques for VOC detection. Sensors and Actuators A: Physical, 302, 111782.

Khatib, M., & Haick, H. (2022). Sensors for volatile organic compounds. ACS nano, 16(5), 7080-7115.

Kim, H. Y., & Choi, N. J. (2020). Study on volatile organic compounds from diesel engine fueled with palm oil biodiesel blends at low idle speed. Applied Sciences, 10(14), 4969.

Kinjalk, K., Paciolla, F., Sun, B., Zifarelli, A., Menduni, G., Giglio, M., ... & Spagnolo, V. (2024). Highly selective and sensitive detection of volatile organic compounds using long wavelength InAs-based quantum cascade lasers through quartz-enhanced photoacoustic spectroscopy. Applied Physics Reviews, 11(2).

Krishnan, S. T., Devadhasan, J. P., & Kim, S. (2017). Recent analytical approaches to detect exhaled breath ammonia with special reference to renal patients. Analytical and bioanalytical chemistry, 409, 21-31.

Kumar, P., Kim, K.-H., Mehta, P.K., Ge, L., & Lisak, G. (2022). Progress and challenges in electrochemical sensing of volatile organic compounds. Results in Chemistry, Volume 4,100678.

Langford, V. S., Graves, I., & McEwan, M. J. (2014). Rapid monitoring of volatile organic compounds: a comparison between gas chromatography/mass spectrometry and selected ion flow tube mass spectrometry. Rapid Communications in Mass Spectrometry, 28(1), 10-18.

Lebrón-Aguilar, R., Soria, A.C., & Quintanilla-López, J.E. (2016). Comprehensive evaluation of direct injection mass spectrometry for the quantitative profiling of volatiles in food samples. Philos. Trans. R. Soc. A Math. Phys. Eng. Sci. 374, 20150375.

Lechner, B., Paar, H., & Sturm, P. (2001). Measurement of VOCs in vehicle exhaust by extractive FTIR spectroscopy. Europto Remote Sensing. SPIE.

Leidinger, M., Sauerwald, T., Conrad, T., Reimringer, W., Ventura, G., & Schütze, A. (2014). Selective detection of hazardous indoor VOCs using metal oxide gas sensors. Procedia Engineering, 87, 1449-1452.

Lindinger, W. & A. Hansel. (1997). Analysis of trace gases at ppb levels by proton transfer reaction mass spectrometry (PTR-MS). Plasma Sources Sci. Technol. 6, 111.

Lindley, R. E., Pradhan, M., & Orr-Ewing, A. J. (2006). Measuring acetylene concentrations using a frequency chirped continuous wave diode laser operating in the near infrared. Analyst, Vol. 131, No. 6, 731-738.

Loomis, D., Guyton, K. Z., Grosse, Y., El Ghissassi, F., Bouvard, V., Benbrahim-Tallaa, L., & Straif, K. (2017). Carcinogenicity of benzene. The Lancet Oncology, 18(12), 1574-1575.

Martins, E. M., Borba, P. F. D. S., Dos Santos, N. E., Dos Reis, P. T. B., Silveira, R. S., Felzenszwalb, I., & Correa, S. M. (2019). BTEX in an occupational environment. International Journal of Environmental Impacts, 2(2), 174-191.

Mhanna, M., Sy, M., Arfaj, A., Llamas, J., & Farooq, A. (2024). Highly Sensitive and Selective Laser-Based BTEX Sensor for Occupational and Environmental Monitoring. Appl. Opt. 63, 2892-2899.

Michanowicz, D. R., Dayalu, A., Nordgaard, C. L., Buonocore, J. J., Fairchild, M. W., Ackley, R., & Spengler, J. D. (2022). Home is where the pipeline ends: characterization of volatile organic compounds present in natural gas at the point of the residential end user. Environmental Science & Technology, 56(14), 10258-10268.

Miekisch, W., Kischkel, S., Sawacki, A., Liebau, T., Mieth, M., & Schubert, J.K. (2008). Impact of sampling procedures on the results of breath analysis. J. Breath Res., 2, 026007.

Montero-Montoya, R., López-Vargas, R., & Arellano-Aguilar, O. (2018). Volatile organic compounds in air: sources, distribution, exposure and associated illnesses in children. Annals of global health, 84(2), 225.

Moon, C. S. (2017). Estimations of the lethal and exposure doses for representative methanol symptoms in humans. Annals of occupational and environmental medicine, 29, 1-6.

Morakinyo, O. M., Mokgobu, M. I., Mukhola, M. S., & Engelbrecht, J. C. (2017). Health risk assessment of exposure to ambient concentrations of benzene, toluene and xylene in Pretoria West, South Africa. African Journal of Science, Technology, Innovation and Development, 9(4), 489-496.

Mustafa, M., Menon, J., Muniandy, R. K., Illzam, E. M., Nornazirah, A., Nang, M. K., & Sharifa, A. M. (2017). Gastric cancer: risk factors, diagnosis and management. IOSR J Dent Med Sci, 16(3), 69-74.

Nadeem, F., Mandon, J., Khodabakhsh, A., Cristescu, S. M., & Harren, F. J. M. (2018). Sensitive spectroscopy of acetone using a widely tunable external-cavity quantum cascade laser. Sensors, Vol. 18, No. 7, 2050.

Nordling Nilson, L., Barregård, L., Sällsten, G., & Hagberg, S. (2007). Self-reported symptoms and their effects on cognitive functioning in workers with past exposure to solvent-based glues: an 18-year follow-up. International archives of occupational and environmental health, 81, 69-79.

Ojala, S., Pitkäaho, S., Laitinen, T., Niskala Koivikko, N., Brahmi, R., Gaálová, J., & Keiski, R. L. (2011). Catalysis in VOC abatement. Topics in Catalysis, 54, 1224-1256.

Ollé, E.P., Farré-Lladós, J., & Casals-Terré, J. (2020). Advancements in microfabricated gas sensors and microanalytical tools for the sensitive and selective detection of odors. Sensors, 20, 5478.

Pathak, A. K., & Viphavakit, C. (2022). A review on all-optical fiber-based VOC sensors: Heading towards the development of promising technology. Sensors and Actuators A: Physical, 338, 113455.

Paredi, P., Kharitonov, S. A., Leak, D., Shah, P. L., Cramer, D., Hodson, M. E., & Barnes, P. J. (2000). Exhaled ethane is elevated in cystic fibrosis and correlates with carbon monoxide levels and airway obstruction. American journal of respiratory and critical care medicine, 161(4), 1247-1251.

Park, K. J., Wu, C., Mercer-Smith, A. R., Dodson, R. A., Moersch, T. L., Koonath, P., & Niemz, A. (2015). Raman system for sensitive and selective identification of volatile organic compounds. Sensors and Actuators B: Chemical, 220, 491-499.

Patimisco, P., Scamarcio, G., Tittel, F.K., & Spagnolo, V. (2014). Quartz-Enhanced Photoacoustic Spectroscopy: A Review. Sensors. 14(4):6165-6206.

Pauling, L., Robinson, A. B., Teranishi, R., & P. Cary. (1971). Quantitative analysis of urine vapor and breath by gas-liquid partition chromatography. Proc. Natl. Acad. Sci., 68, 2374.

Pereira, J., Porto-Figueira, P., Cavaco, C., Taunk, K., Rapole, S., Dhakne, R., Nagarajaram, H., & Câmara, J. S. (2015). Breath analysis as a potential and non-invasive frontier in disease diagnosis: an overview. Metabolites, 5(1), 3–55.

Pham, Y. L., & Beauchamp, J. (2021). Breath biomarkers in diagnostic applications. Molecules, 26(18), 5514.

Phillips, M., Cataneo, R. N., Saunders, C., Hope, P., Schmitt, P., & Wai, J. (2010). Volatile biomarkers in the breath of women with breast cancer. Journal of breath research, 4(2), 026003Popov, T. A. (2011). Human exhaled breath analysis." Ann. Allergy Asthma Immunol.,106, 451.

Prichard, E., & Barwick, V. Quality Assurance in Analytical Chemistry; John Wiley & Sons: Hoboken, NJ, USA, 2007.

Rajabi, H., Mosleh, M. H., Mandal, P., Lea-Langton, A., & Sedighi, M. (2020). Emissions of volatile organic compounds from crude oil processing–Global emission inventory and environmental release. Science of the Total Environment, 727, 138654.

Ras, M. R., Borrull, F., & Marcé, R. M. (2009). Sampling and preconcentration techniques for determination of volatile organic compounds in air samples. TrAC Trends in Analytical Chemistry, 28(3), 347-361.

Risby, T. H., Amann, A., & Smith D. (2015). Current status of clinical breath analysis. Breath Gas Analysis for Clinical Diagnosis and Therapeutic Monitoring, ed. A. Amman and D. Simth (World Scientific, Singapore), 251.

Sahil, K., Prashant, B., Akanksha, M., Premjeet, S., & Devashish, R. (2011). Gas chromatography-mass spectrometry: applications. International Journal of Pharmaceutical and Biological Archives, 2(6), 1544-1560.

Sanchez, J. M., & Sacks, R. D. (2007). Performance characteristics of a new prototype for a portable GC using ambient air as carrier gas for on-site analysis., 30(7), 1052–1060.

Sarigiannis, D. A., Karakitsios, S. P., Gotti, A., Liakos, I. L., & Katsoyiannis, A. (2011). Exposure to major volatile organic compounds and carbonyls in European indoor environments and associated health risk. Environment international, 37(4), 743-765

Schmidt, F. M., Vaittinen, O., Metsala M., Kraus, P. & Halonen L. (2010). Direct detection of acetylene in air by continuous wave cavity ring-down spectroscopy, Applied Physics B: Lasers and Optics, 101, 671-682.

Sindelarova, K., Granier, C., Bouarar, I., Guenther, A., Tilmes, S., Stavrakou, T., Müller, J.-F., Kuhn, U., Stefani, P., & Knorr, W. (2014). Global data set of biogenic VOC emissions calculated by the MEGAN model over the last 30 years. Atmospheric Chemistry and Physics. 14 (17): 9317–9341.

Smith, B. C. (2018). Infrared spectral interpretation: a systematic approach. CRC press.

Su, P., Z. Han, D. Kita1, P. Becla, H. Lin, S. Deckoff-Jones1, K. Richardson, L. C. Kimerling, J. Hu, & A. Agarwal. (2019). Monolithic on-chip mid-IR methane gas sensor with waveguide-integrated detector. Applied Physics Letters, Vol. 114, 5, 051103.

Sy, M., Arfaj, A., Farooq, A., Mhanna, M., & Llamas, J. (2022). Laser-based selective BTEX sensing using deep neural networks. Optics Letters, 47, 13, 3247-3250.

Szulczyński, B., & Gębicki, J. (2017). Currently Commercially Available Chemical Sensors Employed for Detection of Volatile Organic Compounds in Outdoor and Indoor Air. Environments 4, 1: 21.

Talaiekhozani, A., Fulazzaky, M. A., Ponraj, M., & Abd Majid, Z. M. (2013). Formaldehyde from production to application. In the 3th Conference of Application of Chemistry in Novel Technologies, 1-16Talapatra, A., & Srivastava, A. (2011). Ambient air non-methane volatile organic compound (NMVOC) study initiatives in India–A review. Journal of Environmental Protection, 2(01), 21.

Toby, S. (1984). Chemiluminescence in the reactions of ozone. Chem. Rev. 84, 277–285.

Xing, Y., Wang, G., Zhang, T., Shen, F., Meng, L., Wang, L. & He, S. (2022). VOC detections with optical spectroscopy. Prog. Electromagn. Res., 173, 71-92.

Wang, M., Qin, W., Chen, W., Zhang, L., Zhang, Y., Zhang, X., & Xie, X. (2020) Seasonal variability of VOCs in Nanjing, Yangtze River delta: implications for emission sources and photochemistry. Atmos. Environ. 223:117254.

Wang, P., & Miller, B. L. (2022). Waveguide-enhanced raman spectroscopy (WERS): an emerging chip-based tool for chemical and biological sensing. Sensors, 22(23), 9058.

Williams, J., & Koppmann, R. (2007). Volatile organic compounds in the atmosphere: an overview. Volatile organic compounds in the atmosphere, 1.

Wilson, A.D., & Baietto, M. (2009). Applications and advances in electronic-nose technologies. Sensors, 9, 5099–5148.

Witkiewicz, Z., & Wardencki, W. (2019). Transportable, portable and micro gas chromatographs. Anal. Chem. Indian J., 19, 142.

Wolkoff, P. (1995). Volatile organic compounds. Indoor Air, Suppl, 3, 1-73.

WHO, "Exposure To Benzene: a Major Public Health Concern," Prev. Dis. Through Heal. Environ. 3–6 (2019).

World Health Organization. (1985). Toluene. World Health Organization.

World Health Organization Publications. Air Quality Guidelines for Europe; European Series No. 91; World Health Organization: Copenhagen, Denmark, 2000.

Wu, C. H., Feng, C. T., Lo, Y. S., Lin, T. Y., & Lo, J. G. (2004). Determination of volatile organic compounds in workplace air by multisorbent adsorption/thermal desorption-GC/MS. Chemosphere, 56(1), 71-80.

Yang, Z., Du, L., Li, Y., & Ge, X. (2022). Secondary organic aerosol formation from monocyclic aromatic hydrocarbons: insights from laboratory studies. Environmental Science: Processes & Impacts, 24(3), 351-379.

Yuan, K., Jurado-Sánchez, B., & Escarpa, A. (2022). Nanomaterials meet surface-enhanced Raman scattering towards enhanced clinical diagnosis: a review. Journal of Nanobiotechnology, 20(1), 537.

Zhou, X., Zhou, X., Wang, C., & Zhou, H. (2023). Environmental and human health impacts of volatile organic compounds: A perspective review. Chemosphere, 313, 137489.

Zhou, M., Liu, Y., & Duan, Y. (2012). Breath biomarkers in diagnosis of pulmonary diseases. Clinica Chimica Acta, 413(21-22), 1770-1780.

Chapter 2:

Quartz-Enhanced Photoacoustic Spectroscopy and Light Induced Thermo-Elastic Spectroscopy

2.1. Basic principles of QEPAS technique

2.1.1 From PAS to QEPAS

One of the most robust trace-gas optical detection techniques is photoacoustic spectroscopy (PAS), which can reach a high detection sensitivity with a compact and relatively low-cost acoustic detection module (Elia et al., 2009). PAS is based on an optical absorption process, such as other optical detection techniques, but differs in the physical phenomenon used for the detection of the absorption signal. The photoacoustic (PA) effect was discovered in 1880 by A. G. Bell while working on the development of the Photophone and consists in the generation of acoustic waves due to absorption of modulated light in a gaseous, liquid, or solid sample (Bell, 1880). A schematic representation of the photoacoustic signal generation in a gas sample is shown in Fig. 2.1.
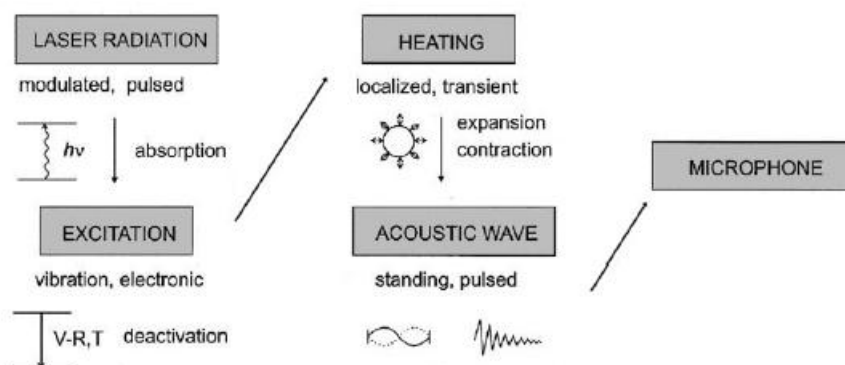

Fig. 2.1. Schematic representation of the PA signal generation in a gas sample.

A typical PAS gas sensing setup is composed of a light source, a resonant acoustic cell containing the target gas, a mechanical resonator which acts as a microphone, and a readout mechanism. When light at a specific wavelength is absorbed by a sample of target gas, it excites

a fraction of the ground-state molecular population into higher energy levels. These excited molecules will subsequently relax through a combination of radiative and non-radiative pathways. The latter generate a localized heating in the gas and an increase of the local pressure occurs (Patimisco et al., 2018). If the incident light is intensity modulated, the generation of thermal energy in the gas sample will be periodic and a pressure wave, i.e. sound wave, with the same frequency of the light modulation will be generated and detected by a microphone (Patimisco et al., 2014). The key advantages of PAS are that this technique is wavelength independent and does not require an optical detector. Other advantages of PAS-based sensors include small size, large linear dynamic range (from part-per-trillion (ppt) to few % as concentration range), and long-term stability. The PAS signal can be amplified by tuning the modulation frequency to one of the acoustic resonances of the gas sample cell. The PAS signal S can be expressed as (Patimisco et al., 2014):

$$S = C \cdot P_L \cdot \alpha, \qquad (2.1)$$

where C is the instrumental constant, P_L is the laser power and α is the gas absorption coefficient, that is given by:

$$\alpha = N_{tot} \cdot \sigma \cdot c, \qquad (2.2)$$

where N_{tot} is the total number of molecules per unit of volume, σ is the cross section of the optical transition and c is the concentration of the target gas and. According to equations *(2.1)* and *(2.2)*, the PAS signal is proportional to the target gas concentration, hence it is possible to measure the concentration of the target gas retrieving the amplitude of the PAS signal. Furthermore, once the PAS signal is acquired for known concentrations of target gas, the calibration curve can be obtained. Any concentration of target gas in real samples can be retrieved by comparing the measured PAS signal with the calibration curve. The minimum optical absorption coefficient α_{min} detectable with a PAS-based sensor is determined by the condition $S = N$, where N is the noise level, which is assumed to be independent of the optical excitation. The minimum detectable concentration c_{min} can be expressed as:

$$c_{min} = \frac{\alpha_{min}}{N \cdot \sigma}. \qquad (2.3)$$

The instrumental constant C depends on the cell size and its geometry, the modulation frequency, the transducer's efficiency and the quality factor Q (Q-factor) of the acoustic resonance, which is defined by:

$$Q = \frac{f_0}{\Delta f_{FWHM}}, \qquad\qquad (2.4)$$

where f_0 and Δf_{FWHM} are the resonance frequency and the full width at half maximum (FWHM) of the resonance profile, respectively. The Q-factor and f_0 are parameters that can be experimentally measured, and their values typically is in the ranges $40 - 200$ and $1,000 - 4,000 \, Hz$, respectively. The PAS signal is proportional to the effective integration time t, defined by:

$$t = \frac{Q}{f_0}. \qquad\qquad (2.5)$$

Light sources such as continuous-wave single-mode diode lasers, interband cascade lasers (ICLs) and quantum cascade lasers (QCLs) emitting in the mid-IR have been successfully applied in PAS (Elia et al., 2009). Compact PAS-based trace gas sensors employing broadband IR sources have been also reported (Fonsen et al., 2009). The three main noise sources are represented by: i) noise caused by the incident radiation upon the walls of the PAS absorption cell; ii) non-selective absorption of the gas cell windows; iii) external acoustic noise (Patimisco et al., 2014). To improve the signal-to-noise ratio (SNR), different designs of PAS cells have been proposed, including resonant cell with acoustic buffers (Bijnen et al., 1996), windowless and optical fiber amplifiers (Webber et al., 2003). PAS has been successfully applied to trace gas sensing in several fields of application, including atmospheric chemistry, volcanic activity, agriculture, industrial processes, workplace surveillance and medical diagnostics (McCurdy et al., 2006, Campbell et., 1979, Harren et al., 1999).

In 2002 A. Kosterev and F. K. Tittel developed a novel technique based on PAS, named quartz-enhanced photoacoustic spectroscopy (QEPAS) (Kosterev et al., 2002). This technique employs a quartz tuning fork (QTF) as a sharply resonant acoustic transducer to detect weak photoacoustic excitations. The basic idea of QEPAS is to accumulate the acoustic energy in a QTF, avoiding the use of traditional gas-filled photoacoustic cells, thereby removing restrictions imposed on the gas cell design by acoustic resonance conditions (Kosterev et al., 2005). The QTF is positioned in the acoustic near-field zone of the laser excitation beam and the gas cell only serves to separate the target sample from the surrounding environment and fix and control its pressure. QTFs are perfect candidates to detect weak photoacoustic excitation since they are characterized by a sharp resonant acoustic profile. Standard commercially available QTFs have a resonant frequency of 2^{15} or $\sim 32,768 \, Hz$. They have a Q-factor of $\approx 100,000$ or higher when encapsulated in vacuum and $\approx 10,000$ at atmospheric pressure.

Thes values lead to an energy accumulation time of $t \approx 320 \, ms$ at atmospheric pressure. Acoustically a QTF is a quadrupole, which provides good environmental noise immunity. The width of the QTF resonance curve at atmospheric pressure is $\sim 4 \, Hz$ thus, only frequency components in this narrow spectral band can produce vibrations of the QTF prongs. If sound waves at $32 \, kHz$ generated by external acoustic sources are considered, they have an acoustic wavelength of $\sim 1 \, cm$ and thus they tend to apply a force in the same direction on the two QTF prongs that are positioned at $\sim 1 \, mm$ distance. These sound waves do not excite the piezoelectrically active mode, and zero electrical response is generated. The only way to cause QTF vibration via the photoacoustic effect is to produce sound waves from an acoustic source located between the two QTF prongs. The standard way to realize this condition is that the excitation laser beam must pass through the gap between the QTF prongs without touching them (Patimisco et al., 2014). This causes an antisymmetric vibration of the QTF prongs in the QTF plane. This vibration mode is piezoelectrically active and thus electrical charges, proportional to the sound wave intensity, are generated. The generation of a photoacoustic wave involves an energy transfer from internal to translational molecular degrees of freedom. If a rotational-vibrational state is excited, a collision-induced vibrational to translation (V-T) relaxation follows, with a time constant characteristic for each molecule and dependent from the presence of other molecules and intermolecular interactions. QEPAS measurements are more sensitive to the V-T relaxation rate compared to the conventional PAS, which is commonly performed at $f_0 < 4 \, kHz$ (Patimisco et al., 2014). For gas species with a slow relaxation rate (such as CO, CO_2 and NO), the generated thermal waves in the gas sample cannot follow fast changes of the laser induced molecular vibration excitation. Thus, the generated photoacoustic wave is weaker than it would be in case of fast V-T energy equilibration (Ma et al., 2013). For instantaneous V-T relaxation, the detected photoacoustic signal can be expressed in the same way of the PAS:

$$S \propto \frac{Q \cdot P_L \cdot \alpha}{f}, \qquad\qquad (2.6)$$

where f is the QTF resonance frequency, Q its Q-factor, α is the gas target absorption coefficient, and P_L is the laser power. The Q-factor typically falls in the range from 10^4 to 10^5, depending on the carrier gas and the gas pressure. Like PAS-based sensing systems, the detection sensitivity of a QEPAS sensor is proportional to the exciting laser optical power. Significant enhancements of QEPAS signal-to-noise (SNR) ratio have been obtained thanks to the implementation of a micro-resonator (mR). The typical acoustic mR consists of two thin

tubes aligned perpendicular to the QTF plane, with the QTF positioned between the tubes. The subsystem composed of the QTF and the mR is called spectrophone or acoustic detection module (ADM). In 2010, Dong et al. reported a performance evaluation of a QEPAS sensor as a function of the geometrical parameters of the mR. In QEPAS technique the correct optical alignment between the laser beam and the QTF is fundamental. The laser beam that enters the mR must not touch the mR walls to avoid photothermal effects and create an undesirable background which can be several times larger than the QTF thermal noise level. This background has a shifting fringe-like interference pattern and limits the detection sensitivity (Spagnolo et al., 2010; Dong et al., 2011). QEPAS technique has been employed to detect several target gases in different application fields (Patimisco et al., 2014). A schematic of a typical QEPAS setup, used in most QEPAS-based sensors, is shown in Fig. 2.2.
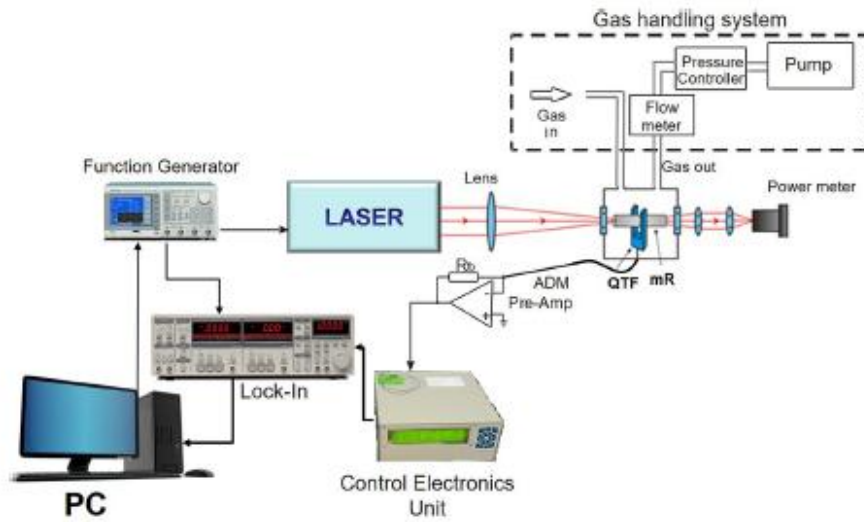

Fig. 2.2. Schematic of a typical QEPAS sensor setup. QTF, quartz tuning fork; mR, acoustic micro-resonator; ADM, acoustic detection module (Patimisco et al., 2018).

A laser source, typically an ICL or a QCL, is used as excitation source and the ADM is mounted inside a vacuum-tight cell equipped with two optical windows. The laser beam is focused by a lens between the QTF prongs, passing through the ADM windows. A power meter is used to ensure optical alignment. A function generator is used to sinusoidally dither the laser current at the QTF resonance frequency or one of its subharmonics. The flow rate and pressure of the sample target gas flowing in the ADM can be controlled and maintained constant using a flow meter and a pressure controller, respectively. A control electronics unit (CEU) is used to determine the main QTF parameters: dynamic resistance R, Q-factor, and resonant frequency

f_0. The CEU is also employed to pass the amplified signal from the transimpedance preamplifier (Pre-Amp) to the lock-in amplifier for the demodulation of the QEPAS signal.

2.1.2 Resonance properties of a QTF

A QTF can be designed to resonate at frequencies in the range $4 - 200 \, kHz$ and beyond, since resonance frequencies are defined by the properties of the employed piezoelectric material and by its geometry. The interaction between the intensity modulated laser beam and the target gas, leads to the generation of acoustic waves that mechanically bend the QTF prongs. Chromium/gold layers are deposited on the QTF surface as electrodes to collect the electrical charges induced by the mechanical deformation and whose position has been designed to increase the piezoelectric signal. Piezoelectricity is typical of most crystals lacking a center of inversion symmetry and represents the coupling between internal dielectric polarization and strain (Patimisco et al., 2014). When a stress is applied to these materials, a displacement of charge and a net electric field are induced. The effect is reversible, indeed when a voltage in applied to a piezoelectric material, a strain is generated. Each prong can be modelled as a slab of dimension $w_0 \times y_0 \times t_0$, as shown in Fig. 2.3.
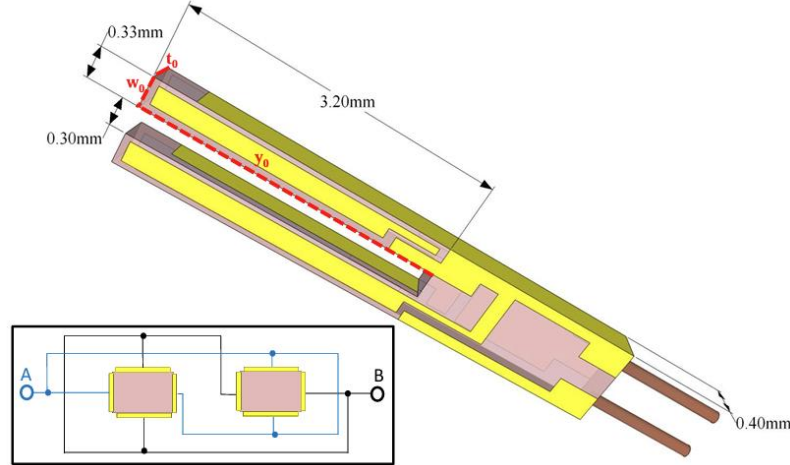

Fig. 2.3. Schematic of a standard quartz tuning fork (QTF). Each prong can be modelled as a rectangular bar of dimension $w_0 \times y_0 \times t_0$ (dotted lines). Inset: top view of the QTF with the electrical configuration for the electrodes A and B (Patimisco et al., 2014).

Standard QTFs are widely used in clocks, watches, and smartphones as clock oscillators due to their stability and precision (Friedt et al., 2007). The low cost of quartz crystal and the ease of production have pushed the mass production of QTFs by using standard photolithography and chemical etching (Lee et al., 2001) or, more recently, using optical techniques consisting of

direct cutting of the quartz crystal using ultrashort laser pulses. Standard QTFs have a resonant frequency of $\sim32\ kHz$ and two prongs $3.2\ mm$ long, with a width and a thickness of $330\ \mu m$ and with a gap between them of $\sim300\ \mu m$.

From a mechanical point of view, each prong of the QTF can be considered to behave as a cantilever. The vibrational modes of a QTF are generally divided in flexural, mostly excited by the PA effect, and torsional. The flexural modes take place in the x-y plane (in plane vibrations), while the torsional ones involve a rotation of the prongs around the z-axis. The in-plane flexural vibrations modes can be classified as in phase (symmetric) and out of phase (antisymmetric). The flexural antisymmetric modes, in which the two prongs oscillate in antiphase, are the only vibrational modes exploited in QEPAS-based sensors (Patimisco et al., 2016). The available resonant frequencies of the QTF can be calculated in the approximation that each prong behaves as a cantilever vibrating in the in-plane flexural modes. The first two flexural modes are shown in Fig. 2.4.
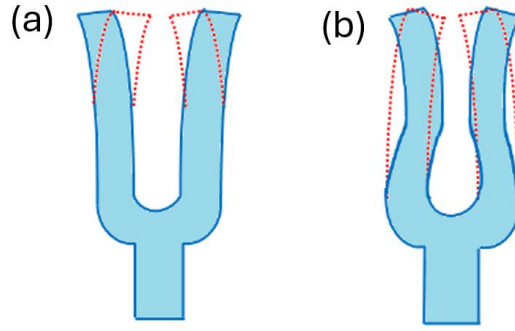

Fig. 2.4. (a) First in-plane vibrational mode of a tuning fork; (b) Third in-plane vibrational mode of a tuning fork (Patimisco et al., 2014).

In the first flexural mode, the tines move in opposite directions and the center of mass of the QTF remains unchanged. The flexural mode vibration can be modelled by considering each prong of the QTF as a 2D free-clamped beam, since the crystal width w is smaller than both the QTF thickness and length. When the applied force is removed, the beam will return to its original shape. Assuming that the elastic modulus, inertia and cross-sectional area are constant along the beam length, the equation for this vibration in vacuum is given by the following fourth-order differential equation, according to the Euler-Bernoulli approximation:

$$EI\ \frac{\partial^4 y}{\partial x^4}(x,t) + \rho A \frac{\partial^2 y}{\partial t^2}(x,t) = 0, \qquad (2.7)$$

where ρ is the density of the material, E the Young modulus of the material, t is the time, $A = w_0 \times y_0$ and x and y are the directions in the plane of the QTF. Equation (2.7) can be solved by the method of separation of variables, assuming that the displacement

can be separated into one part that depends on position and the other one on time. This leads to a simplified differential equation for the y-direction that can be solved by superimposing boundary conditions coming from the support of the QTF. The fixed end must have zero displacement and zero slope due to the clamp, while the free end cannot have a bending moment or a shearing force (free-clamped boundary conditions). The general solution is a linear combination of trigonometric equations leading to the frequency equation for the cantilever beam (Christen, 1983):

$$cos(k_n y_0)cosh(k_n y_0) = -1, \tag{2.8}$$

where k_n are the wavenumbers related to the eigenfrequencies f_n. The resonance frequencies in vacuum are given by (Hirata et al., 1985):

$$f_{n,vac} = \frac{\pi T}{8\sqrt{12}L_p^2}\sqrt{\frac{E}{\rho}}v_n^2, \tag{2.9}$$

where $\rho = 2650\ kg\ m^{-3}$ is the quartz density, $E = 72\ GPa$ is the component of the quartz Young's modulus in the vibrational plane of the QTF, L_p and T are the tuning fork length and thickness. The first two eigenmodes values are obtained for $v_{n=0} = 1.194$ (fundamental mode) and for $v_{n=1} = 2.988$, (first overtone mode).

Both mechanical motion and electrical response of the QTF can be modelled using differential equations, having equivalent mathematical forms. Due to the intrinsic coupling between strain and charge displacement, a QTF can be modelled both electrically and mechanically, as shown in Fig. 2.5.
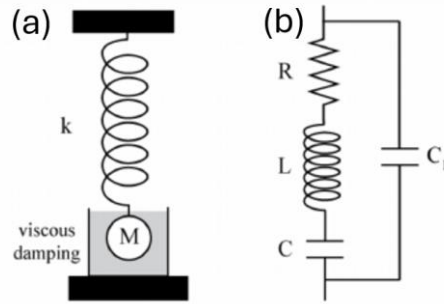

Fig. 2.5. (a) Mechanical model of a QTF; (b) Electrical model of a QTF.

The QTF is both a circuit with capacitance C, resistance R and inductance L, and equivalently a mass m on a spring, with spring constant k and damping factor β. The electrical behaviour of a QTF can be effectively described by the Butterworth-Van Dyke model (Fig. 2.5b). The presence of a capacitor C_p in parallel to the series RLC circuit considers any parasitic capacitance from electrical contacts and connecting wires. Mechanical and electrical domains

can be coupled through a relation, in which the force driving the QTF is proportional to the driving voltage. Hence, a voltage signal measured from the QTF can be translated into the force applied on it. The best way to acquire the QTF electrical response is to use an ultra-low transimpedance amplifier with feedback resistor $R_F = 10\ M\Omega$, which maintains a zero voltage between the QTF electrodes and thus the influence of the parallel stray capacitance C_p is neutralized. In this condition, the QTF model is an RLC series circuit, and the resonance frequency is given by:

$$f_0 = \frac{1}{2\pi}\sqrt{\frac{1}{LC}}, \qquad (2.10)$$

and the Q-factor, defined as the ratio of the total input energy and the dissipated energy during one cycle, is given by:

$$Q = \frac{1}{R}\sqrt{\frac{L}{C}}, \qquad (2.11)$$

The resonance properties of a QTF can be determined by analysing its response to a sinusoidal excitation of amplitude V_0 to the circuit depicted in Fig. 2.6.
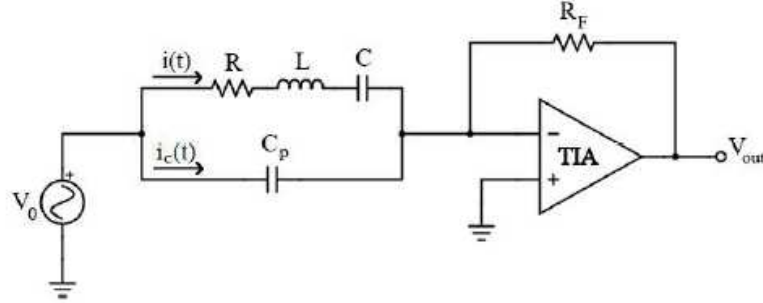

Fig. 2.6. Equivalent circuit for QTF characterization. TIA is the transimpedance amplifier, R_F is the feedback resistor (Olivieri et al., 2021).

The current $i(t)$ flowing through the RLC circuit is associated with the prong's vibration, whereas $i_c(t)$ is the stray current generated by C_p. The impedance Z of the equivalent circuit of the QTF is given by (Olivieri et al., 2021):

$$\frac{1}{Z(\omega)} = j\omega C_p + \frac{1}{j\omega L + R + \frac{1}{j\omega C}}. \qquad (2.12)$$

The output current is given by the sum of $i(t)$ and $i_c(t)$ and is converted into a voltage signal by the transimpedance amplifier with the feedback resistor R_F.

By solving the circuit represented in Fig. 2.6, the output signal amplitude V_{out} is retrieved as a function of the angular frequency of the excitation $\omega = 2\pi f$ and is given by:

$$V_{out} = \frac{A\omega}{Q\omega_0} \frac{\sqrt{1+2C'\left(1-\frac{\omega^2}{\omega_0^2}\right)+C'^2\left(1-\frac{\omega^2}{\omega_0^2}\right)^2 + C'^2\left(\frac{\omega}{\omega_0 Q}\right)^2}}{\left(1-\frac{\omega^2}{\omega_0^2}\right)^2 + \left(\frac{\omega}{\omega_0 Q}\right)^2}, \tag{2.13}$$

where $A = V_0 \cdot R_F/R$, $Q = L \cdot \omega_0/R$, $\omega_0 = 2\pi f_0$ and $C' = C_P/C$.

The QEPAS sensor noise measured at the output of the amplifier at the resonant frequency f_0 is primarily determined by the thermal noise of the equivalent resistor R (Fischer et al., 2006):

$$\sqrt{\frac{\langle V_N^2 \rangle}{\Delta f}} = R_F \sqrt{\frac{4KT}{R}}, \tag{2.14}$$

where V_N is the voltage noise at the transimpedance amplifier output, Δf is the detection bandwidth and T is the QTF temperature. The feedback resistor R_F introduces noise as well but it is several times lower than the thermal QTF noise and can be neglected for typical values of R in the range $10-100$ KΩ.

The QTF resonance parameters change when it is coupled to mR tubes to compose the spectrophone. The decrease of the Q-factor provides a measure of the acoustic coupling between the QTF and the mR. Acoustically, the mR is a dipole with a higher acceptance bandwidth compared to the QTF, which results in a reduction of the Q-factor of the spectrophone. The spectrophone has a higher fundamental frequency compared to the bare QTF, indicating that an additional force constant is added due to acoustic coupling (Dong et al., 2010).

2.1.3 QEPAS with custom QTFs

All the QEPAS-based sensors reported in literature until 2013 employed standard $32.7 \, kHz$ QTFs but their design was optimized for timing purposes. Two main factors limit the use of standard QTFs for trace gas sensing. Firstly, QEPAS signal strongly depends on the energy relaxation rates associated with the target gas species. The relaxation time constant τ_T depends on the specific molecule and on the specific gas carrier (typically air or N_2) and intermolecular interactions. For gases, the vibrational-translational (V- T) time constant τ_T falls typically in the μs time range (Griffith, 1950). To ensure an efficient energy transfer for a fast modulation

frequency f of the incident laser radiation, it is necessary to satisfy the condition $f \ll 1/2\pi\tau_T$ (Kosterev et al., 2005). Secondly, standard $32 \, kHz$ QTFs are characterized by a small volume between their prongs ($\sim 0.3 \times 0.3 \times 3 \, mm^3$) hence, the use of light sources with poor beam quality, like LEDs, fiber lasers, or laser emitting in the long IR range is precluded, since the beam diameter is bigger than the prong spacing. A way to overcome these limitations is to employ custom QTFs with larger prong spacing and lower resonance frequency ($f_0 < 20 \, kHz$) to approach gases relaxation rates. However, prong spacing influences the acousto-electric transduction efficiency, i.e. the conversion efficiency of the acoustic wave in piezoelectric charge production. The larger is the prong spacing, the lower is the sound wave intensity hitting the internal surface of the prong. Moreover, typically a decrease in the operation frequency f leads to a decrease of the QTF's Q-factor. A trade-off optimization of the above parameters must be found (Blom et al., 1992).

To optimize the strain field between the prongs and their support, a new geometry with T-shaped prongs has been proposed (Li et al., 2019). The T-shaped prong design provides two main advantages: i) a reduction of the resonance frequency with no influence on the Q-factor; ii) an increase of the stress field along the prongs lateral surface, leading to an increase of collected piezoelectric charges (Patimisco et al.,2019). Both advantages are beneficial for QEPAS-based sensor performances.

2.1.4 Influence of pressure on QTF properties

When a QTF vibrating at harmonic oscillations of small amplitude is immersed in a fluid medium, it tends to induce a motion in the fluid, giving rise to an energy loss and additional inertia. Hence, the reaction force is composed of a resistive part, which leads to energy dissipation by acoustic loss, and a reactive part, which gives rise to an additional inertia to the vibrating QTF. For these conditions, the Euler-Bernoulli approximation can be modified by considering a term, which includes damping effects (damping parameter C_d) and an additive mass u per unit length (Christen, 1983). This approximation is given by:

$$EI \, \frac{\partial^4 y}{\partial x^4}(x, t) + (\rho A + u)\frac{\partial^2 y}{\partial t^2}(x, t) + C_d \frac{\partial y}{\partial t}(x, t) = 0. \qquad (2.15)$$

In the realistic case of a negligible damping, i.e. $u << \rho A$, the additive mass causes a shift Δf of the QTF resonance frequency with respect to that in vacuum that is given by:

$$\Delta f = \frac{f_0' - f_0}{f_0'} = \frac{u}{2\rho A}, \tag{2.16}$$

where f_0 are the QTF resonance frequencies when prongs vibrate in air. In steady motion, the additive mass u is proportional to the density of air ρ_{air}, thus $u = k\rho_{air}$ (Sader, 1998). According to the ideal gas law, $\rho_{air} = \frac{MP}{R\Theta}$, where $M = 28.964 \frac{kg}{mol}$ is the molar mass, P is air pressure, $R = 62.3637\ m^3 \cdot Torr/K \cdot mol$ is the gas constant, and Θ is the QTF temperature. Air damping also affects the Q-factor of the QTF resonance mode. The contribution due to air damping was derived by Hosaka et al in 1995. In the viscous region, the dynamic can be described by the Navier–Stokes equation which expresses the Q-factor contribution Q_{air} related to air damping as (Giglio et al., 2019):

$$Q_{air} = \frac{4\pi\rho T w^2 f_0}{3\pi\mu w + \frac{3}{4}\pi w^2 \sqrt{4\pi\rho_{air}\mu f_0}}, \tag{2.17}$$

where T is the prong thickness, w is the crystal width and μ is the coefficient of viscosity of air. Thermoelastic and support losses are intrinsic dissipation mechanisms and can be assumed as pressure independent. In 2003, Hao et al. developed a model to describe support losses as the effect of a shear force exerted from the vibrating beam on the QTF support, which excites elastic waves propagating into the support with a wavelength greater than the prong width w. With this assumption, the contribution Q_{sup} related to support losses can be expressed as:

$$Q_{sup} = A_n \frac{L^3}{T^3}, \tag{2.18}$$

with the coefficients A_n depending on the n-th QTF resonance mode, and L and T that are the prong's length and thickness, respectively. An additional channel of energy dissipation are thermoelastic losses due to the inhomogeneity of the stress field, which, in turn, causes an inhomogeneous local increase in temperature (Zener, 1938). The corresponding Q-factor contribution Q_{TED} depends upon prong geometry and is given by:

$$Q_{TED} \propto \frac{T^3}{L^2}. \tag{2.19}$$

Each loss contribution is independent from the other, but all occur simultaneously for a vibrating QTF prong thus, the overall Q-factor can be written as (Olivieri et al., 2021):

$$\frac{1}{Q(P)} = \frac{1}{Q_0} + \frac{1}{Q_{air}(P)}, \tag{2.20}$$

where $\frac{1}{Q_0} = \frac{1}{Q_{TED}} + \frac{1}{Q_{sup}}$.

Using Eq. *(2.17)* for Q_{air}, $Q(P)$ can be rewritten as:

$$Q(P) = \frac{1}{C + D\sqrt{P}} \quad \text{where:} \begin{cases} C = \frac{1}{Q_0} + \frac{3\mu}{4\rho Twf_0} \\ \\ D = \frac{\frac{3}{4}\sqrt{\frac{4\pi\mu M}{R\Theta}}}{4\rho Tf_0} \end{cases} \quad (2.21)$$

Where the parameter C considers all the pressure-independent loss mechanisms.

2.1.5 Wavelength Modulation detection technique

In QEPAS technique, the modulation frequency must match the resonance frequency of the QTF or its sub-harmonics. The wavelength modulation (WM) technique is generally employed to improve the signal-to-noise ratio (SNR) and minimize external acoustic noise of a QEPAS-based sensor (Spagnolo et al., 2020). In WM, the frequency of the laser light is modulated with a periodic function, typically a sine wave, whose amplitude must be optimized for each target gas and operating pressure to maximize the QEPAS signal. One important advantage of this modulation technique is that only the noise centred at the detection frequency and within the detection bandwidth will affect measurements. The WM description is based on the intensity representation of an optical wave; in this way only the absorption of the sample is considered, and dispersion effects can be neglected. The instantaneous laser frequency is described by (Patimisco et al., 2014):

$$\nu(t) = \nu_0 - \Delta\nu cos(\omega t), \qquad (2.22)$$

where ν_0 is the optical carrier frequency and $\omega = 2\pi f$ is the modulation of the angular frequency due to the laser injection current modulated at the same angular frequency. In addition to frequency modulation, the current applied to the laser source produces a sinusoidal modulation of laser intensity and is given by:

$$I(t) = I_0 + \Delta I cos(\omega t), \qquad (2.23)$$

Where I_0 is the DC current of the laser. The amplitude ΔI of the sinusoidal intensity modulation is determined by the slope of the emitted laser power versus current characteristic, which is assumed constant across a wavelength scan. The WM based on a Lorentzian absorption line-shape is schematically depicted in Fig 2.7a. The instantaneous laser frequency interacts with

the absorption feature. Expanding with the Taylor series the absorption coefficient $\alpha(v(t))$ for a small Δv it is possible to obtain:

$$\alpha(v(t)) = \alpha_0 + \frac{\partial \alpha}{\partial v}|_{v=v_0} \Delta v \cos(\omega t) + \frac{1}{2}\frac{\partial^2 \alpha}{\partial v^2}|_{v=v_0} (\Delta v)^2 \cos^2(\omega t) + \cdots, \qquad (2.24)$$

where α_0 can be considered the background absorption contribution. The laser is modulated simultaneously both in intensity and wavelength. Inserting $I(t)$ and the Taylor series expansion of $\alpha(v(t))$ into the Lambert-Beer law it is possible to obtain:

$$I_t(t) = [I_0 + \Delta I \cos(\omega t)] \cdot [1 - L(\alpha_0 + \frac{\partial \alpha}{\partial v}|_{v=v_0} \Delta v \cos(\omega t) +$$

$$+ \frac{1}{2}\frac{\partial^2 \alpha}{\partial v^2}|_{v=v_0} (\Delta v)^2 \cos^2(\omega t))], \qquad (2.25)$$

where L is the effective length over which the absorption takes place to produce the acoustic wave (L is comparable with the thickness w of the QTF). The 1ω-signal $S_{1\omega}$ is given by:

$$S_{1\omega} = L\Delta I \alpha_0 - L\frac{\partial \alpha}{\partial v}|_{v=v_0} \Delta v. \qquad (2.26)$$

The trend of $S_{1\omega}$ as a function of the laser frequency across a Lorentzian absorption line is reported in Fig. 2.7b. The 2ω-signal $S_{2\omega}$ is given by:

$$S_{2\omega} = -L\Delta I \frac{\partial \alpha}{\partial v}|_{v=v_0} \Delta v + \frac{I_0}{2}\frac{\partial^2 \alpha}{\partial v^2}|_{v=v_0} (\Delta v)^2. \qquad (2.27)$$

This expression shows that the background absorption contributes to the $S_{1\omega}$ but it does not contribute to $S_{2\omega}$. In the assumption that the absorption coefficient α has a pure Lorentzian line shape, $S_{1\omega}$ has a pure first derivative line-shape with a constant background. On the other hand, $S_{2\omega}$ consists of two terms: the first, arising from the residual amplitude modulation (RAM) and proportional to the first derivative; the second is the second-derivative expression arising from the laser wavelength modulation. Hence, as it is possible to see in Fig. 2.7, that $S_{2\omega}$ is not a pure second derivative of the Lorentzian lineshape but is distorted by a contribution originating from the RAM. The distortion does not affect the peak position of $S_{2\omega}$ since the first derivative of the Lorentzian lineshape vanishes when $v = v_0$.
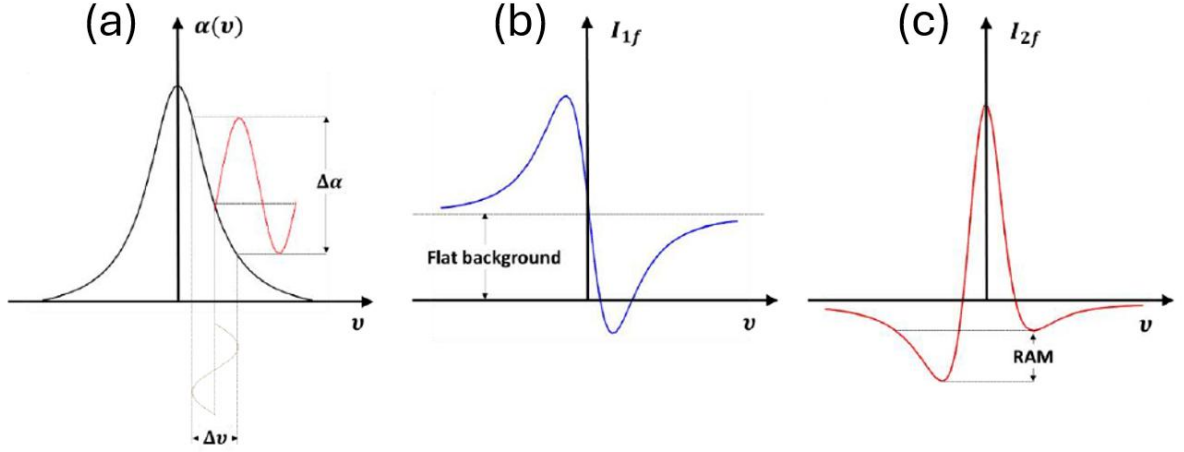
Fig. 2.7. (a) WM based on a Lorentzian absorption line-shape; (b) Absorption profile in WM and 1f-detection: the profile resembles the first derivative of a Lorentzian absorption line-shape with a flat background; (c) Absorption profile in WM and 2f-detection: the 2f-signal profile is not a true second derivative of a Lorentzian absorption line-shape, but it is distorted by a contribution originating from the RAM.

The generated QEPAS signal is then demodulated by a lock-in amplifier at the fundamental frequency f_0 or a successive harmonic nf. When the laser radiation is modulated at the resonant frequency f_0 and the QEPAS signal is demodulated at the same frequency, the demodulated signal is called 1f-QEPAS signal; while when the laser light is modulated at the $f_0/2$ and the QEPAS signal is demodulated at f_0, the demodulated signal is called 2f-QEPAS signal. In this case, the QTF detects sound oscillations at the second harmonic of the modulation frequency caused by a double intersection of the absorption line by the laser radiation during a modulation period. Working in $1f$-detection approach has two main disadvantages: i) the acquired line shape is heavily distorted; ii) it is not background-free and thus post processing techniques must be adopted to remove the contribution due to the background. On the other side, the $2f$-detection approach is background free. The central peak is at the maximum of the absorption there are two symmetrical lobes of opposite sign on two sides with respect to the central peak associated to the RAM contribution, introduced by the current modulation (Patimisco et al., 2014).

2.1.6 Advantages of QEPAS technique

Some merits of QEPAS include a simple design, the absence of a spectrally selective optical component, the applicability over a wide range of pressure including atmospheric pressure, the capability to analyse trace-gas samples as low as few cm^3 in volume, and immunity to external environmental noise thanks to the acoustic quadrupole structure and the narrow bandwidth of the QTF. The latter aspect allows to reduce the noise level and improve the SNR of QEPAS-based sensors. Moreover, these sensors have a fast response time (< 1 s), suffer from minimal drift, offer high gas specificity, are capable of part-per-trillion (ppt) detection sensitivity and allow real time and in-situ measurements (Spagnolo et al., 2013). Compared to sensors based on other optical techniques, a distinct advantage of a QEPAS sensor is that its performances can be improved increasing the output optical power of the laser source. However, QEPAS being a contact measurement method, is not recommended for the detection of corrosive gases, that can compromise the QTF resonance properties in terms of shifts of resonance frequency and degradation of Q-factor due to deterioration of the electrodes and/or the quartz crystal during long-term exposure.

To compare the performances of different laser based optical techniques, a metric that consider the available output optical power, the strength of the selected absorption line and the integration time used in the measurements is needed. In this case, the normalized noise equivalent absorption (NNEA) parameter, measured in $cm^{-1} \cdot W \cdot Hz^{-1/2}$, is obtained by normalizing the noise equivalent absorption to a $1\ Hz$ measurement bandwidth, represents the best choice (Hodgkinson et al., 2013; Laurila et al., 2005). Figure 2.8. reports a comparison among the performances of several gas detection techniques in terms of NNEA as a function of optical pathlength (Sampaolo et al., 2020; Patimisco et al., 2014). It should be noted that in most cases the reported NNEA was obtained in a laboratory setting and such performances cannot easily be replicated in outdoor environments.
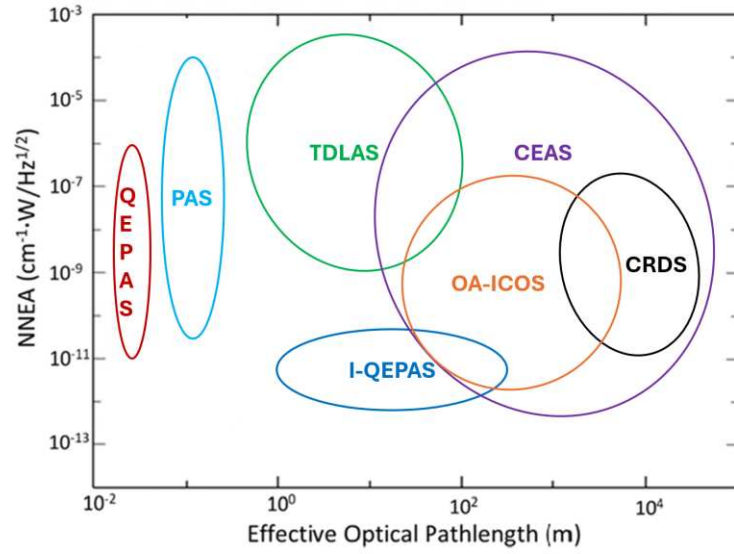
Fig. 2.8. NNEA for different gas detection techniques as a function of optical path-length. CEAS – cavity-enhanced spectroscopy, CRDS – cavity ring-down spectroscopy, OA-ICOS – off-axis integrated cavity output spectroscopy, PAS – photoacoustic spectroscopy, QEPAS – Quartz-enhanced photoacoustic spectroscopy, I-QEPAS – Intracavity quartz-enhanced photoacoustic spectroscopy, TDLAS – tunable diode laser absorption spectroscopy.

The techniques with the lowest NNEA, i.e. those capable to reach ppb and ppt sensitivities, are characterized by very long pathlengths (up to tens of km) and are CDRS, ICOS and CEAS, respectively. However, PAS and in particular QEPAS technique shows excellent performances, reaching NNEA in the $10^{-10} \, cm^{-1} \cdot W \cdot Hz^{-1/2}$ range, with the advantage of a much better sensor compactness compared to the previously mentioned techniques. Since QEPAS technique is characterized by a direct proportionality between the signal amplitude and the laser power available for gas excitation, the higher the optical power focused between the QTF prongs is, the lower will be the QEPAS sensor minimum detection limit. In 2014, Borri et al., developed an innovative spectroscopic technique, called intracavity QEPAS (I-QEPAS). This technique can be considered as a merging of CEAS and QEPAS. It has been used to detect CO_2, reaching a sensitivity of $230 \, ppt$ with $10 \, s$ of integration time and a corresponding NNEA of $2.5 \cdot 10^{-10} \, cm^{-1} \cdot W \cdot Hz^{-1/2}$.

2.2. Basic principles of LITES technique

2.2.1 QTF employed as infrared photodetector

In the last decade, the rapid development of infrared laser technology has led to an increasing demand for photodetectors capable of operating in a wide spectral range with high sensitivity. Nowadays, commercial laser sources can cover a wide region of the infrared spectrum but progresses in photodetection are still bogged down. Infrared photodetectors can be divided in two main groups: i) thermal detectors (bolometers, pyroelectrics and Golay Cells), in which the absorbed radiation causes a change of a physical property of the sensing material to generate an electrical signal; ii) photonic detectors (photoconductive, photovoltaic and photoemissive) in which the radiation is absorbed by the material via interaction with electrons and an electrical signal results from the changes in the electronic distribution (Lewicki et al., 2013). Commercially available photodetectors are usually composed of separate photoactive semiconductors, for example, silicon ($400-1100\ nm$), InGaAs ($800-1600\ nm$), and HgCdTe ($3-10\ \mu m$). Recently, QTFs have been proposed as an alternative to traditional photovoltaic or photoconductive infrared detectors exploiting the properties of quartz crystals. Due to the advantage of a high Q-factor ($> 10,000$) at atmospheric pressure, the detection bandwidth (few Hertz or even lower) is several orders of magnitude narrower compared to traditional infrared detectors (Haas et al., 2016). Moreover, QTFs are low cost and small sized and can operate in a wide spectral range without any cooling systems (Pan et al., 2023).

In 2018, a novel QTF-based gas sensing technique named Light-Induced Thermoelastic Spectroscopy (LITES) has been proposed by He (He et al., 2019) and Ma (Ma et al., 2018). This technique exploits the light-induced thermo-elastic effect occurring in a QTF as basic physical principle to enable light detection. In LITES the laser beam, after passing through a gas cell containing the target gas, is focused onto the QTF surface and photothermal energy is generated in the crystal because of light absorption by the quartz. Due to the thermo-elastic conversion, elastic deformations put the QTF prongs into vibration. When the laser is intensity-modulated at the resonance frequency of one of the flexural modes of the QTF, the mechanical vibrations of the prongs are enhanced and converted, via the piezoelectric effect, into an electrical signal proportional to the absorbed light intensity. This effect is enhanced when the radiation is focused close to the prong clamped end, named prong base, where the stress field is supposed to be mainly located at (He et al., 2020). A schematic diagram of LITES principle is shown in Figure 2.9.
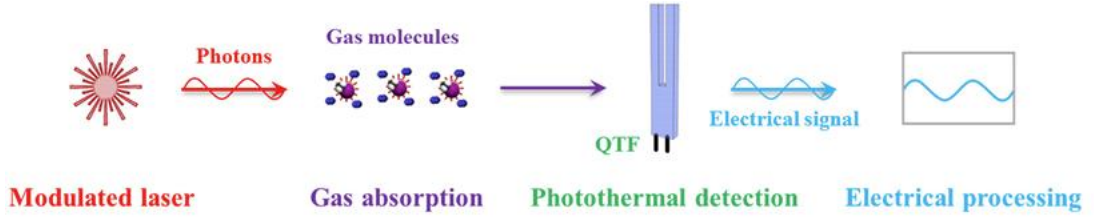
Fig. 2.9. Schematic diagram of light-induced thermoelastic spectroscopy (Pan et al., 2022).

The most employed QTFs in LITES sensors are the standard ones, with resonance frequencies $> 30 kHz$ ($30.72 kHz$ and $32.768 kHz$) and Q-factor of $\sim 10,000$ at atmospheric pressure. In 2018, Ma et al. realized the first trace gas sensor based on LITES technique for acetylene (C_2H_2) detection. The employed setup is shown in Fig. 2.10.
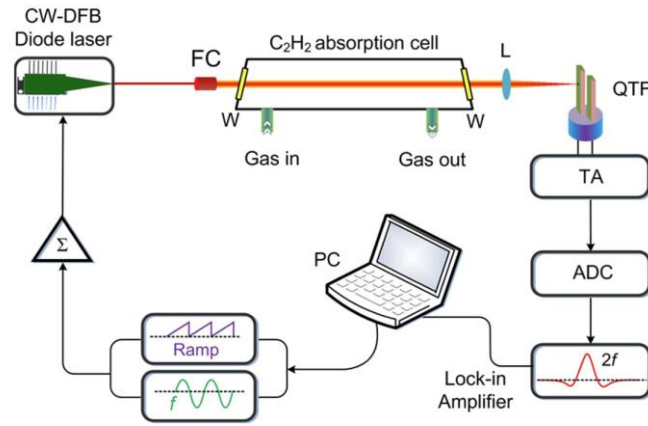

Fig. 2.10. Schematic diagram of the QTF based LITES sensor system (Ma et al., 2018).

In the experimental setup a $20\,cm$ gas absorption cell and a standard $32.7\,kHz$ QTF were employed. A distributed feedback (DFB) diode laser emitting at $1.53\,\mu m$ was selected as excitation source. A minimum detection limit (MDL) of $718\,ppb$ was obtained with an integration time of $1\,s$, corresponding to an NNEA of $7.63 \cdot 10^{-9}\,cm^{-1} \cdot W \cdot Hz^{-1/2}$. The obtained MDL is lower compared to the one reported by sensors based on TDLAS (He et al., 2016) and QEPAS techniques (Ma et al., 2017).

2.2.2 Thermo-elastic properties of a QTF

The LITES signal is generated by photothermal energy deposited in the quartz crystal because of light absorption. This energy is then converted in mechanical energy as vibration of QTF prongs at their natural frequencies, i.e. mechanical oscillations. This suggests that the LITES signal is proportional to the intensity of the strain field (elasticity) generated at the prong base, i.e. where the beam is focused, and to the accumulation time in units of heating period (thermic effect). The accumulation time is defined as the ratio between the Q-factor of the QTF and the angular frequency (Dong et al., 2010):

$$\tau = \frac{Q}{2\pi f}. \tag{2.28}$$

The LITES signal amplitude is expected to be inversely proportional to the resonance frequency f of the QTF and directly proportional to its Q-factor. The distribution of the strain field as well as the resonator accumulation time depends on prong geometry, hence the implementation of custom QTFs with a low resonance frequency and characterized by a longer energy accumulation time, but at the same time retaining a high Q-factor and having properly designed coating patterns to enhance light absorption, represents the best way to improve the performance of QTF-based LITES sensors (Ma et al., 2020). As explained in Section 2.1.3, the T-shaped geometry has been introduced and allows the reduction of the resonance frequency f without affecting the Q-factor.

For a deeper understanding of LITES phenomenon, five custom QTFs (from QTF#1 to QTF#5) with different length L, crystal thickness T and width W were analysed by Dello Russo et al. and compared to the standard $32.7\ kHz$ QTF. QTF#1 has a prong length of $L = 10\ mm$ and $W = 0.9\ mm$, with $T = 250\ \mu m$ (shown in Fig. 2.12). QTF#2 is a T-shaped QTF with $50\ \mu m$-deep rectangular grooves carved on both prong sides (Li et al., 2019). The QTF has the following geometrical parameters: $L = L1 + L2 = 9.4\ mm$, $T = 250\ \mu m$, $W1$ and $W2$ are $1.4\ mm$ and $2\ mm$, respectively (shown in Fig. 2.13). QTF#3 is a T-shaped QTF with the same geometrical parameters of QTF#2 but without grooves (Patimisco et al., 2019). QTF#4 and QTF#5 have rectangular prongs, both with $T = 250\ \mu m$, but QTF#4 has $L = 1.2\ mm$ and $W = 16.0\ mm$, instead QTF#5 has $L = 1.0\ mm$ and $W = 17.0\ mm$. For each QTF, the resonance frequency of the fundamental mode and the Q-factor measured at atmospheric pressure, the accumulation time τ calculated by using Eq. *(2.28)*, and the maximum strain field ε calculated by using the COMSOL simulation model are reported in Table 2.1.

Tab. 2.1. Electro-mechanical performances measured for all the QTFs analysed.

QTF	f [Hz]	Q-factor	τ [s]	ε [a.u.]
Standard	32757.4	8630	0.04	523
QTF#1	7230.3	8720	0.19	161
QTF#2	9783.8	11510	0.19	278
QTF#3	12460.7	10400	0.13	290
QTF#4	3853.8	7240	0.30	83
QTF#5	2877.5	5730	0.32	59

In 2019, Giglio et al. demonstrated that to increase the Q-factor of the QTF, a reduction of the length of the prongs and an increase in their thickness and in crystal width are required. On the other hand, the Euler-Bernoulli beam theory shows that the fundamental flexural mode resonance frequency is proportional to the ratio T/L, hence a reduction of the resonance frequency may result in a decrease in the Q-factor, leading to a decrease of the accumulation time. A trade-off optimization of these parameters must be found.

In Fig. 2.11, the LITES SNR values for the analyzed QTFs are plotted as a function of the product between the maximum strain field ε and the QTF accumulation time τ (Dello Russo et al., 2018).
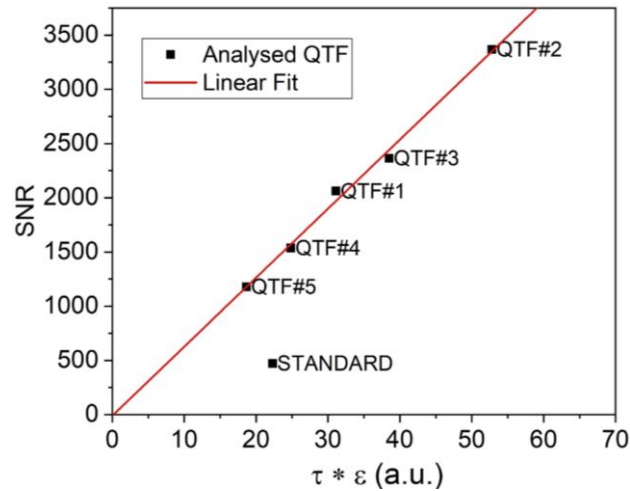
Fig. 2.11. SNR values of all the QTF analysed (black squares) as a function of the product between accumulation time and strain. The red line represents the best linear fit (Dello Russo et al., 2018).

Apart from the standard QTF, the LITES SNR values follow a linear trend as a function of the product $\tau \cdot \varepsilon$. The reason for the different trends of the standard QTF is ascribed to the geometrical parameters of the standard QTF, which is significantly smaller than the other analyzed QTFs. Indeed, the reduced size of the QTF prongs, comparable to laser beam spot size $(100\ \mu m)$, do not allow a precise mapping of the prongs surface area. As a result, the 1σ-noise level measured for the standard QTF was three times higher than the noise levels recorded for the other custom QTFs. Figure 2.11 points out that QTF#2 has the highest SNR.

2.2.3 LITES Signal mapping on QTF surface

In the study carried out by Dello Russo et al. the 2D mapping of the LITES signal at different laser spot positions on the QTF surface was performed, to find the optimal laser focusing position. In this study the QTF was positioned on the plane perpendicular to the laser beam direction. The laser beam position was fixed, while the QTF can translate along x and y axes on the QTF plane. The first investigated QTF was QTF#1 (refer to Table 2.1). It had a fundamental resonance frequency of $7230.3\ Hz$ and a Q-factor of 8800 at atmospheric pressure. The LITES signal mapping onto the QTF#1 surface is reported in Fig. 2.12a. To calculate the strain spatial distribution when the QTF is forced to vibrate at one of its eigenfrequencies modes and a finite element method (FEM) modelling was carried out using COMSOL Multiphysics. The strain distribution in the QTF plane at the fundamental is depicted in Fig. 2.12b. The LITES signal colour scale reports signal intensities in mV while the intensity of the strain field is reported in arbitrary unit.
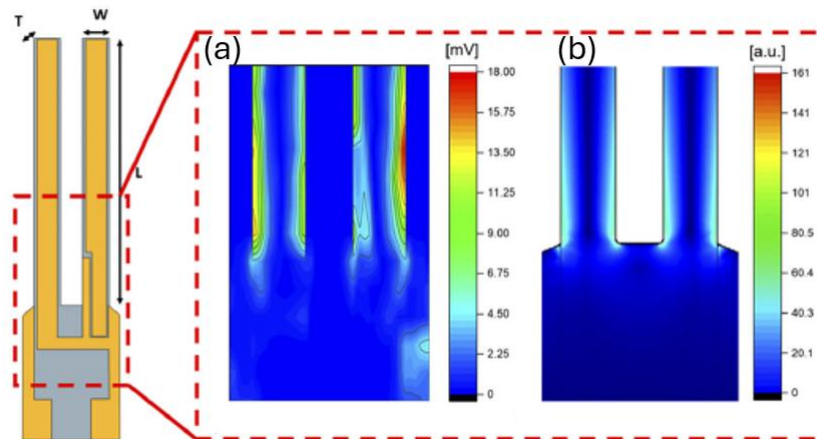

Fig. 2.12. (a) LITES peak signal mapping onto the QTF#1 surface; (b) COMSOL simulation of the strain field for QTF#1 fundamental resonance mode (Dello Russo et al., 2018).

When the laser beam hits the QTF close to the prong base, additional energy losses can arise from thermo-elastic damping, affecting the prong vibration (Giglio et al., 2019). Figure 2.12 points out that the map of LITES signal peak values retraces the spatial distribution of the strain field: the piezoelectric charges generated by prongs vibration accumulate where the induced strain is maximum, hence the maximum LITES signal occurs where the strain reaches its highest values.

The same investigation was performed with the T-shaped QTF#2 (refer to Table 2.1). The fundamental mode had a resonance frequency of $9783.8\ Hz$ and a Q-factor of 11,500 at atmospheric pressure. The map of the LITES peak signal and the simulated strain distribution for the QTF#2 are shown in Fig. 2.13a and 2.13b, respectively.
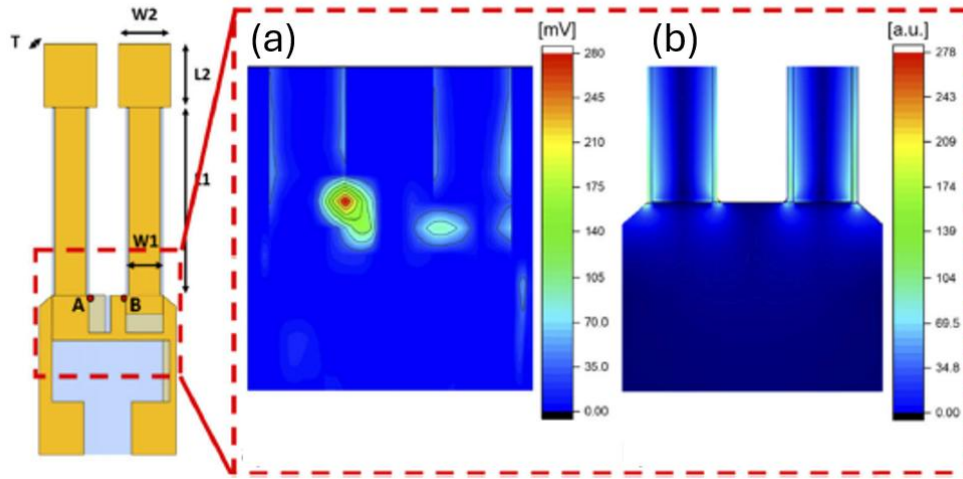
Fig. 2.13. (a) LITES peak signal mapping onto the QTF#2 surface; points A and B indicate the positions of the main local maxima of the LITES signal.

(b) COMSOL simulation of the strain field for QTF#2 fundamental resonance mode (Dello Russo et al., 2018).

Also for QTF#2 the spatial distribution of the LITES signal shows a good match with the pattern of the strain distribution. However, for QTF#2 the highest LITES signal was recorded on the right side of the left prong base (point A in the QTF schematic in Fig. 2.13a). At the specular point B, on the left side of the right prong end, the LITES signal was 4.2 times lower with respect to point A. This asymmetry can be ascribed to the gold electrode pattern deposited on the junction area between two prongs. Close to point A, the front surface was uncoated, allowing the laser transmission and absorption through the quartz; while a chromium film, with a strong absorption coefficient in the mid-infrared range ($> 10^5 cm^{-1}$), and a gold layer were

coated on the QTF's back surface, allowing the laser beam to be back reflected and diffused, achieving a higher thermoelastic conversion efficiency.

Conversely, close to point B, the gold layer on the front surface reflected part of the laser radiation, limiting its propagation through the quartz crystal and negatively affecting the LITES signal. The investigation of the LITES signal on the QTF plane demonstrated its dependence on the strain induced by the prong vibration as well as the influence of the gold layer pattern deposited on the quartz crystal. However, the area where the maximum strain occurs is not on the QTF plane, as shown in the simulation results reported in Fig. 2.14.
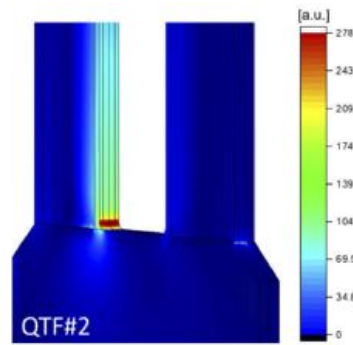
Fig. 2.14. Zoom and tilt of the COMSOL simulation results in the part of QTF#2, where the strain has a maximum (Dello Russo et al., 2018).

The area where the maximum strain occurs is located at the internal side junction of each prong. To focus the laser beam upon these areas, the QTF must be rotated along directions identified by an azimuth (φ) and a polar (Θ) angle. As the polar angle increases, the LITES signal rises, reaching the maximum ($\Theta = 27°$ for QTF#2) and then decreases for larger angles.

2.2.4 Advantages of LITES technique

As a detector, QTFs have the merits to be low-cost, small-size and can achieve a wide spectral response range without any cooling system. LITES technique has several advantages compared to other optical techniques employed for trace gas detection. Firstly, LITES-based gas sensors have superior performances by using QTF as a photothermal detector instead of commercial selective photodetectors because this technique is wavelength independent. In the study performed by Dello Russo et al., the performance of the QTF#2 (refer to Table 2.1) were compared with a commercial photodetector (THORLABS PDA10CF EC) operating in the near-

IR. The normalized spectral scans of a water absorption line, employing the LITES technique and the commercial photodetector, are shown in Fig. 2.15.
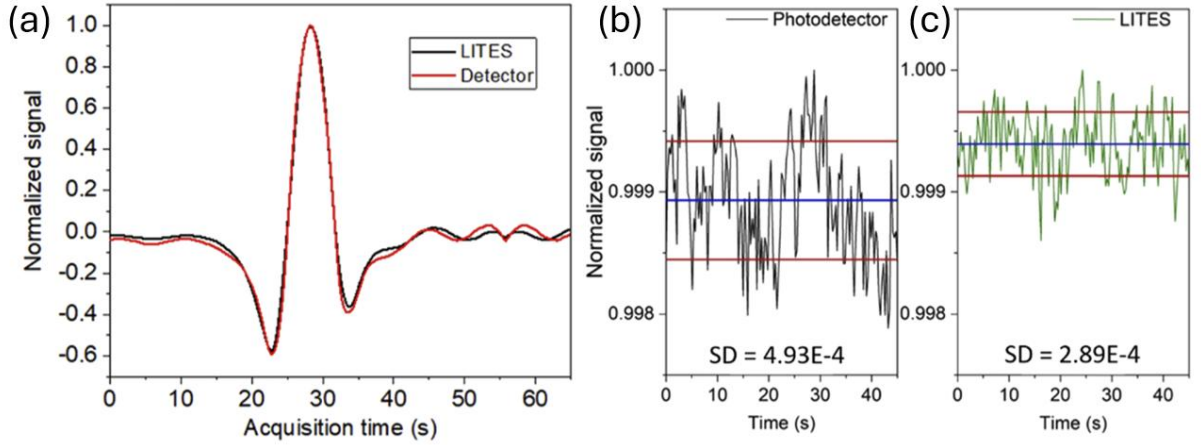

Fig. 2.15. (a) Comparison between normalized QTF#2 LITES signal (black curve) and photodetector signal (red curve); (b) Normalized photodetector signal when the laser is locked on the water absorption line; (c) Normalized LITES signal when the laser is locked on the water absorption line (Dello Russo et al., 2018).

The noise level is extracted as the standard deviation (1σ-value) of the dataset. The commercial photodetector showed an SNR of 2030, which is 1.65 times lower compared to the one obtained with the QTF#2 (SNR=3500). This result points out that QTF#2 provides higher performances for light detection compared to commercial photodetectors.

Moreover, LITES technique overcomes the disadvantage of QEPAS technique, which requires that the QTF must be placed in the gas chamber containing the target gas. This feature limits the application of QEPAS-based sensors in some application fields, such as remote gas detection and monitoring of combustion processes of hydrocarbons, in which the detection module needs to be placed far from the sample under investigation. On the contrary, in LITES technique the QTF is positioned outside the gas chamber, allowing remote gas sensing. Furthermore, custom QTFs ensure high and flat responsivity in the spectral range from 1 μm to 10 μm (Wei et al., 2021). The voltage spectral responsivity is defined as the output signal response to monochromatic incident radiation at a frequency v on a photodetector. When the light is modulated at a frequency f, the voltage responsivity $R_V(v, f)$ can be expressed as:

$$R_V(v, f) = \frac{S_V(f)}{\Delta P(v)} \qquad (2.29)$$

where $S_V(f)$ is the voltage signal due to the optical power modulation ΔP. The responsivity comparison between QTF#2 and several commercial photodetectors is shown in Fig. 2.16. The

measurements were made employing five single-mode DFB laser sources covering the infrared range, from 1.65 μm to 10.34 μm.
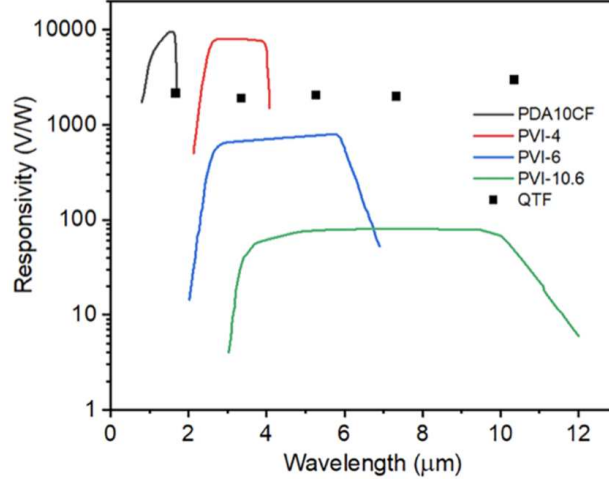

Fig. 2.16. Responsivity as a function of the wavelength for three models of photovoltaic HgCdTe detectors, namely PVI-4 (red line), PVI-6 (blue line), and PVI-10.6 (green line) provided by VIGO Photonics, for the PDA10CF InGaAs Amplified Photodetector (black line) provided by Thorlabs, Inc. and for the custom QTF#2 (datapoints) (Wei et al., 2021).

Figure 2.16 points out that the PDA10CF photodetector is confined to operate in a narrow spectral range while VIGO detectors require three different designs (PVI-4, PVI-6, and PVI-10.6) to cover the whole mid-infrared range with the disadvantage that the broader the spectral band is, the lower is the responsivity. The QTF#2 photodetector can cover the whole infrared spectral range with a flat spectral response. The responsivity does not consider the level of total intrinsic noise of the photodetector. The noise-equivalent power (NEP) is a common metric that quantifies a photodetector's ultimate sensitivity. It is defined as the signal that gives an SNR of one in a 1 Hz-output bandwidth:

$$NEP = \frac{S_N}{R_V} \qquad (2.30)$$

where S_N is the noise spectral density and R_V is the voltage responsivity. The ultimate noise level was determined by the QTF thermal noise. An average responsivity of $\sim 2.2\ kV/W$ and a NEP of 1.5 nW/Hz were achieved for the custom QTF#2, which can be flatly extended across the whole infrared spectral range 1.65 – 10.34 μm, without requiring any thermoelectrical cooling system.

Moreover, LITES-based sensors for multi-gas detection can exploit frequency-division multiplexing for simultaneous detection without replacing the detector. However, it needs to be

pointed out that, when the frequency division multiplexing is used, multiple excitation light sources are required.

QTF-based LITES sensors have the potentiality to be applied in on-field scenarios, such as environmental monitoring, combustion diagnostics, petrochemical industry, and breath analysis. One of the reasons that limit the use of QTFs as photodetectors is the requirement of an excitation light source that can be modulated in the frequency response range of the QTF (Pan et al., 2023).

Bibliography

Bell, A. (1880). On the production and reproduction of sound by light. American Journal of Science, 20 305.

Bijnen, F.G.C., Harren, F.J.M., & Reuss, J. (1996). Geometrical optimization of a longitudinal resonant photoacoustic cell for sensitive and fast trace gas detection. *Rev. Sci. Instrum.*, *67*, 2914–2923.

Blom, F. R., Bouwstra, S., Elwenspoek, M., & Fluitman, J. H. J. (1992). Dependence of the quality factor of micromachined silicon beam resonators on pressure and geometry. Journal of Vacuum Science & Technology B: Microelectronics and Nanometer Structures Processing, Measurement, and Phenomena, 10(1), 19-26.

Borri, S., Patimisco, P., Galli, I., Mazzotti, D., Giusfredi, G., Akikusa, N., ... & Spagnolo, V. (2014). Intracavity quartz-enhanced photoacoustic sensor. Applied Physics Letters, 104(9).

Campbell, S.D., Yee, S.S., & Afromowitz, M.A. (1979). Applications of photoacoustic spectroscopy to problems in dermatology research. IEEE Trans. Biomed. Eng. J., 4, 220–227.

Christen, M. (1983). Air and gas damping of quartz tuning forks. Sens. Actuators, 4, 555–554.

Dello Russo, S., Zifarelli, A., Patimisco, P., Sampaolo, A., Wei, T., Wu, H., ... & Spagnolo, V. (2020). Light-induced thermo-elastic effect in quartz tuning forks exploited as a photodetector in gas absorption spectroscopy. Optics Express, 28(13), 19074-19084.

Dong, L., Kosterev, A. A., Thomazy, D., & Tittel, F. K. (2010). QEPAS spectrophones: design, optimization, and performance. Applied Physics B, 100, 627-635.

Dong, L., Spagnolo, V., Lewicki, R., & Tittel, F.K. (2011). Ppb-level detection of nitric oxide using an external cavity quantum cascade laser based QEPAS sensor. Opt. Expr., 19, 24037–24045.

Elia, A., Lugarà, P. M., Di Franco, C., & Spagnolo, V. (2009). Photoacoustic techniques for trace gas sensing based on semiconductor laser sources. Sensors, 9(12), 9616-9628.

Fischer, C., Bartlome, R., & Sigrist, S.W. (2006). The potential of mid-infrared photoacoustic spectroscopy for the detection of various doping agents used by athletes. J. Appl. Phys. B, 85, 289–294.

Fonsen, J., Koskinen, V., Roth, K., & Kauppinen, J. (2009). Dual cantilever enhanced photoacoustic detector with pulsed broadband IR-source. *Vib. Spectrosc.*, *50*, 214–217.

Friedt, J.-M., & Carry, É. (2007). Introduction to the quartz tuning fork. Am. J. Phys., 75, 415–422.

Spagnolo, V., Patimisco, P., Borri, S., Scamarcio, G., Bernacki, B. E., & Kriesel, J. (2013). Mid-infrared fiber-coupled QCL-QEPAS sensor. Applied Physics B, 112, 25-33.

Giglio, M., Menduni, G., Patimisco, P., Sampaolo, A., Elefante, A., Passaro, V. M., & Spagnolo, V. (2019). Damping mechanisms of piezoelectric quartz tuning forks employed in photoacoustic spectroscopy for trace gas sensing. physica status solidi (a), 216(3), 1800552.

Griffith, W. (1950). Vibrational relaxation times in gases. Journal of Applied Physics, 21(12), 1319-1325.

Haas, J., & Mizaikoff, B. (2016). Advances in mid-infrared spectroscopy for chemical analysis. Annual Review of Analytical Chemistry, 9, 45-68.

Hao, Z., Erbil, A., & Ayazi, F. (2003). An analytical model for support loss in micromachined beam resonators with in-plane flexural vibrations. Sens. Actuat. A Phys., 109, 156–164.

Harren, F.J.M., Berkelmans, R., Kuiper, K., Hekkert, S.L., Scheepers, P., Dekhuijzen, R., Hollander, P., & Parker, D.H. (1999). On-line laser photoacoustic detection of ethane in exhaled air as biomarker of ultraviolet radiation damage of the human skin. Appl. Phys. Lett., 74, 1761–1763.

He, Q., Zheng, C., Liu, H., Li, B., Wang, Y., & Tittel, F.K. (2016). A near-infrared acetylene detection system based on a 1.534 µm tunable diode laser and a miniature gas chamber. Infrared Phys. Technol., 75, 93–99.

He, Y., Ma, Y., Tong, Y., Yu, X., & Tittel, F. K. (2019). Ultra-high sensitive light-induced thermoelastic spectroscopy sensor with a high Q-factor quartz tuning fork and a multipass cell. Optics letters, 44(8), 1904-1907.

Hirata, M., Kokubun, K., Ono, M., & Nakayama, K. (1985). Size effect of a quartz oscillator on its characteristics as a friction vacuum gauge. Journal of Vacuum Science & Technology A: Vacuum, Surfaces, and Films, 3(3), 1742-1745.

Hodgkinson, J., & Tatam, R.P. (2013). Optical gas sensing: A review. Meas. Sci. Technol., 24, 012004:1–012004:59.

Hosaka, H., Itao, K., & Kuroda, S. (1995). Damping characteristics of beam-shaped micro-oscillators. Sens. Actuat. A Phys., 49, 87–95.

Kosterev, A.A., Bakhirkin, Y.A., Curl, R.F., & Tittel, F.K. (2002). Quartz-enhanced photoacoustic spectroscopy, Opt. Lett. 27 1902–1904.

Kosterev, A.A., Tittel, F.K., Serebryakov, D., Malinovsky, A., & Morozov, A. (2005). Applications of quartz tuning fork in spectroscopic gas sensing. Rev. Sci. Instrum. 2005, 76, 043105:1–043105:9.

Laurila, T., Cattaneo, H., Koskinen, V., Kauppinen, J., & Hernberg, R. (2005). Diode laser-based photoacoustic spectroscopy with interferometrically-enhanced cantilever detection. Opt. Expr., 13, 2453–2458.

Lee, S., Lee, J.-Y., & Park, T.-S. (2001). Fabrication of SMD 32.768 kHz tuning fork-type crystals: Photolithography and selective etching of an array of quartz tuning fork resonators. Mater. Corros., 52, 712–715.

Lewicki, R., Jahjah, M., Ma, Y., Stefanski, P., Tarka, J., Razeghi, M., & Tittel, F. K. (2013). Current status of mid-infrared semiconductor laser based sensor technologies for trace gas sensing applications. In The Wonder of Nanotechnology: Present and Future of Optoelectronics Quantum Devices and Their Applications for Environment, Health, Security, and Energy. SPIE Press.

Li, S., Dong, L., Wu, H., Sampaolo, A., Patimisco, P., Spagnolo, V., & Tittel, F. K. (2019). Ppb-level quartz-enhanced photoacoustic detection of carbon monoxide exploiting a surface grooved tuning fork. Analytical chemistry, 91(9), 5834-5840.

Ma, Y., He, Y., Zhang, L., Yu, X., Zhang, J., Sun, R., & Tittel, F.K. (2017). Ultra-high sensitive acetylene detection using quartz-enhanced photoacoustic spectroscopy with a fiber amplified diode laser and a 30.72 kHz quartz tuning fork. Appl. Phys. Lett., 110, 031107.

Ma, Y., He, Y., Patimisco, P., Sampaolo, A., Qiao, S., Yu, X., ... & Spagnolo, V. (2020). Ultra-high sensitive trace gas detection based on light-induced thermoelastic spectroscopy and a custom quartz tuning fork. Applied Physics Letters, 116(1).

Ma, Y., Lewicki, R., Razeghi, M., & Tittel, F. K. (2013). QEPAS based ppb-level detection of CO and N2O using a high power CW DFB-QCL. *Opt. Expr.*, *21*, 1008–1019.

McCurdy, M.R., Bakhirkin, Y.A., & Tittel, F.K. (2006). Quantum cascade laser-based integrated cavity output spectroscopy of exhaled nitric oxide. Appl. Phys. B, 85, 445–452.

Olivieri, M., Zifarelli, A., Menduni, G., Di Gioia, M., Marzocca, C., Passaro, V.M.N, Sampaolo, A., Giglio, M., Spagnolo, V., & Patimisco, P. (2021). Influence of Air Pressure on the Resonance Properties of a T Shaped Quartz Tuning Fork Coupled with Resonator Tubes. Applied Sciences, 11(17):7974.

Ma, Y., He, Y., Tong, Y., Yu, X., & Tittel, F. K. (2018). Quartz-tuning-fork enhanced photothermal spectroscopy for ultra-high sensitive trace gas detection. Optics express, 26(24), 32103-32110.

Pan, Y., Zhao, J., Lu, P., Sima, C., & Liu, D. (2023). Recent Advances in Light-Induced Thermoelastic Spectroscopy for Gas Sensing: A Review. Remote Sens., 15, 69.

Patimisco, P., Sampaolo, A., Giglio, M., Dello Russo, S., Mackowiak, V., Rossmadl, H., ... & Spagnolo, V. (2019). Tuning forks with optimized geometries for quartz-enhanced photoacoustic spectroscopy. Optics Express, 27(2), 1401-1415.

Patimisco, P., Sampaolo, A., Dong, L., Tittel, F. K., & Spagnolo, V. (2018). Recent advances in quartz enhanced photoacoustic sensing. Applied Physics Reviews, 5(1).

Patimisco, P., Sampaolo, A., Dong, L., Giglio, M., Scamarcio, G., Tittel, F. K. & Spagnolo, V. (2016). Analysis of the electro-elastic properties of custom quartz tuning forks for optoacoustic gas sensing, Sens. Actuators, B 227, 539–546.

Patimisco, P., Scamarcio, G., Tittel, F. K., & Spagnolo, V. (2014). Quartz-enhanced photoacoustic spectroscopy: a review. Sensors, 14(4), 6165-6206.

Sader, J.E. (1998). Frequency response of cantilever beams immersed in viscous fluids with applications to the atomic force microscope. J. Appl. Phys., 84, 64–76.

Sampaolo, A., Menduni, G., Patimisco, P., Giglio, M., Passaro, V. M., Dong, L., ... & Spagnolo, V. (2020). Quartz-enhanced photoacoustic spectroscopy for hydrocarbon trace gas detection and petroleum exploration. Fuel, 277, 118118.

Spagnolo, V., Kosterev, A. A., Dong, L., Lewicki, R., & Tittel, F. K. (2010). NO trace gas sensor based on quartz-enhanced photoacoustic spectroscopy and external cavity quantum cascade laser. Applied Physics B, 100, 125-130.

Spagnolo, V., Patimisco, P., & Tittel, F.K. Mid-infrared Optoelectronics Materials, Devices, and Applications 1st Edition Chapter 15, Pages 597-659.

Spagnolo, V., Patimisco, P., & Tittel, F. K. (2020). Quartz-enhanced photoacoustic spectroscopy for gas sensing applications. In Mid-infrared Optoelectronics (pp. 597-659). Woodhead Publishing.

Webber, M.E., Pushkarsky, M., & Patel, C.K.N. (2003). Fiber-Amplifier-Enhanced Photoacoustic Spectroscopy with Near-Infrared Tunable Diode Lasers. *Appl. Opt*, *42*, 2119–2126.

Wei, T., Zifarelli, A., Dello Russo, S., Wu, H., Menduni, G., Patimisco, P., ... & Dong, L. (2021). High and flat spectral responsivity of quartz tuning fork used as infrared photodetector in tunable diode laser spectroscopy. Applied Physics Reviews, 8(4).

Zener, C. (1938). Internal friction in solids II. General theory of thermoelastic internal friction. Phys. Rev., 53, 90–99.

Chapter 3:

Experimental Apparatus

for benzene detection

3.1 Selection of absorption features

In the last decade, the rapid development of commercial laser sources in the mid-IR range allowed the exploration of the spectral window around 3.3 μm for BTEX detection, employing traditional optical gas sensors (Elkhazraji et al., 2024). Figure 3.1 reports the absorption features of BTEX compounds, as well as some light hydrocarbons (methane, ethane and propane), water (H_2O) and carbon dioxide (CO_2) in the spectral region around 3.3 μm, simulated using HITRAN database at 298 K and at atmospheric pressure (Gordon et al., 2022).
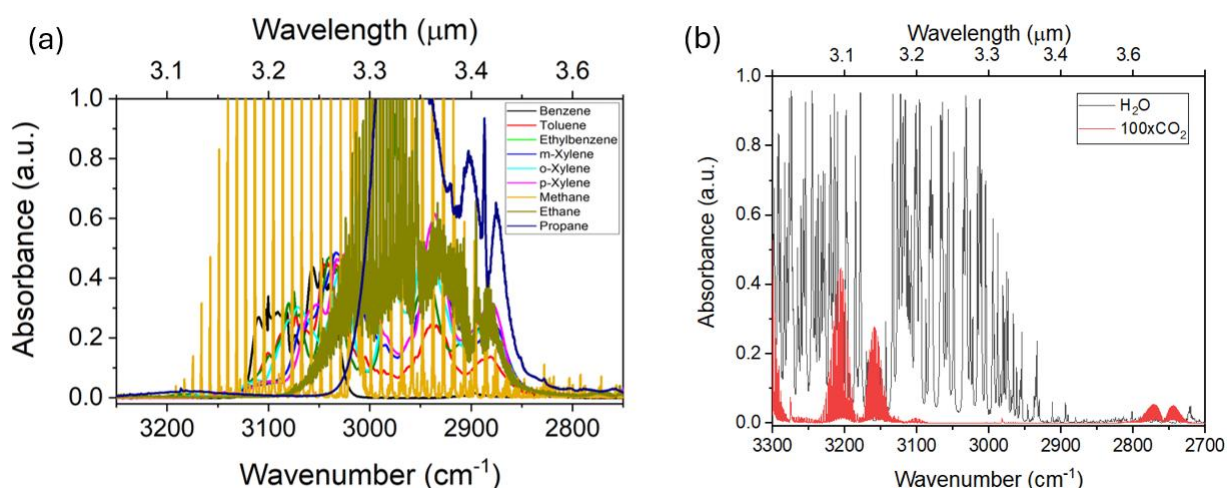
Fig. 3.1 (a) Absorption features of BTEX compounds and some light hydrocarbons in the spectral region around 3.3 μm; (b) H_2O and CO_2 absorption features in the same spectral region.

Figure 3.1 highlights the presence in this spectral region of several interferents that can compromise the selectivity of detection (Luo et al., 2022). This issue can be overcome by moving towards longer wavelength, specifically in the region $13 - 15\,\mu m$, where BTEX compounds show distinct and isolated absorption features. This spectral range is well-known for its immunity to interferences from CO_2 or H_2O. As discussed in Section 1.4, this spectral region presents two main technological challenges: i) lack of commercial laser sources; ii) performances decrease of commercial light detectors.

In this thesis work, the focus is on the detection of benzene molecule in the $13\,\mu m - 15\,\mu m$ spectral region using a custom-made QCL as light source for QEPAS and LITES techniques.

Benzene is a planar oblate symmetric top molecule with D6h point group symmetry. The molecule has 10 nondegenerate and 10 doubly degenerate vibrational modes (Pliva et al., 1982). Although C_6H_6 has 20 fundamental modes covering the spectral range $410\,cm^{-1} - 3063\,cm^{-1}$, only four fundamental modes are infrared active because of the molecule's high degree of symmetry (Smith, 2018). The four active fundamentals are: the parallel band ν_4 centered at $674\,cm^{-1}$ and three perpendicular bands ν_{12} at $3048\,cm^{-1}$, ν_{13} at $1484\,cm^{-1}$, and ν_{14} at $1038\,cm^{-1}$ (Di Lonardo et al., 1999). Figure 3.2 reports the benzene absorption spectrum in the range $600\,cm^{-1} - 4000\,cm^{-1}$ simulated at $298\,K$ and at atmospheric pressure with a resolution of $0.11\,cm^{-1}$ in HITRAN database.
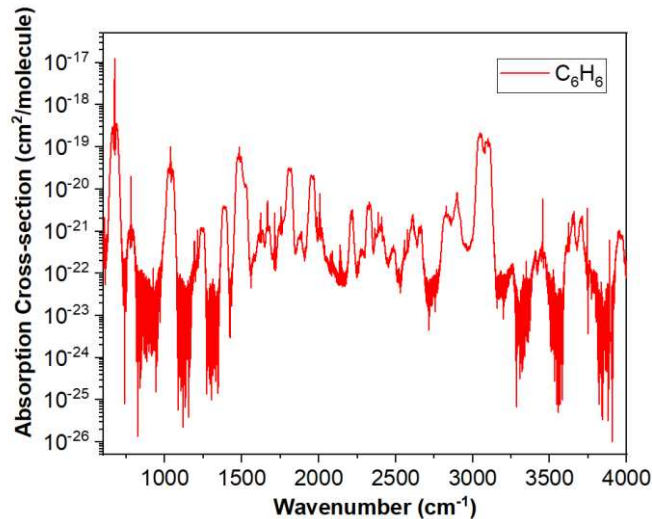
Fig. 3.2 Absorption cross section in logarithmic scale versus wavenumber of benzene molecule in the spectral range $600\,\mathrm{cm}^{-1} - 4000\,cm^{-1}$.

The parallel band ν_4 centered at $673.96\,cm^{-1}$ $(14.85\,\mu m)$ is the most intense band in the entire spectral region, with a peak value an order of magnitude higher than the other infrared bands. This absorption band correspond to aryl C–H out-of-plane bending vibration (Rinsland et al., 2008). The ν_4 band, as well as ambient CO_2 absorption features in the same spectral range $(670\,cm^{-1} - 676\,cm^{-1})$, are reported in Fig. 3.3. To make easier the visualization, the CO_2 absorption features have been multiplied by a factor of ten. The absorption spectra have been simulated in HITRAN database at $298\,K$ and at atmospheric pressure with a resolution of $0.11\,cm^{-1}$.
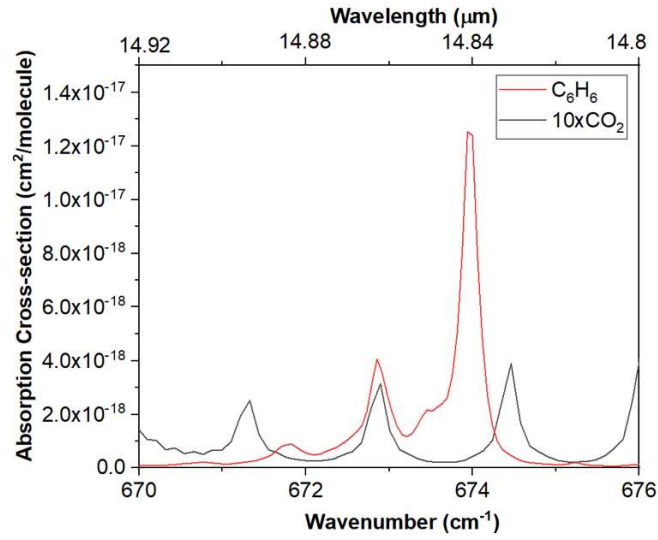
Fig. 3.3 Absorption cross section versus wavenumber of benzene molecule and CO_2 molecule in the spectral range $670 \text{ cm}^{-1} - 676 \ cm^{-1}$.

Figure 3.3 points out that CO_2 has two absorption peaks on either side of the benzene peak, which are approximately one order of magnitude weaker than the ν_4 benzene band and do not affect measurements. In this thesis, the ν_4 band was targeted using a QCL emitting at $14.85 \ \mu m$.

3.2 Experimental apparatus for QEPAS sensor

The QEPAS setup is schematically depicted in Fig. 3.4a. The sensor head, the gas line, and the electronic components used to drive the laser and acquire data are included in the schematic. Figure 3.4b shows a picture of the experimental setup.
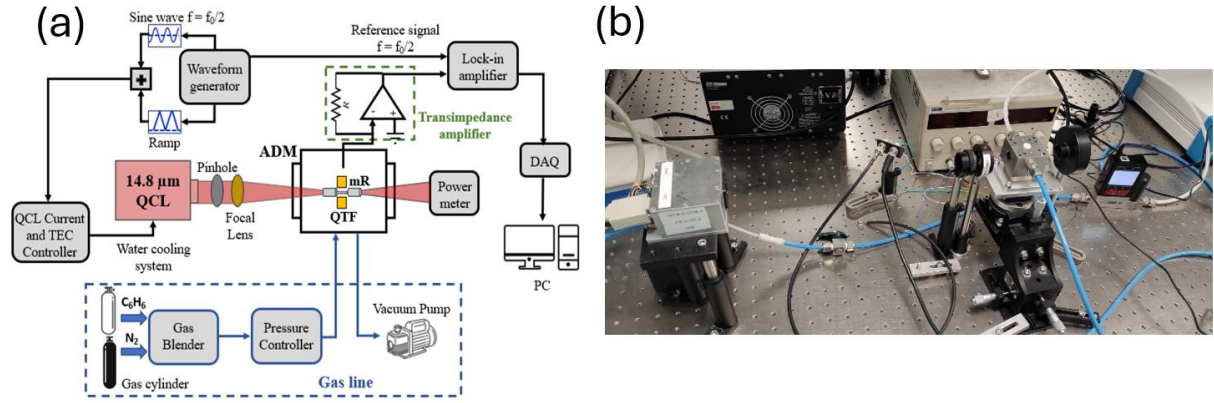
Fig. 3.4 (a) Schematic representation of the QEPAS setup; (b) QEPAS experimental apparatus employed for benzene detection.

The gas line is composed of a certified gas cylinder of 240 ppm of benzene in N_2, a gas blender to generate different mixtures, a pressure controller to set the pressure in the gas line and a vacuum pump to achieve continuous flow measurements. The employed laser source is a custom-made QCL emitting at $\lambda = 14.85 \ \mu m$, controlled by a combined laser current driver and thermoelectric cooler (TEC) controller (Thorlabs ITC4002QCL). The current driver provides the necessary current to operate the QCL, while TEC controls the operational temperature. A water-cooling system is used to regulate the heat sink temperature, assisting the Peltier cooler, installed within the QCL package, in stabilizing the internal temperature. A pinhole is used to spatially filter the laser beam, improving its quality. The laser beam is then focused into the Acoustic Detection Module (ADM) using a Zinc Selenide (ZnSe) plano–convex lens with a focal length of $50 \ mm$ and a $3 - 12 \ \mu m$ antireflection coating. The laser beam passes through the micro-resonator tubes and between the prongs of the QTF. The ADM is mounted on a five-axis stage to ensure precise optical alignment. Proper alignment is critical to prevent laser beam tail from hitting the walls of the resonator tubes and/or the QTF prongs, which would produce a non-zero background and negatively impact the ultimate noise level. During optical alignment, an optical power meter (THORLABS PM100D) was placed before and after the ADM to measure the power while passing through the spectrophone. To carry out QEPAS measurements, the wavelength modulation and $2f$ detection method was

employed (as described in Section 2.1.5). The Tektronix AFG 31000 waveform generator was used to apply a sinusoidal dither to the QCL current driver, matching half of the QTF resonance frequency, along with a slow ramp to scan across the QCL's dynamic range. A transimpedance amplifier was then used to convert the resulting QTF piezoelectric current into an electrical signal. The transduced QTF signal was demodulated by a lock-in amplifier (7265 produced by EG&G) at the QTF resonance frequency. The lock-in time constant was set to 100 ms. The demodulated signal was then digitized and saved on a personal computer using a data acquisition board (NI 779051-01), with the sampling time set to three times the lock-in time constant.

3.2.1 14.85 µm custom-made Quantum Cascade Laser source

The lack of suitable laser sources emitting above 10 μm, due to performance limitations of long wavelength semiconductor lasers, has limited the development of TDLAS-based sensors in this spectral region. QCLs are in principle the best candidate to cover the spectral range beyond 10 μm. However, the electron lifetime in the upper level of an intersubband lasing transition, which represents the main parameter responsible for the QCL optical gain, rapidly decreases as emission wavelength increases. For this reason, conventional long wavelength QCLs based on InP are unable to operate in the continuous wave (CW) regime close to room temperature. The intersubband optical gain depends on the electron effective mass m^* in the quantum wells as $m^{*-3/2}$, which makes materials with a small m^* very attractive for the development of long wavelength QCLs (Kinjalk et al., 2024). Due to the small electron effective mass, InAs-based QCLs exhibit higher optical gain compared with the InP-based counterparts and demonstrated much better performances (Benveniste et al., 2008). The development of this new technology has paved the way for the investigation of these lasers in the spectral range beyond 10 μm. In InAs-based QCLs, lasing transitions occur in InAs quantum wells. Consecutive design adjustments allowed achieving room temperature CW operation of such lasers at wavelengths up to 18 μm (Nguyen et al., 2019). A detailed discussion on the design and characteristics of recent InAs-based long wavelength QCLs can be found in Carras et al., 2008.

The laser source employed for benzene detection is an InAs-based distributed feedback (DFB) QCL emitting at $\lambda = 14.85\ \mu m,$ fabricated by molecular beam epitaxy in the InAs/AlSb material family (Kinjalk et al., 2022). The design, growth, and fabrication of this device was carried out at IES, University of Montpellier. The laser operates in CW at temperatures from

$-10 \, °C$ to $10 \, °C$. The front-view of the laser package is depicted in Fig. 3.5a. A top view of the interior of the package is shown in Fig. 3.5b.
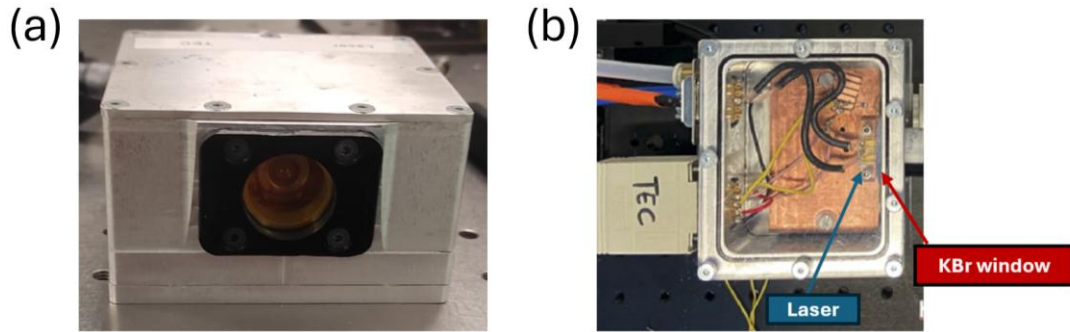

Fig. 3.5 (a) Front-view of the laser package; (b) Top-view opening the package.

The laser chip was mounted on aluminium nitride (AIN) heatsink, collimated, and packaged in a customized enclosure equipped with a PT100 temperature sensor, a Peltier cooling element and closed under dry N_2 to avoid water condensation on the laser chip (Ayache et al., 2022). External water cooling is available in the enclosure to aid in extracting heat generated by the Peltier element. The TEC consumption depends on the cooling water temperature. For the QCL operation in the range $-15 \, °C$ to $+5 \, °C$ and water temperature in the range $20 \, °C$ to $30 \, °C$, the TEC electrical power is $< 40 \, W$ and the TEC current limit is $< 4.5 \, A$. A double-lens optical system can provide more precise adjustment of the focal point within the QEPAS spectrophone. However, a single-lens mount was chosen to minimize optical power loss. The emission spectrum of the employed QCL, recorded at a temperature of $-10 \, °C$ with injected current of $750 \, mA$ is reported in Fig. 3.6.
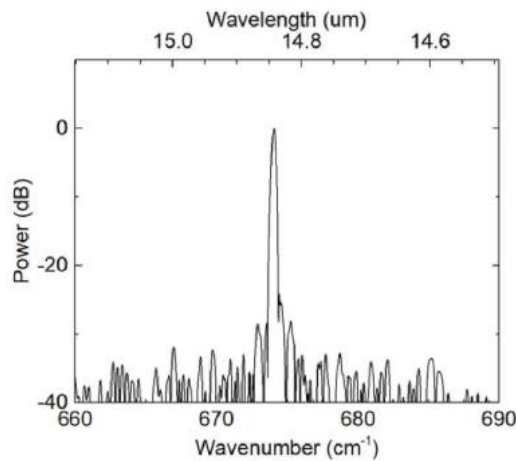

Fig. 3.6 Emission spectrum of the quantum cascade laser recorded at a temperature of $-10 \, °C$ and injected current of 750 mA (Ayache et al., 2022).

The laser source exhibits a very good spectral purity, suitable for QEPAS spectroscopy, with a side mode suppression ratio (SMSR) of $30\ dB$. The spectral emission can be tuned by varying the injected current. Figure 3.7 shows the spectral absorption coefficient of benzene molecule at atmospheric pressure simulated by using NIST database. Additionally, the datapoints depict the wavelength tuning range of the QCL at $-5\ °C$ as a function of the injection current.
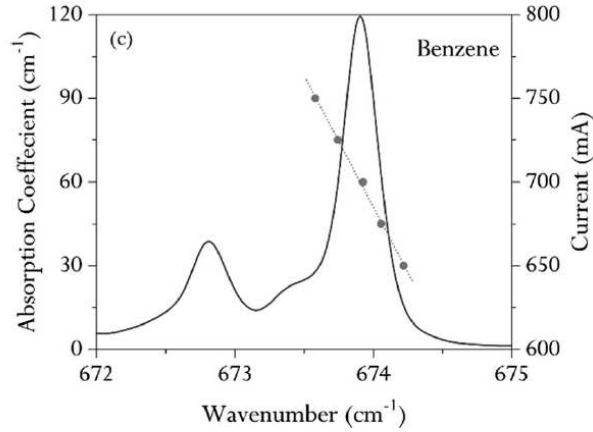

Fig. 3.7 Solid lines represent the simulated absorption coefficient for pure benzene at atmospheric pressure. Dotted lines and datapoints mark the QCL wavelength tuning ranges as a function of the QCL injection current (Kinjalk et al., 2024).

This spectral analysis confirms that the QCL can efficiently excite the most intense benzene absorption feature located at $14.85\ \mu m$.

3.2.2 Acoustic Detection Module (ADM)

The employed Acoustic Detection Module (ADM01) is supplied by Thorlabs, Inc. A picture of the ADM01 is provided in Fig. 3.8a. This module features two gas connection ports - an inlet and an outlet - enabling the gas to be introduced into the airtight chamber. The gas ports are equipped with standard Hylok stainless steel tube fittings for 6 mm tubing. The bottom of the ADM01 module includes an 8-32 (M4) tap for mounting to on a 5-Axis Stage. The ADM01 has two Ø1/2" uncoated BaF_2 wedged windows, with a transmittance spectral range from $200\ nm$ to $11\ \mu m$. The ADM01 module includes the spectrophone, which consists of a QTF and two micro-resonator tubes on either side of the QTF (Fig. 3.8b). The laser beam passes through the wedged windows and through the micro-resonator tubes. When the spectrophone is excited, the generated QTF signal is amplified by the integrated high-gain transimpedance preamplifier, ensuring an excellent signal-to-noise ratio (SNR).

The QTF mounted in the ADM01 is the QTF-S08-T (Fig. 3.8b), it provides the highest QEPAS SNR (Patimisco et al., 2019). This QTF has the following geometrical parameters: prong width ($T_1 = 2\ mm$ and $T_2 = 1.4\ mm$), prong length ($L = 9.4\ mm$) and thickness ($w = 0.25\ mm$) (Fig. 3.8c).
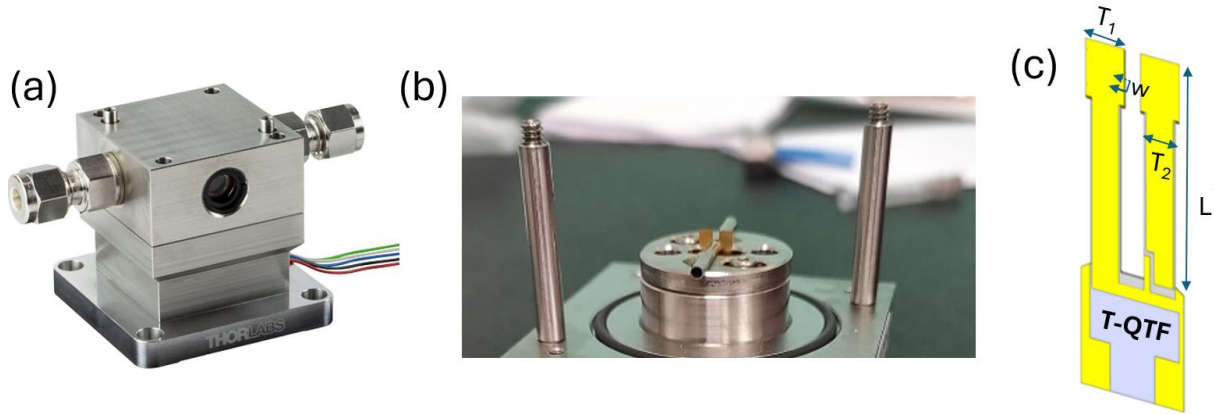

Fig. 3.8 (a) Commercial ADM01 produced by Thorlabs, Inc; (b) Spectrophone composed of the QTF and two micro-resonator tubes on either side of the QTF opening the cap of the ADM; (c) sketch of the QTF with the geometrical parameters.

As shown in Fig. 3.8b, the micro-resonator tubes are glued on a V-groove. The main geometrical parameters of the tubes influencing sensor performance are: i) the length of the tubes; ii) the internal diameter of the tubes; iii) the spacing between the tubes and the surface of the QTF; iv) the prong spacing. In 2016, Patimisco et al. reported a detailed investigation of the geometrical parameters of micro-resonator tubes, as well as their influence on QEPAS sensing performance. The QEPAS signal is maximized when the tubes are positioned about 200 μm far from the QTF surface, with the tube center positioned $2\ mm$ below the QTF top. The optimal tube length and internal diameter are $l = 12.4\ mm$ and $ID = 1.59\ mm$, respectively. With these conditions, the signal-to-noise ratio (SNR) of the spectrophone was enhanced by approximately a factor of 60 compared to that of a bare QTF. The main technical specifications of the commercial ADM01 are summarized in Table 3.1.

Tab. 3.1 Technical specifications of the ADM01 commercialized by Thorlabs, Inc.

Resonance Frequency f_0	$\sim 12,455\ Hz$ at atmospheric pressure
Q Factor	$> 12,000$
Volume Sample Chamber	$7\ cm^3$
Micro-resonator Tubes	Inner Diameter: $1.59\ mm$ Length, Each: $12.4\ mm$
Wedged Windows	Ø1/2" uncoated BaF$_2$ windows transmission range $200\ nm - 11\ \mu m$
Gas Connectors	G1/8 Straight for 6 mm Tubing
Recommended Gas Flow	$< 200\ sccm$ (standard cubic centimeter per minute)
Maximum Gas Pressure	$1.5\ bar$

The resonance frequency and the Q-factor of the spectrophone included in the ADM01 are $f \sim 12,455\ Hz$ and $Q > 12,000$, respectively, at atmospheric pressure. The QTF operates in a small sample volume, enabling fast and real-time gas sampling. The recommended gas flow is up to $200\ sccm$ and the maximum gas pressure is $1.5\ bar$. The pinout connections of the transimpedance amplifier integrated in the ADM01 are reported in Table 3.2.

Tab. 3.2 Electrical connections of the ADM01.

Color	Purpose	Comment
Red	+ 12 V	Recommended Voltage, up to 24 V maximum
Black	GND	-
Blue	- 12 V	Recommended Voltage, up to - 24 V maximum
White	MODULATION IN	Electrical Modulation (sine) IN for QTF characterization
Green	SIGNAL OUT	Amplified QTF signal OUT

		Linear p to 1.8 V, 50 Ω termination

The red and blue wires represent positive and negative supply voltage of the QTF, respectively, and the black one is the ground. The white wire should be connected only for electrical excitation of the QTF during its characterization. The green wire carries the amplified output signal from the QTF.

The QTF converts the mechanical strain induced by acoustic waves into a current signal, which is proportional to the concentration of the target gas. However, this signal must be processed by appropriate front-end electronics to yield useful information about the analyte concentration. The first stage in the QTF signal conditioning chain is an analog preamplifier, which is integrated in the commercial ADM01. It converts the piezo-current into a voltage signal, which is amplified to increase the amplitude of the output signal. A schematic of the transimpedance amplifier used for the QTF readout is shown in Fig. 3.9.
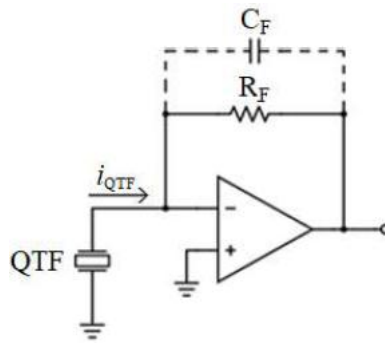

Fig. 3.9 Transimpedance amplifier configuration.

The QTF piezo-current is converted to a voltage signal by means of the feedback resistor R_F. The dashed capacitor C_F represents the stray capacitance associated to R_F. If the impedance of C_F is not negligible compared to R_F, it acts as a lowpass filter with a time constant $\tau_F = R_F \cdot C_F$, significantly attenuating the output signal (Starecki et al., 2017).

3.2.3 Gas handling system

The gas handling system includes certified gas cylinders, a gas blender, a pressure controller, a needle valve, and a vacuum pump. The gas cylinder employed in the experiment is a certified mixture of 240 ppm of C_6H_6 in N_2. The pressure controller/flow meter, in conjunction with a needle valve and a vacuum pump, is used to precisely regulate gas pressure and flow rate within the gas line and achieve continuous flow measurements. The gas line connects the ADM to the

pump on the outlet side and to the pressure controller on the inlet side (see Fig. 3.4a). Upstream, the gas blender is used to precisely control the flow rate of each individual gas channel and produce the desired gas mixtures. In this thesis work, the employed gas blender is the MCQ GB100 supplied by MCQ Instruments (Fig. 3.10).
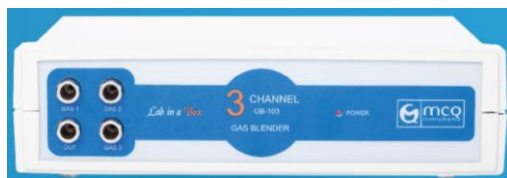

Fig. 3.10 MCQ GB100 gas blender produced by the MCQ Instruments.

The MCQ GB100 features three inputs channels and one output for the defined output mixture. The end user only needs to set the total flow at the output channel and the percentage of each gas concentration in the output mixture. The gas blender automatically set the flow needed for each channel. One input is a cylinder containing pure N_2 as the gas carrier, while the other is a cylinder with a certified mixture of the target gas in N_2. In this way, several mixtures with different gas target concentrations can be obtained starting from the certified 240 ppm of C_6H_6 in N_2 cylinder and diluting it in N_2. The main technical specifications of the MCQ GB100 are reported in Tab. 3.3.

Tab. 3.3 Main technical specifications of the MCQ GB100 gas blender.

Mass flow rate	$0.5 - 500 \ mL/min$
Accuracy	1%
Repeatability	0.16%
Response time	$50 \ ms$

The pressure controller employed is the Alicat MC3S-D supplied by the Alicat Scientific (Fig. 3.11).

Fig. 3.11 Alicat MC3S-D pressure controller produced by Alicat Scientific.

The desired pressure in the gas line can be set by using dedicated software. The main technical specifications of the pressure controller are: i) $\pm 0.125\%$ of full-scale accuracy; ii) $\pm 0.08\%$ of full-scale repeatability; iii) $0.01\% - 100\%$ measurement and control range (10,000:1 turndown).

3.2.4 Signal processing system

The amplified signal in output from the ADM is then fed to a lock-in amplifier (LIA), used for extracting a desired harmonic component of the input signal even in an extremely noisy environment. The use of a LIA in the signal conditioning chain of a QEPAS sensor allows the enhancement of the signal-to-noise ratio (SNR), thus improving the sensitivity of the sensing system (Di Gioia et al., 2023). LIAs exploit phase-sensitive detection technique to single out the component of a signal at a specific reference frequency and phase. The noise signal, at frequencies and phases different from the reference frequency, are filtered and do not affect the measurement. This technique is based on a mixer and an adjustable low-pass filter (LPF) to retrieve the output signal. In particular, the LPF influences the noise level at the output of the LIA; therefore, the choice of the correct LPF time constant is crucial. The time constant has been set to $100\ ms$ in all the experiments. The LIA employed in this thesis work is the 7265 produced by EG&G. It has two phase sensitive detectors and can work both with internal and external reference. The auto-phase function allows to phase shift the reference channel to cancel the phase difference. Figure 3.12 presents the scheme of a dual-phase lock-in amplifier employed in QEPAS and LITES measurements.
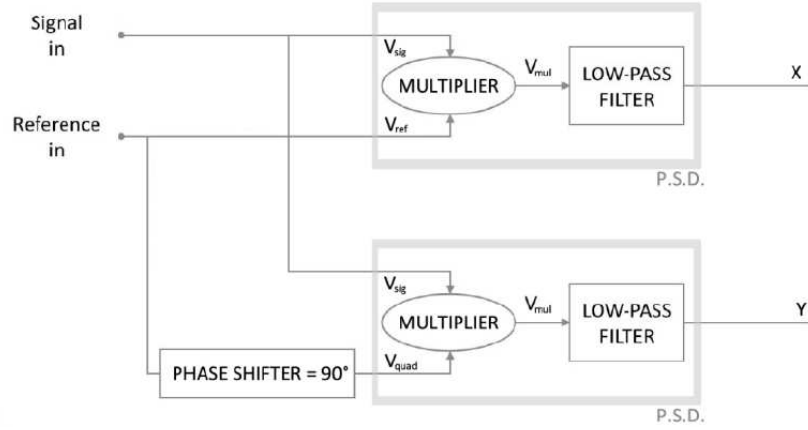
Fig. 3.12 Scheme of a dual-phase lock-in amplifier.

The transimpedance amplifier output signal (V_{sig}) is mixed with a reference signal (V_{ref}) generated by an oscillator (typically the TTL output of a waveform generator) and with its 90-phase shifted version. Then a LPF preserves the DC components at the output of the mixers. Therefore, by choosing the frequency f_{ref} of the signal V_{ref} equal to the frequency f_s of the signal V_{sig}, the LPF output signal will depend on the amplitude of V_{sig} and on the phase shift ϕ between V_{sig} and V_{ref}. On top of that, the output signal will be influenced only by the noise component around the reference frequency, thus getting rid of the noise floor overlapping to the input signal. The X output signal of the LIA is referred to as in-phase component, since it reaches its maximum value when the phase shift ϕ is zero, and is given by:

$$X = A_{sig} \cdot cos\,(\phi) \tag{3.1}$$

where A_{sig} is the amplitude of the input signal. The Y output signal is referred to as out-of-phase component, and is given by:

$$Y = A_{sig} \cdot sin(\phi) \tag{3.2}$$

Starting from these components, it is possible to retrieve the amplitude R of the output signal, which is phase-independent, and the phase shift ϕ with the following expressions:

$$R = \sqrt{X^2 + Y^2} \propto A_{sig} \tag{3.3}$$

$$\phi = arctg\left(\frac{Y}{X}\right)$$

A dual-phase lock-in can measure X and Y signals at the same time and the phase shift ϕ. The demodulated signal in output from the LIA is then digitized using a data acquisition board with the sampling time set to three times the lock-in time constant and finally saved on a personal computer. A custom LabView program has been developed to read the signals from the data acquisition board and show the obtained signal in function of time on the PC.

3.3 Experimental apparatus for LITES sensor

The LITES setup is illustrated schematically in Fig. 3.13a and depicted in a photograph in Fig. 3.13b.
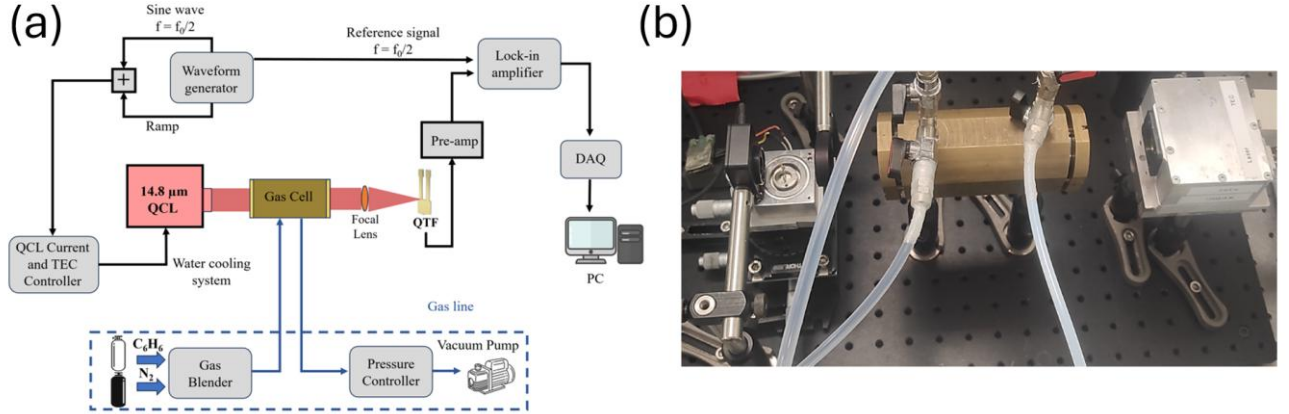
Fig. 3.13 (a) Schematic representation of the LITES setup; (b) LITES experimental apparatus employed for benzene detection.

The QCL laser beam passes through a brass gas cell with an internal diameter of $4\ cm$ and length of $12\ cm$. As for the QEPAS setup, a current driver and TEC control (THORLABS ITC4002) are employed to polarize the QCL and regulate its temperature, respectively. The external water-cooling system is used to efficiently extract the extra-heating. The light exiting the gas cell is then focused on the bare QTF, used as infrared photodetector, with a Ø1" ZnSe plano-convex lens having a focal length of $25\ mm$ and a $7 - 12\ \mu m$ antireflection coating. As for QEPAS, the LITES setup operates at wavelength modulation and second harmonic detection: the modulation frequency of the laser source was set to half of the resonance frequency of the QTF using the KEYSIGHT EDU33212A waveform generator. As detailed in Section 2.2.2, when the QTF is used as an infrared photodetector, the modulation of the optical power incident on the QTF surface causes periodic heating/cooling cycles. They induce changes in the accumulated charges on the QTF surface due to quartz's piezoelectric properties. Consequently, the electric signal generated by the QTF is proportional to both the intensity of the strain field produced on the QTF and to the resonator's accumulation time. The piezoelectric current generated by the QTF is converted into an electric signal by means of a custom transimpedance preamplifier and then demodulated by a lock-in amplifier (7265 produced by EG&G) at the QTF resonance frequency. The lock-in time constant was set to $100\ ms$. The gas handling system is the same as for the QEPAS setup.

3.3.1 Gas absorption cell

The gas absorption cell used in this thesis work is depicted in Fig. 3.14a. It is constructed from brass, with an internal diameter of $4\ cm$ and length $12\ cm$, and features two windows made of Germanium. The leakage test of the gas cell is reported in Fig 3.14b.
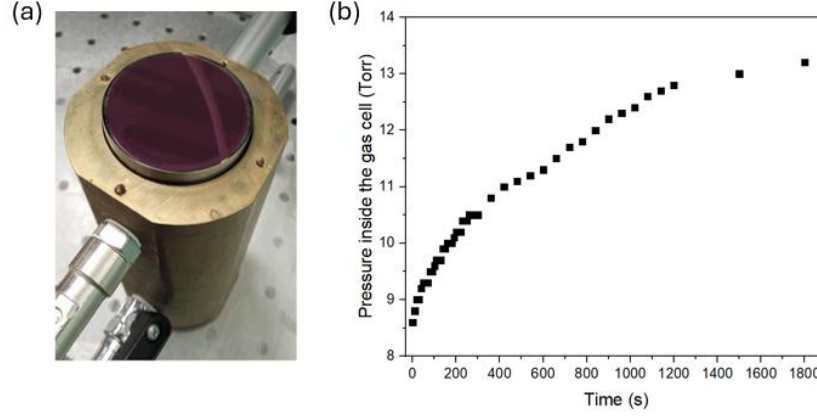

Fig. 3.14 (a) Employed gas absorption cell; (b) Leakage test of the gas cell.

Optical windows with appropriate diameter and antireflection coating for $14.85\ \mu m$ are not commercially available. Therefore, germanium optical windows with a diameter of $40\ mm$ and thickness of $4\ mm$, with a $3\ \mu m - 12\ \mu m$ AR coating as shown in Fig. 3.15, were used instead.
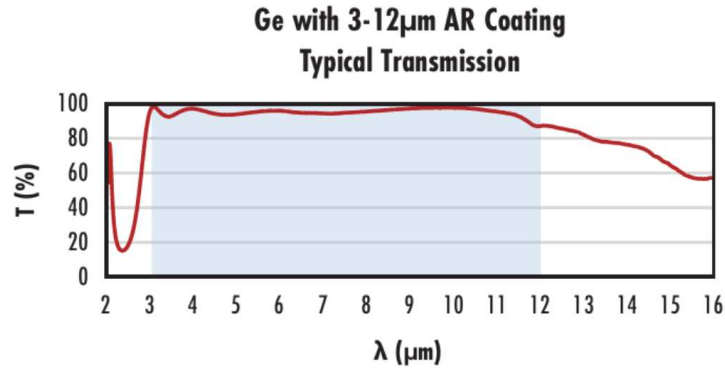

Fig. 3.15 Transmission spectrum of a $3\ mm$ thick germanium window with a $3 - 12\ \mu m$ AR coating.

The blue shaded region represents the wavelength range of the coating design, which features a mean reflectivity of $R_{avg} < 5.0\%$ in the $3 - 12\ \mu m$ range. Consequently, the operating wavelength falls outside the spectral range of the AR coating.

3.3.2 Custom made bare QTF

The QTF employed in LITES setup is a T-shaped QTF with 50 μm-deep rectangular grooves carved on both prong sides, named QTF#2 in Table 2.1 (Dello Russo et al., 2020). A sketch of the T-shaped QTF is reported in Fig. 3.16a. The prong has a full length of $L = L1 + L2 = 9.4\ mm$, a crystal thickness of $T = 250\ \mu m$, and W1 and W2 are $2\ mm$ and $1.4\ mm$, respectively. The fundamental mode has a resonance frequency of $\sim 9781\ Hz$ and a Q-factor of $\sim 10,500$ at atmospheric pressure. With respect to standard QTFs, the T-shaped geometry with a carved surface prong allows the reduction of the resonance frequency and electrical resistance, while retaining a high Q-factor. In addition, the mass added on top of each prong results in an increase in the strain intensity close to the QTF prong's clamped end.
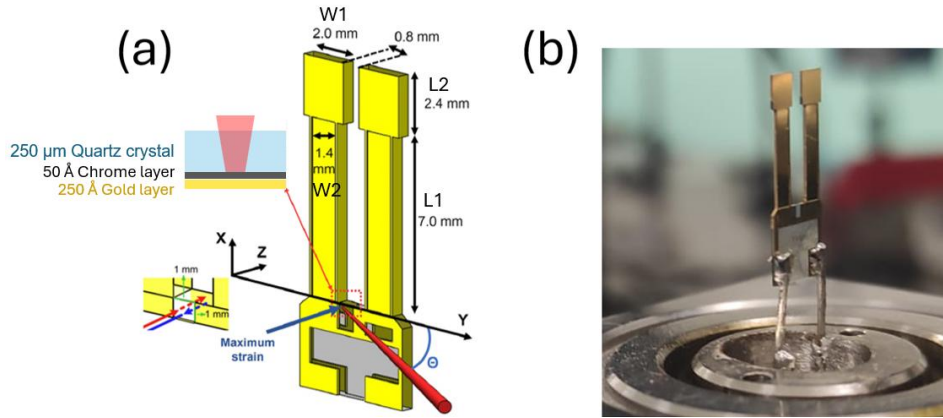

Fig. 3.16. (a) Sketch of the T-shaped QTF with its geometrical parameters; (b) T-shaped QTF with 50 µm-deep rectangular grooves carved on both prong sides employed for LITES measurements.

In 2021 Wei et al. studied the response characteristic of the T-shaped grooved QTF in a wide spectral range, from $1.65\ \mu m$ to $10.34\ \mu m$, starting from the investigation on the absorption of the different materials composing the QTF, i.e., quartz, chrome, and gold. The measured transmittance spectrum of a $0.75\ mm$-thick Z-cut α-quartz over the wavelength range $1 - 11\ \mu m$, shown in Fig. 3.17, was measured using a Fourier transform spectrometer.
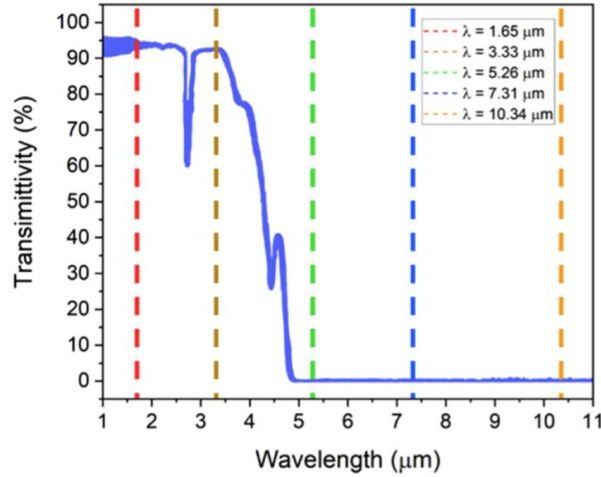
Fig. 3.17. Transmittance spectrum of a 0.75 mm-thick Z-cut α-quartz over the wavelength range 1–11 μm measured using a Fourier transform spectrometer (Wei et al., 2021).

A high transmissivity ($> 90\%$) was obtained in the spectral range $1 - 3.5\,\mu m$, and then it rapidly decreased in the range $3.5 - 4.8\,\mu m$. The narrow absorption features around $2.7\,\mu m$ and $4.2\,\mu m$ are related to H_2O and CO_2 absorption, respectively. For $\lambda > 4.8\,\mu m$, transmissivity reaches values close to zero. The low-energy edge of the transmissivity band is determined by the thickness of the sample as well as the optical absorption coefficient. The spectral dependence of absorbance reflects that of the optical absorption coefficient (Wei et al., 2021): for $\lambda > 4.8\,\mu m$, almost all the electromagnetic energy is absorbed on QTF surface with a penetration depth of tens of microns that can generate local heating. Conversely, for $\lambda < 4.8\,\mu m$, the light passes through the entire quartz sample and the energy deposited is not sufficient to efficiently stimulate thermoelastic effects. To achieve a high thermoelastic conversion efficiency in the whole infrared spectral range, the corresponding back area in Fig. 3.16a was coated with dielectric/metallic films composed of a chrome film and a gold layer. The QTF is realized with an uncoated front surface and a chromium/gold layer-coated back surface, where the light is supposed to be focused. In this way, the section of the QTF consists of a 250 μm thick α-quartz crystal (Z-cut), a 50 Å-thick chrome film and a 250 Å-thick gold layer (Wei et al., 2021). The absorption coefficient of quartz and chromium at different wavelengths are reported in Tab. 3.4.

Tab. 3.4. Absorption coefficient of quartz and chromium at different wavelengths.

	QUARTZ	CHROMIUM
$\lambda \ (\mu m)$	$\alpha \ (cm^{-1})$	$\alpha \ (cm^{-1})$
1.65	1.523	3.92×10^5
3.33	7.170	3.89×10^5
5.26	21.911	4.06×10^5
7.31	130.5	4.13×10^5
10.34	1507.6	4.12×10^5

Chromium exhibits a high absorption coefficient in the mid-infrared range, and it is an excellent adhesion promoter between quartz and gold. The deposition of a chromium film and a highly reflective gold layer traps the electromagnetic energy at the quartz/chromium interface. Considering a round trip of 100 Å in the chromium layer, the Lambert–Beer law predicts an attenuation of the incident light of ~80%. Thus, it is reasonable to assume that after a second-round trip, the light is completely absorbed within the chromium layer.

Bibliography

Ayache, D., Trzpil, W., Rousseau, R., Kinjalk, K., Teissier, R., Baranov, A. N., ... & Vicet, A. (2022). Benzene sensing by quartz enhanced photoacoustic spectroscopy at 14.85 μm. Optics Express, 30(4), 5531-5539.

Benveniste, E., Vasanelli, A., Delteil, A., Devenson, J., Teissier, R., Baranov, A., ... & Sirtori, C. (2008). Influence of the material parameters on quantum cascade devices. Applied Physics Letters, 93(13).

Carras, M., Garcia, M., Marcadet, X., Parillaud, O., De Rossi, A., & Bansropun, S. (2008). Top grating index-coupled distributed feedback quantum cascade lasers. Applied physics letters, 93(1).

Dello Russo, S., Zifarelli, A., Patimisco, P., Sampaolo, A., Wei, T., Wu, H., ... & Spagnolo, V. (2020). Light-induced thermo-elastic effect in quartz tuning forks exploited as a photodetector in gas absorption spectroscopy. Optics Express, 28(13), 19074-19084.

Di Gioia, M., Lombardi, L., Marzocca, C., Matarrese, G., Menduni, G., Patimisco, P., & Spagnolo, V. (2023). Signal-to-Noise Ratio Analysis for the Voltage-Mode Read-Out of Quartz Tuning Forks in QEPAS Applications. Micromachines, 14(3), 619.

Di Lonardo, G., Fusina, L., Masciarelli, G., & Tullini, F. (1999). Integrated band strengths of benzene vapour in the 600–1900 cm^{-1} region. Spectrochimica Acta Part A: Molecular and Biomolecular Spectroscopy, 55(7-8), 1535-1544.

Elkhazraji, A., Sy, M., Mhanna, M., Aldhawyan, J., Khaled Shakfa, M. and Farooq, A., "Selective BTEX detection using laser absorption spectroscopy in the CH bending mode region," Exp. Therm. Fluid Sci. 151, 111090 (2024).

Gordon, I. E., Rothman, L. S., Hargreaves, E. R., Hashemi, R., Karlovets, E. V., Skinner, F. M., ... & Yurchenko, S. N. (2022). The HITRAN2020 molecular spectroscopic database. Journal of quantitative spectroscopy and radiative transfer, 277, 107949.

Kinjalk, K., Díaz-Thomas, D. A., Loghmari, Z., Bahriz, M., Teissier, R. and Baranov, A. N., "InAs-Based Quantum Cascade Lasers with Extremely Low Threshold," Photonics 2022, Vol. 9, Page 747 9(10), 747 (2022).

Kinjalk, K., Paciolla, F., Sun, B., Zifarelli, A., Menduni, G., Giglio, M., ... & Spagnolo, V. (2024). Highly selective and sensitive detection of volatile organic compounds using long wavelength InAs-based quantum cascade lasers through quartz-enhanced photoacoustic spectroscopy. Applied Physics Reviews, 11(2).

Luo, P., Harrist, J., Menduni, G., Mesdour, R., Stmichel, N. and Sampaolo, A., "Simultaneous Detection of Methane, Ethane, and Propane by QEPAS Sensors for On-Site Hydrocarbon Characterization and Production Monitoring" (2022).

Nguyen Van, H., Loghmari, Z., Philip, H., Bahriz, M., Baranov, A. N., & Teissier, R. (2019, March). Long wavelength (λ> 17 μm) distributed feedback quantum cascade lasers operating in a continuous wave at room temperature. In Photonics (Vol. 6, No. 1, p. 31). MDPI.

Patimisco, P., Sampaolo, A., Zheng, H., Dong, L., Tittel, F. K., & Spagnolo, V. (2016). Quartz–enhanced photoacoustic spectrophones exploiting custom tuning forks: a review. Advances in Physics: X, 2(1), 169-187.

Pliva, J., & Pine, A. S. (1982). The spectrum of benzene in the 3-μm region: The ν12 fundamental band. Journal of Molecular Spectroscopy, 93(1), 209-236.

Rinsland, C. P., Devi, V. M., Blake, T. A., Sams, R. L., Sharpe, S., & Chiou, L. (2008). Quantitative measurement of integrated band intensities of benzene vapor in the mid-infrared at 278, 298, and 323 K. Journal of Quantitative Spectroscopy and Radiative Transfer, 109(15), 2511-2522.

Smith, B. C. (2018). Infrared spectral interpretation: a systematic approach. CRC press.

Starecki, T., & Wieczorek, P. Z. (2017). A high sensitivity preamplifier for quartz tuning forks in QEPAS (quartz enhanced photoacoustic spectroscopy) applications. Sensors, 17(11), 2528.

Wei, T., Zifarelli, A., Dello Russo, S., Wu, H., Menduni, G., Patimisco, P., ... & Dong, L. (2021). High and flat spectral responsivity of quartz tuning fork used as infrared photodetector in tunable diode laser spectroscopy. Applied Physics Reviews, 8(4).

Chapter 4:
Experimental Results

4.1 QEPAS sensor for benzene detection

4.1.1 Laser Characterization

The $14.85\,\mu m$ custom-made QCL used to target the v_4 benzene absorption band was characterized both electrically and spectrally. Figure 4.1 reports the emitted laser optical power measured by the THORLABS PM100D optical power meter at the output window of the laser as a function of the laser injected current, at different operating temperatures.
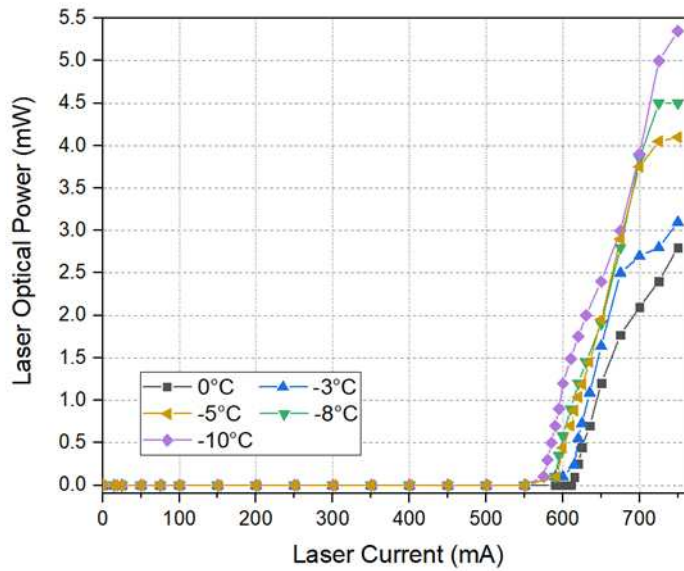

Fig. 4.1. Current-Power QCL characteristic at different operating temperatures.

The current-power characteristic describes the trend of the optical output power of the QCL at different injected currents. An important parameter is the threshold current, which represents the minimum current required for lasing. Below the threshold current, the emitted photons are mainly due to spontaneous emission. Above the threshold, stimulated emission dominates and the optical output power increases linearly with increasing current; this represents the operating region in which the QCL operates efficiently. Further increasing the current, the characteristic starts to deviate from linearity due to several factors, such as thermal effects, carrier leakage, or saturation of the gain medium (Behringer, 2007). The threshold current decreases as the temperature reduces. The temperature dependence of the threshold current density is usually

described by an exponential function (Bazhenov et al., 2005). Moreover, by increasing the operating temperature of the QCL, intrinsic losses raise, causing a reduction of the optical output power dynamic range. For example, as reported in Fig. 4.1, the threshold current was $615\ mA$ at $0\ °C$, with a maximum emitted optical power of $2.8\ mW\ at\ 750\ mA$. Decreasing the operating temperature up to $-10\ °C$, the threshold current reduced to $575\ mA$, with the maximum emitted power increased up to $5.4\ mW\ at\ 750\ mA$. A good trade-off between QCL's good performance and operating conditions for reconstructing the benzene absorption feature was found setting the operating temperature to $-5\ °C$. Figure 4.2 depicts the QCL operating voltage and the emitted optical power as a function of the injected laser current at $-5\ °C$.

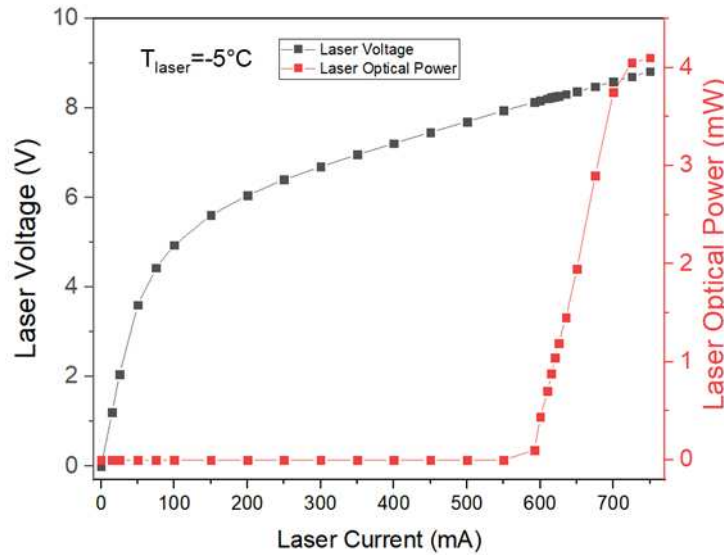**Fig. 4.2.** Current-Power and Current-Voltage QCL characteristics at -5 °C.

The current-voltage characteristic voltage rapidly increases with current up to a knee value; above it, the voltage increases linearly with current. At $-5\ °C$, the threshold current was $592\ mA$ and the maximum emitted power reached $4.1\ mW\ at\ 750\ mA$.

The QCL's emission wavelength was measured using a Fourier spectrometer (Nicolet™ iS50, Thermo Scientific) which allows the acquisition of high-resolution data with a spectral resolution of $0.125\ cm^{-1}$, over a wide spectral range. The laser beam was collimated and directed to the beam splitter of the spectrometer using a parabolic mirror. By changing the injected laser current and the operating temperature, the emission wavelength can be tuned to match the v_4 absorption peak at $673.95\ cm^{-1}$ of the benzene band. The QCL emission

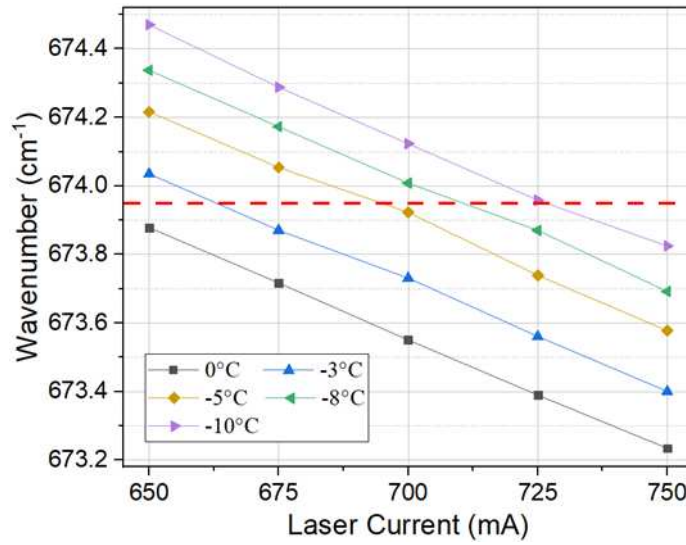wavenumber as a function of the laser injection current at different operating temperatures is depicted in Fig. 4.3.

Fig. 4.3. Laser emission wavelength, in wavenumbers, as a function of the laser injection current at different laser operating temperatures. The red dashed line represents the spectral location $(673.95\ cm^{-1})$ of the targeted v_4 benzene absorption band.

The red dashed line represents the spectral position $(673.95\ cm^{-1})$ of the targeted v_4 benzene absorption band. The choice of the operating temperature to $-5\ °C$ was chosen to fulfil the requirement to full reconstruct the benzene absorption band with highest optical power range available. As pointed out in Figure 4.3, at $-5\ °C$ the QCL can be tuned between $674.14\ cm^{-1}\ (at\ 650\ mA)$ and $673.52\ cm^{-1}\ (at\ 750\ mA)$. At $-5\ °C$, the injection current at which the benzene absorption peak is expected to be targeted was $693\ mA$. The slope of the linear fit of the experimental data at $-5\ °C$ in Fig. 4.3 represents the QCL tuning rate, resulting in $\sim 0.0064\ cm^{-1}/mA$.

The far-field spatial intensity distribution of the laser beam was acquired using an infrared pyrocam (Pyrocam IIIHR, Ophir Optronics Solutions Ltd). The Pyrocam IIIHR is a high performance, solid-state, pyroelectric camera that features a $12\ mm$ imager (160×160 pixels) and 16-bit A/D converter. The laser beam profile at the output window of the QCL is depicted in Fig. 4.4.
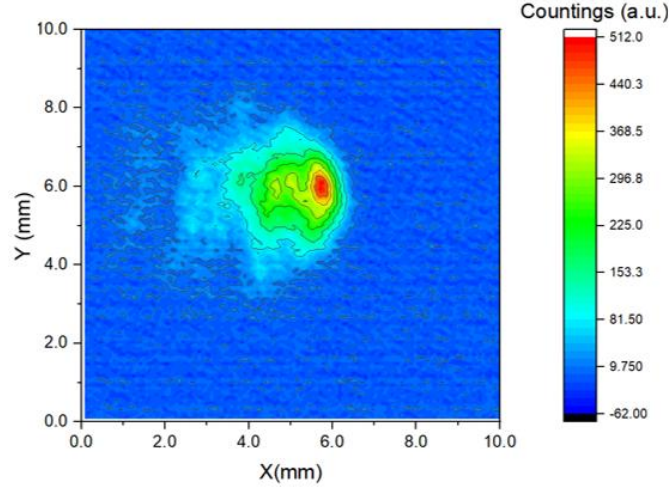
Fig. 4.4. Laser beam profile at the output window of the QCL.

The laser beam profile exhibits a no Gaussian-like profile, with some tails on side. Plotting the data acquired by the pyrocam in Origin software (OriginLab), it is possible to evaluate the core of the distribution of the laser beam, whose dimension has been estimated as $1.4 \times 1.6 \ mm^2$, in X and Y direction, respectively. To spatially filter out tails and improve the spatial quality of the intensity distribution, a $2 \ mm$ pinhole was used. The laser beam profiles at the input window of the ADM01 (Fig. 4.5a), at the focal point (Fig. 4.5b) and at the output window of the ADM (Fig. 4.5c) are following depicted.
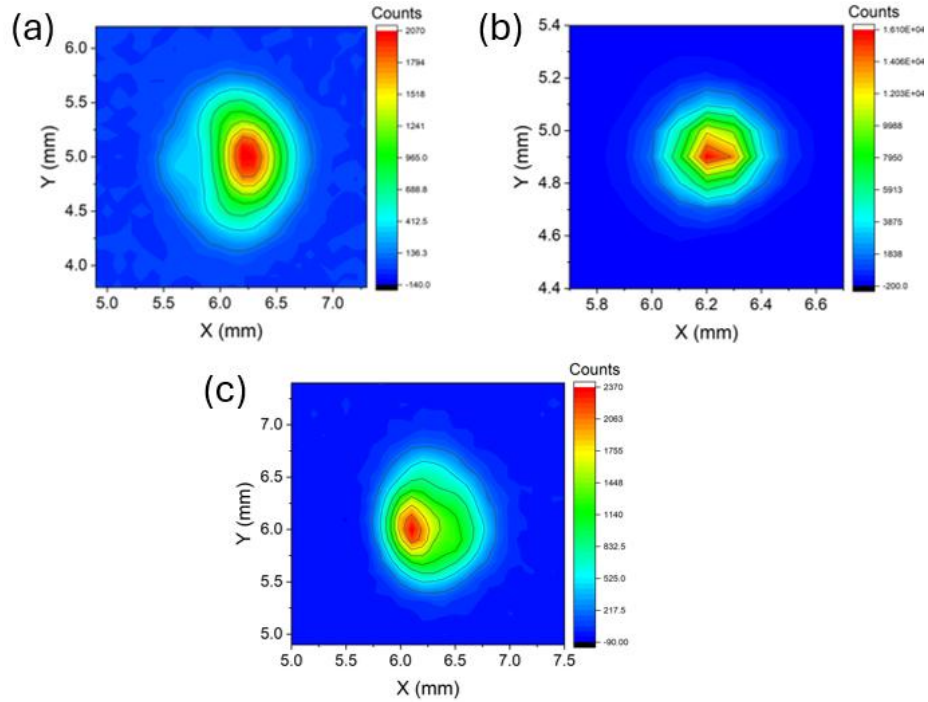

Fig. 4.5. (a) Beam profile at the input window of the ADM01; (b) Beam profile at the focal point; (c) Beam profile at the output window of the ADM01.

The pinhole effectively eliminates tails and yields a more symmetric intensity distribution. At the focal point, the beam size was measured to be 0.5×0.5 mm² in both the X and Y directions. Table 4.1 summarizes the QCL output optical powers at an injection current of $693\ mA$ measured at different points of the QEPAS setup (see Fig. 3.4), together with estimation of power losses in %-unit.

Tab. 4.1. QCL optical power at an injection current of 693 mA measured at different points of the QEPAS setup and an estimation of power losses in %-unit.

Component	Power (mW)	Losses (%)
Laser	3.7	-
Pinhole + Focal Lens	2.5	12% pinhole + 20% lens
ADM	1.4	20% ADM
Power meter after the ADM	1.33	-

The pinhole filtering results in a 12% reduction in QCL emitted power. Additionally, each of the two optical components — the ZnSe lens and the entrance windows of the ADM — further reduces the optical power by 20%. This significant loss is attributed to the optical components not being optimized for operation at $14.85\ \mu m$.

4.1.2 Spectrophone electrical characterization

The resonance frequency and the Q-factor of the fundamental in-plane flexural mode of the spectrophone included in the commercial ADM01 employed for QEPAS measurements, were measured by exploiting the inverse piezoelectric effect via an electrical polarization. The electrical characterization was carried out exciting the spectrophone with a sinusoidal electrical signal, using the Tektronix AFG 31000 waveform generator, and performing a frequency sweep with a step of $0.1\ Hz$, to reconstruct the resonance curve of the QTF nearby its resonance frequency. The generated piezoelectric current was converted into a voltage signal by the operational transimpedance amplifier integrated in the ADM01. The lock-in amplifier was used to demodulate the QTF output signal at the excitation frequency. The frequency response of the

QTF at atmospheric pressure as a function of the driving frequency of the waveform generator is shown in Fig. 4.6.
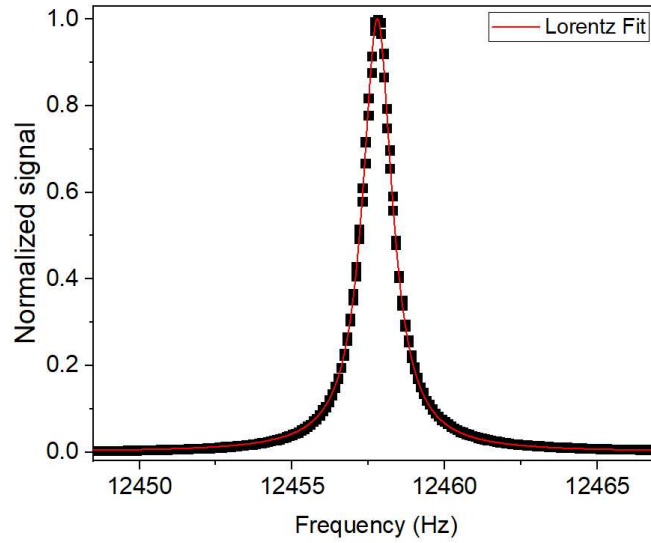

Fig. 4.6. Resonance curve of the employed QTF (black squares) and best Lorentz fitting (red solid line).

The Lorentz function was used to fit the resonance curve and obtain the QTF resonance frequency f_0 and the full width at half-maximum (FWHM) Δf of the signal response. In this way, the Q-factor was calculated as the ratio between f_0 and Δf. A resonance frequency of $12457.8\ Hz$ and a Q-factor of 10648 was obtained at atmospheric pressure. By varying the air pressure inside the ADM, the resonance curves were reconstructed following the same procedure. The extracted resonance frequencies and Q-factor values of the spectrophone as a function of air pressure are plotted in Fig. 4.7.
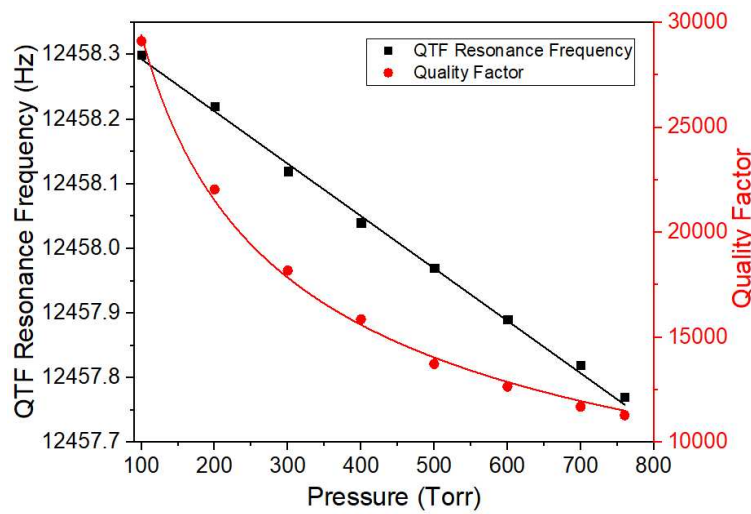

Fig. 4.7. Resonance frequency (black squares) and Q-factor (red circles) of the spectrophone, as a function of pressure.

As explained in section 2.1.2, the coupling of the QF with a pair of micro-resonator tubes causes a small shift of spectrophone resonance frequency which increases linearly with the gas pressure, as described in Eq. *(2.16)*. The dependence of the resonance frequency on the gas pressure can be determined by the assumption that the gas effect on prong vibrations damping increases the inertia of the prong. The added mass per unit length of a thin prong is proportional to gas density, which is in turn proportional to the gas pressure by means of ideal gas law (Blake, 1974). From the imposed linear fit, an intercept of $12458.4\ Hz$ was obtained and a slope of $8 \times 10^{-4}\ Hz/Torr$ was estimated.

The Q-factor represents a measure of the amount of energy retained in the resonator with respect to the energy dissipated in one cycle of oscillation. It rapidly decreases with increasing pressure (red squares in Fig. 4.7) due to energy losses by the viscous damping and friction losses caused by the interaction between the oscillating tines of the QTF and the surrounding medium (Patimisco et al., 2018). The dependence of the Q-factor on gas pressure follows the trend described in Section 2.1.4 by Eq. *(2.21)*. Fitting the obtained data with Eq. *(2.21)*, the estimated C and D parameters were $4 \times 10^{-6} \pm 1 \times 10^{-6}$ and $3 \times 10^{-6} \pm 7 \times 10^{-8}\ Torr^{-0.5}$, respectively. In the whole pressure range, the coupling of the QTF with the micro-resonator tubes leads to a reduction in the spectrophone Q-factor, with respect to a bare QTF. This behaviour can be explained by considering that the effect of acoustic coupling of the high Q-factor QTF with the low Q-factor tubes, leads to a QTF loss of energy.

4.1.3 Modulation depth and gas pressure optimization

In QEPAS measurements, the optimization of modulation depth and gas pressure is a fundamental step to enhance the sensitivity of the QEPAS sensor. In case of broadband absorption features with the presence of interferents, the experimental determination of the best operating conditions aims at achieving the right trade-off to maximize the QEPAS signal and preserve the spectral selectivity of the absorption feature of the target molecule, for an accurate reconstruction of the absorption profile (Kinjalk et al., 2024).

The modulation depth describes the QCL's wavelength variation around its mean value because of the sinusoidal modulation. It influences the detection sensitivity of the QEPAS sensor, as well as the shape of the reconstructed profile of the absorption feature. Although an overmodulation can increase the QEPAS signal intensity, it is crucial to preserve the derivative shape of the absorption profile and prevent the excitation of nearby absorption interferents. To identify the optimal modulation depth, the QCL's emission wavelength was locked at the

benzene absorption peak, fixing the laser injected current at $692\ mA$, and the amplitude of the sinusoidal modulation was varied from $50\ mVpp$ ($0.16\ cm^{-1}$) up to $240\ mVpp$ ($0.75\ cm^{-1}$). This maximum value was set to prevent damages to the QCL. The pressure range of investigation was set from $50\ Torr$ to $760\ Torr$. Pressures lower than $50\ Torr$ were not considered because the QEPAS signal was too low in the overall investigated range of modulation depth. The 2f-QEPAS peak signal as a function of modulation depth for a mixture of $100\ ppm$ of benzene in N_2 is reported in Fig. 4.8, for different operating pressures.
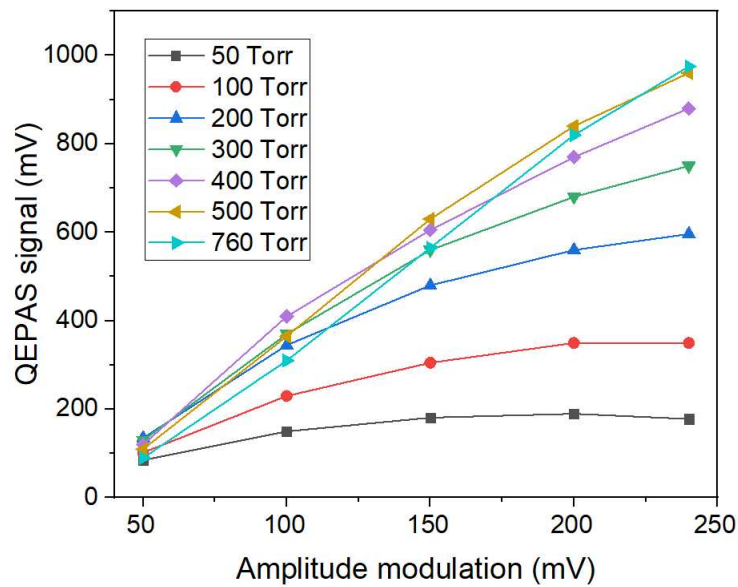

Fig. 4.8. QEPAS peak signal as a function of modulation depth at different pressures for a mixture of $100\ ppm$ of benzene in N_2.

Increasing the modulation depth from $50\ mVpp$ to $240\ mVpp$, the QEPAS peak signal increases as well. The optimal modulation depth maximizing the 2f-QEPAS signal was $240\ mVpp$.

The dependence of the QEPAS peak signal on the operating pressure is the result of a trade-off between two trends (Giglio et al., 2019): i) the Q-factor deterioration of the spectrophone as the working pressure increases; ii) the faster transfer of photoexcited molecules energy via nonradiative relaxation processes at higher pressures (because each molecule can count on more nearest neighbours), resulting in a more efficient generation of the sound wave. Considering a mixture of $100\ ppm$ of C_6H_6 in N_2, the QEPAS signal as a function of the operating pressure was investigated. The 2f-QEPAS spectral scans and the extracted peak values as a function of gas pressure are reported in Fig. 4.9a and 4.9b, respectively.
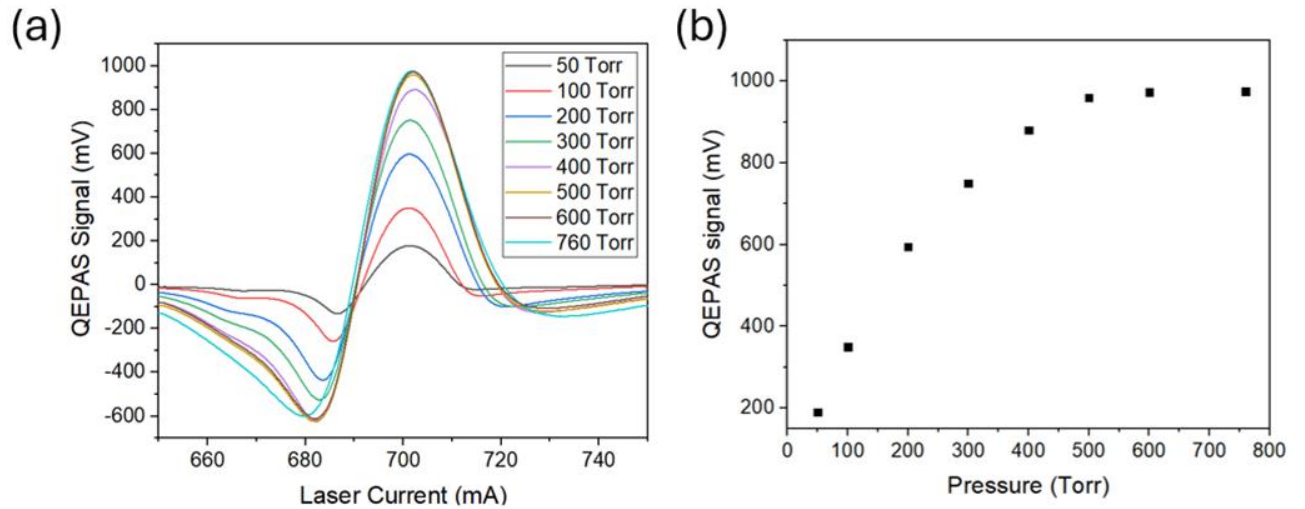
Fig. 4.9. (a) 2f-QEPAS spectral scans as a function of operating pressure; (b) QEPAS peak signal as a function of operating pressure.

Within the investigated pressure range, the absorption feature profiles exhibit slight distortion with increasing pressure. Therefore, $500\ Torr$ was chosen as the optimal pressure, being the lowest value that maximizes the QEPAS peak signal (see Fig. 4.9b).

4.1.4 Sensor calibration

To determine the sensitivity of the developed QEPAS sensor, a calibration process was conducted by acquiring spectral scans at different benzene concentrations obtained by diluting the certified gas cylinder of $240\ ppm$ of benzene in N$_2$, with pure humidified N$_2$, using the MCQ gas blender. The gas flow rate was set to $25\ sccm$. The measurements were acquired imposing the working conditions reported in Section 4.1.2 and 4.1.3: i) sinusoidal modulation centered at $6228.9\ Hz$, which is half of the resonance frequency of the QTF (wavelength modulation and 2f-detection); ii) operating pressure set to $500\ Torr$; iii) modulation depth of $240\ mVpp$. Moreover, a ramp was imposed to the current driver together with the sinusoidal modulation (see Fig. 3.4) to scan across the benzene absorption feature, with the following parameters: frequency $f_{ramp} = 10\ mHz$ and amplitude $A = 300\ mV$. These settings allows a current scan from $600\ mA\ to\ 750\ mA$, within the overall current dynamic range of the QCL (Paciolla et al., 2022). The lock-in time constant was set to $100\ ms$ and an appropriate choice of the lock-in detection phase was needed to correctly reconstruct the 2f-QEPAS feature.

The 2f-QEPAS spectral scans at six different concentrations ($5\ ppm, 10\ ppm, 25\ ppm, 50\ ppm, 75\ ppm\ and\ 100\ ppm$) are reported in Fig. 4.10a. The peak values of the QEPAS signal were extracted from each spectral scan and plotted as a function of the corresponding benzene concentration (datapoints), together with the best linear fit of the experimental (red solid line), as depicted in Fig. 4.10b.
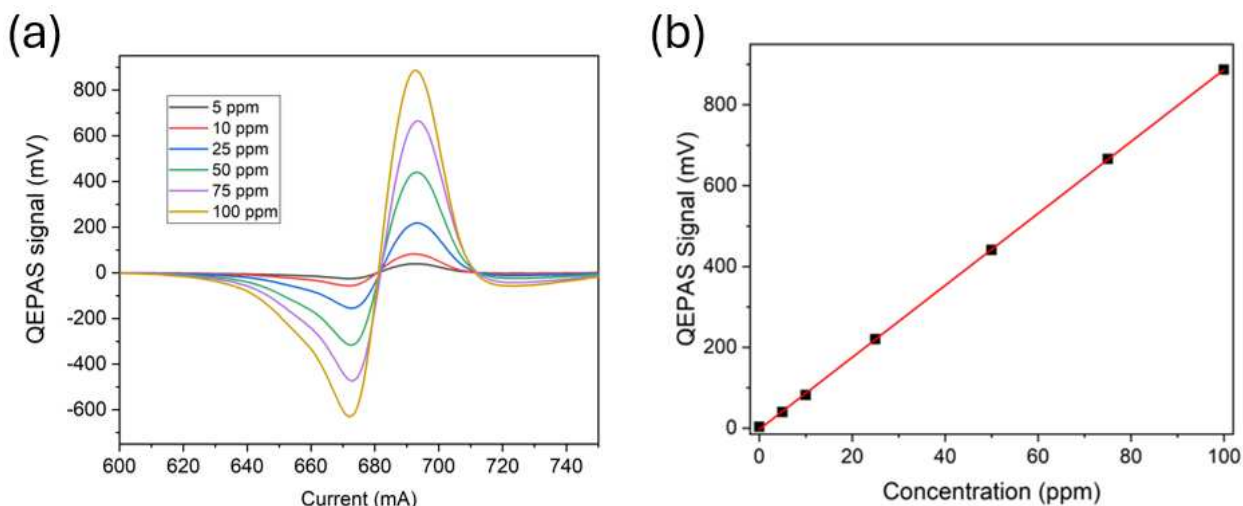

Fig. 4.10. (a) 2f-QEPAS spectral scans at different benzene concentrations; (b) QEPAS signal peak value extracted from each spectral scan as a function of the corresponding benzene concentration (datapoints), together with the best linear interpolation (solid red line).

The acquired 2f-QEPAS spectral scans show a background-free, second-harmonic derivative line-shape, with a significant distortion of the asymmetry of the two negative lobes, as the effect of the Residual Amplitude Modulation (RAM). The RAM contribution originates from the strong intensity modulation of the QCL determined by the imposed sinusoidal modulation (Ruxton et al., 2010).

The developed QEPAS sensor response shows an excellent linearity ($R^2 = 0.99992$) with the benzene concentration (Fig. 4.10b) with a slope of $8.9\ mV/ppm$, corresponding to the sensitivity of the QEPAS sensor for benzene detection.

The noise level is calculated as the standard deviation (1σ) of the sensor response when there is no optical absorption, namely by flowing pure N$_2$ through the ADM01, and locking the QCL current at the absorption peak of the benzene. The time-series of the acquired QEPAS signal at $-5\ °C$ and $760\ Torr$ before flushing benzene is shown in Fig. 4.11.
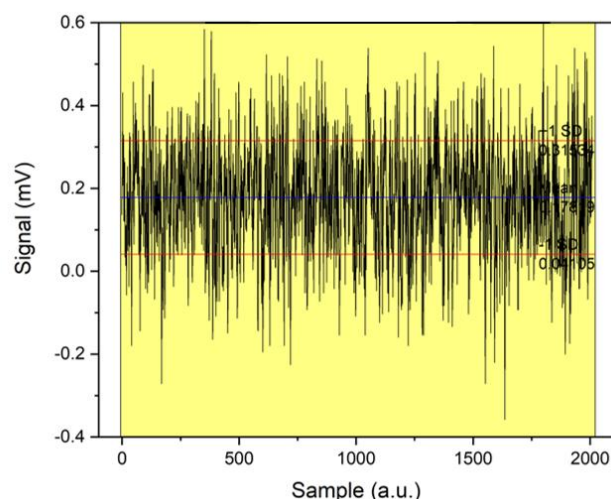
Fig. 4.11. Time-series of the acquired QEPAS signal at $-5\ °C$ and $760\ Torr$ without optimized parameters before flushing benzene.

The 1σ-value of the acquired dataset is $0.117\ mV$, corresponding to the noise level of the QEPAS sensor for benzene detection. The minimum detection limit (MDL) is usually expressed in terms of noise equivalent concentration (NEC) and it is defined as the concentration of the gas to be detected whose signal equals the noise level, namely corresponding to the condition SNR = 1 (De Palo et al., 2023). It represents the smallest concentration of gas that can be distinguished from the background noise. Considering a QEPAS peak signal of $890\ mV$ obtained with a mixture of $100\ ppm$ of C_6H_6 in N_2 and the noise level, the SNR is 7607, corresponding to a MDL of $13\ ppb$ for benzene detection with a lock-in time constant of $100\ ms$. All these estimated parameters are listed in Table 4.2.

Tab. 4.2. Most important obtained parameters of the developed QEPAS based sensor for benzene detection.

QEPAS peak signal measured with 100 ppm of C₆H₆	890 mV
Noise	0.117 mV
Signal to Noise Ratio (SNR)	7607
Minimum Detection Limit (MDL)	13 ppb

The potential spectral interferences caused by other two BTEX, namely ethylbenzene and toluene, on benzene detection were investigated. This analysis aims at verifying whether the presence of the other two compounds in the mixture affects the radiation-to-sound conversion efficiency ε at a given pressure (Kinjalk et al., 2024). Figure 4.12 compares the 2f-QEPAS signal obtained for a mixture of $10\ ppm$ of C_6H_6 in N_2 with a gas mixture containing $10\ ppm$ of benzene, $68\ ppm$ of toluene, $20\ ppm$ of ethylbenzene and N_2 as rest.
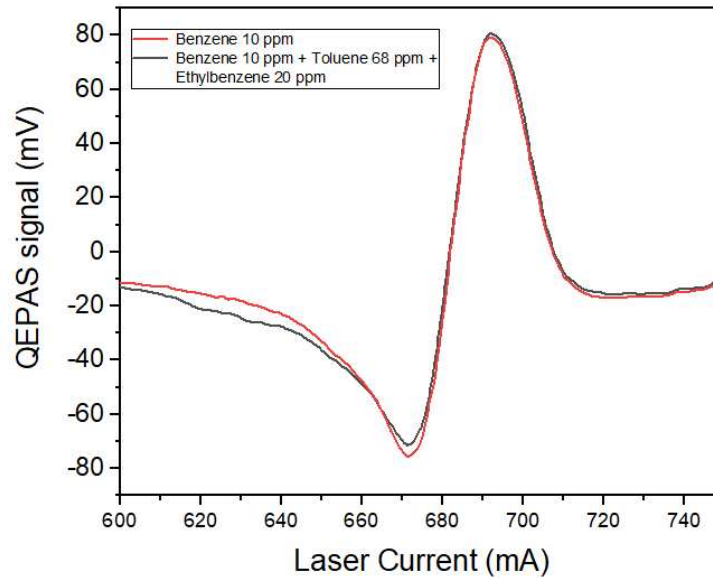

Fig. 4.12. Comparison between the QEPAS signals of $10\ ppm$ of benzene in N_2 (red line) and a mixture of $10\ ppm$ of benzene, $68\ ppm$ of toluene, and $20\ ppm$ of ethylbenzene in N_2 (black line).

Nearby the benzene peak value at $692\ mA$, the two spectral scans completely overlap, indicating that the presence of toluene and ethylbenzene in a mixture does not affect the benzene signal acquisition.

4.1.5 Long terms stability analysis

From a theoretical point of view, the signal from a perfectly stable system could be infinitely averaged, thus leading to extremely sensitive measurements. However, an optical sensor operating in the field is a limited stable system. By increasing the integration time, it is possible to enhance the sensitivity and thus improve the detection limit of a QEPAS sensor. There exists an optimum integration time at which the detection limit reaches a minimum value, then at longer averaging time long-term effects, such as laser and mechanical instabilities, as well as slow temperature drifts emerge, and the sensor performance deteriorates. The optimal integration time for a given sensor could also depend on the specific application. The Allan-

Werle variance analysis is mandatory to determine long-term stability of a sensor and allows investigating drifts and establishing the sensor signal averaging limits. This technique was developed by Allan in 1966 to study frequency stability of precision oscillators (Allan, 1966). In 1993, Werle applied the Allan variance to signal averaging in tunable laser absorption spectroscopy (TDLAS) instrumentation (Werle et al., 1993). Given a set of M time-series data acquired with an integration time τ, its Allan-Werle variance $\sigma_y^2(\tau)$ is defined as:

$$\sigma_y^2(\tau) = \frac{1}{M}\sum_{k=1}^{M}\frac{1}{2}(y_{k+1} - y_k)^2 \tag{4.1}$$

where y_k is the kth data averaged over an integration time τ, $y_{k+1} - y_k$ is the difference between adjacent values of y_k, and M is the total number of data, usually of the order of $10^3 - 10^4$. To estimate how $\sigma_y^2(\tau)$ changes with the integration time, a LabView-based code was implemented. Starting from the set of M data acquired at an integration time τ_0 and assuming that there is no dead time between adjacent measurements, the software averages the values for y_1 and y_2 and obtains a new y_1 value averaged over $2\tau_0$. Subsequently, this routine averages values for y_3 and y_4 and changes them as a new value y_2 averaged over $2\tau_0$ and applies Eq. *(4.1)* to determine $\sigma_y^2(2\tau_0)$. The software iterates the process for other integer multiples m of τ_0 and generates the values of $\sigma_y^2(m\tau_0)$.

To estimate the achievable MDL as a function of the lock-in integration time, an Allan–Werle deviation analysis was performed by acquiring the QEPAS signal for 2.5 h with the same experimental conditions as for the measurement of the noise level (refer to Section 4.1.4). The Allan–Werle plot, in terms of MDL as a function of lock-in integration time, is shown in Fig. 4.13.
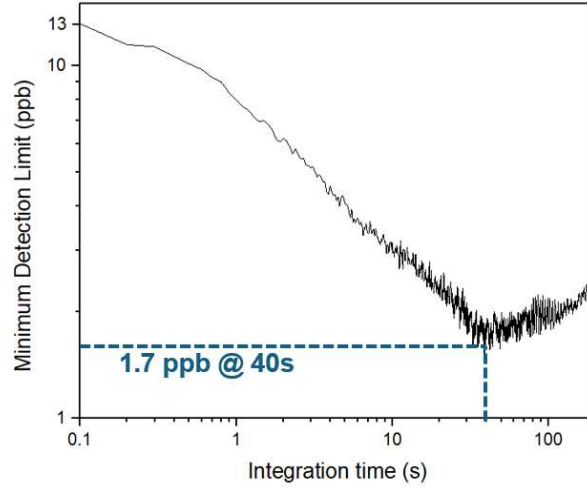
Fig. 4.13. Allan–Werle plot of the developed QEPAS sensor reporting the minimum detection limit as a function of lock-in integration time.

The Allan deviation analysis demonstrates that for integration times $< 40\ s$, the noise level closely follows a $1/\sqrt{t}$ dependence, highlighting that the thermal noise of the QTF is the dominant source of noise in QEPAS measurements. The Allan-Werle plot follows this trend till a turnover point, corresponding to an optimum integration time $\tau_{opt} = 40\ s$. For longer integration times the noise level increases, and the ultimate performance of the sensor deteriorates. At τ_{opt}, the MDL reaches its lowest value of $1.7\ ppb$ (marked in Fig. 4.13). For $\tau > \tau_{opt}$ the QEPAS sensor sensitivity starts to deteriorate, due to the occurrence of long-terms effects that dominate the QTF noise signal (Giglio et al., 2016).

4.2 LITES sensor for benzene detection

As described in Section 3.3, in the LITES setup the QCL beam passes through the $12\ cm$ long-brass gas cell. The cell is positioned $6\ cm$ far from the laser output window and it is featured with two optical windows made of germanium. The laser power measured after the exit window of the gas cell was $2.2\ mW$. Then, the laser beam is focused onto the QTF's surface through a ZnSe plano-convex lens positioned $2.5\ cm$ far from the QTF. The optical power measured after the lens was $\sim 1.8\ mW$.

The QCL beam profiles acquired with the infrared pyrocam at the exit window of the gas cell and at the focal plane of the lens are depicted in Fig. 4.14a ad 4.14b, respectively.
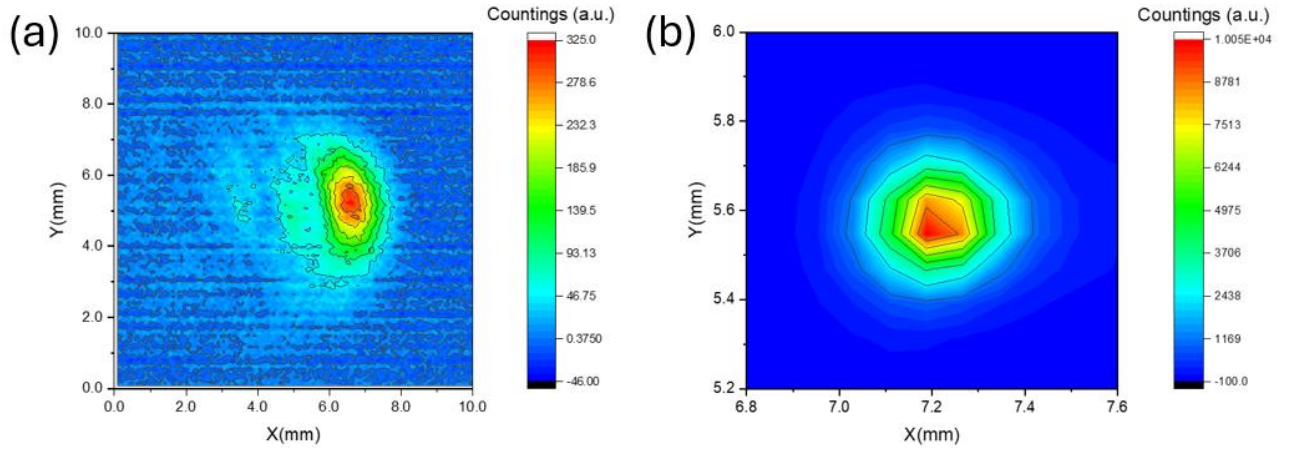

Fig. 4.14. (a) Beam profile at the exit window of the gas cell; (b) Beam profile at the focal plane.

At the focal plane of the lens (Fig. 4.14b), the beam dimension was about $0.5 \times 0.5\ mm^2$ in both the X and Y directions.

4.2.1 Custom QTF electrical characterization

As discussed in Section 3.3.2, a bare QTF is used as infrared photodetector in the LITES setup. The resonance curve of the QTF was acquired by following the same procedure described in Section 4.1.2. for the QEPAS spectrophone. The result is shown in Fig. 4.15.
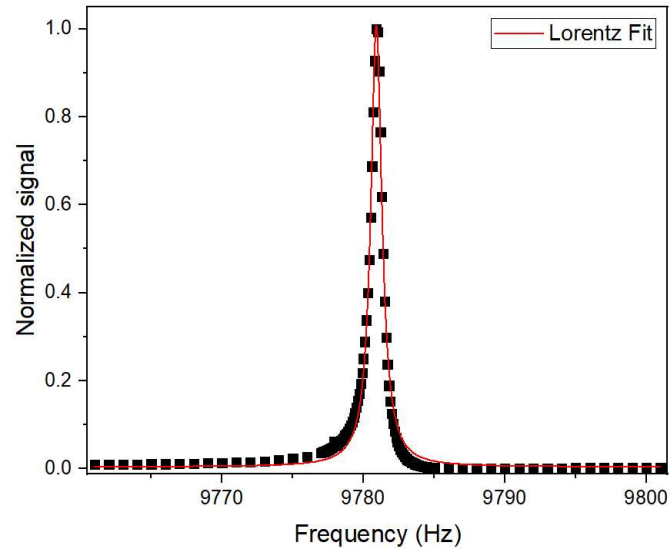

Fig. 4.15. Resonance curve of the employed QTF (black squares) and best Lorentz fitting (red solid line).

A Lorentzian fit was superimposed to the collected data to evaluate both the resonance frequency and the Q-factor of the bare QTF at atmospheric pressure, resulting in 9780.9 Hz and 10340, respectively.

4.2.2 Modulation depth and gas pressure optimization

As for the QEPAS sensor, the modulation depth and the gas pressure within the cell must be optimized to maximize the LITES signal. The 2f-LITES spectral scans at different modulation depth ranging from $200\ mVpp\ to\ 700\ mVpp$ are shown in Fig. 4.16a, when a certified concentration of $240\ ppm$ of benzene in N_2 flows in the ADM at $700\ Torr$.
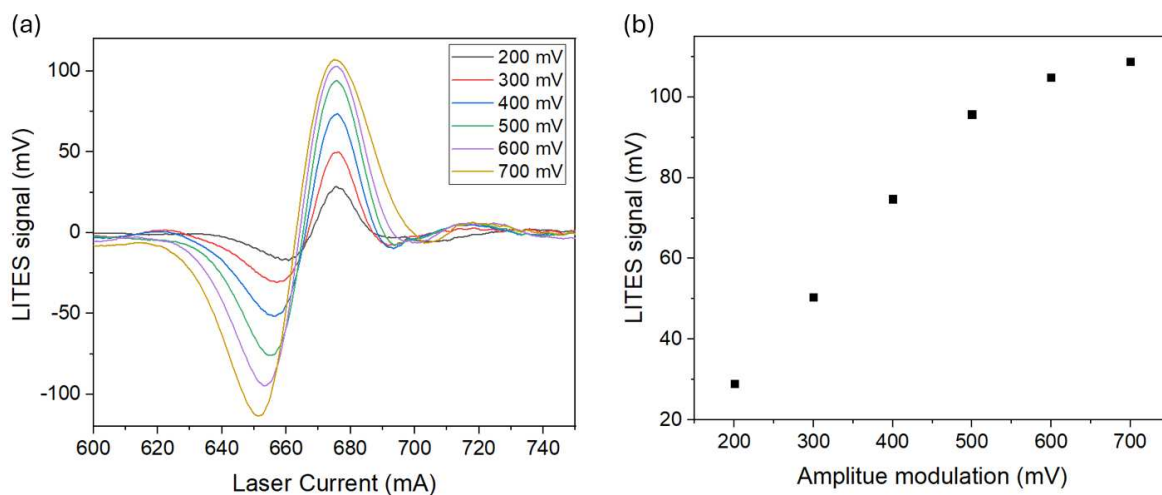

Fig. 4.16. (a) 2f-LITES spectral scans at different modulation depth; (b) LITES peak signals as a function of modulation depth.

For each spectral scan, the peak values were extracted and plotted as a function of modulation depth, as shown in Fig. 4.16b. An optimum value for the modulation depth of $600\ mVpp$ was set to avoid an excessive broadening of the spectral scan of the absorption feature.

Considering the same benzene concentration in N_2, the operating pressure was optimized in the range $200 - 700\ Torr$. The acquired 2f-LITES spectral scans at different pressures are reported in Fig. 4.17a.
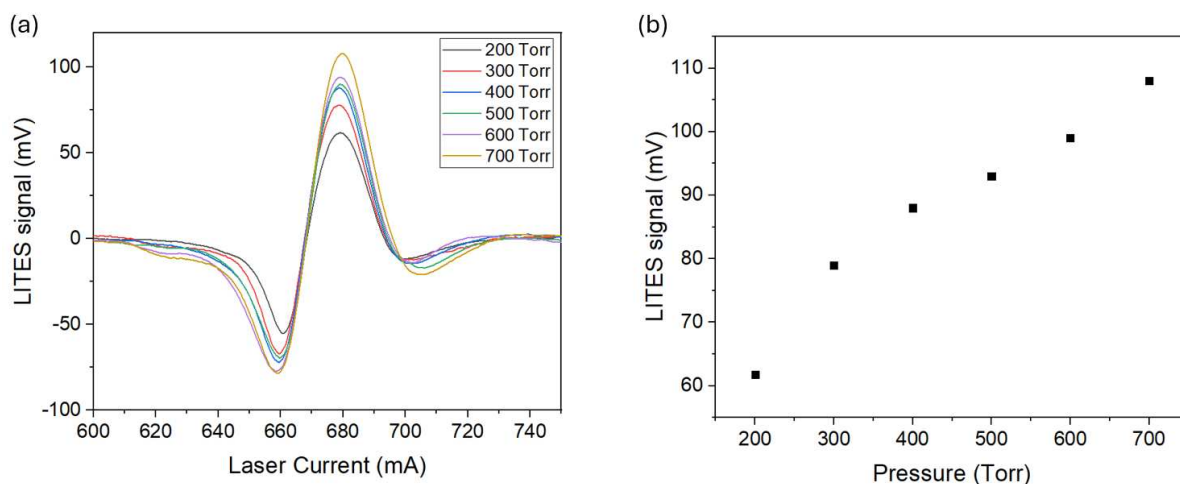

Fig. 4.17. (a) 2f-LITES spectral scans at different operating pressures; (b) LITES peak signals as a function of operating pressures.

As already discussed for the QEPAS signal in Section 4.1.4, the reconstruction of the benzene absorption feature shows a strong asymmetry in the negative lobes. This effect is due to the RAM contribution, occurring because of the high modulation depth employed to optimize the LITES signal. In Fig. 4.17b, the peak values of the spectral scans are plotted as a function of the gas pressure. The optimal pressure value for the LITES sensor was set to 700 Torr.

4.2.3 Sensor calibration

The LITES sensor was calibrated at a gas flow rate of $50\ sccm$, starting from a certified gas cylinder of $240\ ppm$ of C_6H_6 in N_2 and diluting it with pure N_2 to generate mixtures with different benzene concentrations. The working parameters for the LITES sensor calibration were: i) sinusoidal modulation at $4890.45\ Hz$, which is half of the resonance frequency of the QTF (wavelength modulation and 2f-detection); ii) operating pressure of $700\ Torr$; iii) modulation depth of $600\ mVpp$. Moreover, a ramp was imposed to the current driver together with the sinusoidal modulation to scan across the benzene absorption feature (see Fig. 3.13), with the following parameters: frequency $f_{ramp} = 5\ mHz$ and amplitude $A = 800\ mV$. These settings allow a current scan from $600\ mA\ to\ 750\ mA$, within the overall current dynamic range of the QCL. The lock-in time constant was set to $100\ ms$ and an appropriate choice of the lock-in detection phase is needed to correctly reconstruct the 2f-LITES signal.

The 2f-LITES spectral scans measured at five different benzene concentrations, namely $48\ ppm, 96\ ppm, 144\ ppm, 192\ ppm\ and\ 240\ ppm$ are reported in Fig. 4.18a. A non-flat background was observed also when pure N_2 was flushed inside the gas cell due to the high modulation depth required to enhance the signal (black line in Fig. 4. 18a). This background was monitored throughout the experiment and found to be stable and repeatable, allowing it to be considered as an offset. After subtracting this background, the resulting spectral scans are displayed in Fig. 4.18b. To retrieve the sensor calibration curve, the LITES peak values were extracted, plotted and linearly fitted with the best linear fit, as shown in Fig 4.18c.
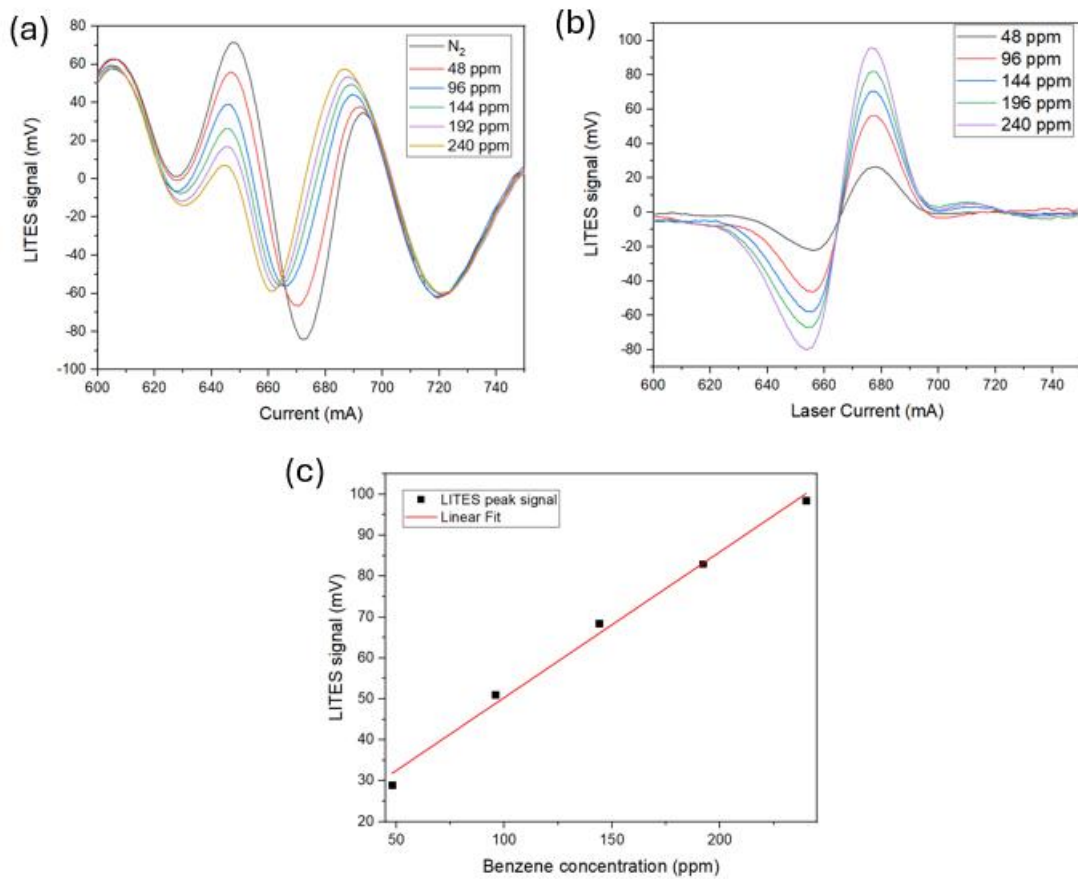
Fig. 4.18. (a) 2f-LITES spectral scans measured at five different benzene concentrations, namely 48 ppm, 96 ppm, 144 ppm, 192 ppm and 240 ppm and non-flat background measured when pure N₂ was flushed inside the gas cell (black line); (b) Resulting spectral scans after subtracting the background; (c) LITES signal peak value extracted from each spectral scan as a function of the corresponding benzene concentration (datapoints), together with the best linear interpolation (solid red line).

The LITES sensor for benzene detection shows an excellent linear response in the investigated concentration range. The sensitivity of the LITES sensor for benzene detection was equal to $0.4 \ mV/ppm$, with $R^2 = 0.9992$. Considering a LITES peak signal of $96 \ mV$ for a benzene concentration of $240 \ ppm$ in N₂ and a noise level of $42 \ \mu V$, the SNR results 2286. The estimated MDL for lock-in time constant of $100 \ ms$ is $105 \ ppb$. These parameters extracted from the LITES sensor calibration are summarized in Table 4.3.

Tab. 4.3. Most important obtained results for the LITES based sensor for benzene detection.

LITES signal at 240 ppm	96 mV
Noise	42 μV
Signal to Noise Ratio (SNR)	2286
Minimum Detection Limit (MDL)	105 ppb

The developed QEPAS and LITES sensors achieved a high sensitivity for benzene detection and showed an excellent linearity in the investigated concentration range. The QEPAS sensor response shows an excellent linearity ($R^2 = 0.99992$) with the benzene concentration with a sensitivity of 8.9 mV/ppm. The sensitivity of the LITES sensor for benzene detection was equal to $0.4 \, mV/ppm$, with $R^2 = 0.9992$. An estimated MDL of $13 \, ppb$ and $105 \, ppb$ for the QEPAS and LITES sensors, respectively, were obtained with a lock-in time constant of $100 \, ms$.

4.2.4 Long terms stability analysis

The long-term stability of the developed LITES-based sensor was investigated with an Allan–Werle analysis, under the same experimental conditions used for the QEPAS sensor in Section 4.1.5. Fig. 4.19 reports the Allan–Werle plot in terms of the MDL as a function of the integration time.
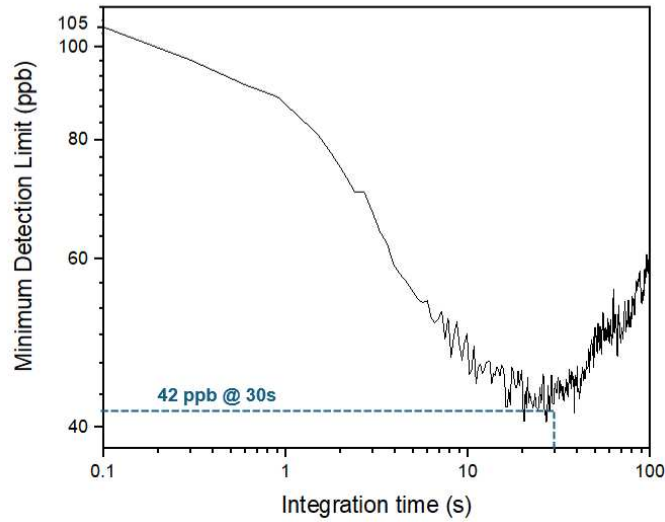

Fig. 4.19. Allan–Werle plot of the developed LITES sensor reporting the minimum detection limit as a function of lock-in integration time.

Considering an integration time of $30\,s$ at the turnover point, the MDL can be lowered to $42\,ppb$.

4.2.5 Technological challenges related to LITES technique

The LITES technique for long wavelengths presents several technological challenges. The first is related to the use of optical components without the appropriate antireflection coating because not commercially available. The germanium windows of the gas cell have the antireflection coating is in the range $3 - 12\,\mu m$, while the ZnSe focal lens in the range $7 - 12\,\mu m$. Being outside the antireflection window, the transmittance spectrum of germanium at wavelengths higher than $13\,\mu m$ (refer to Fig. 3.15) presents fringes that negatively influence the detected LITES signal and create a strong non-flat background. To mitigate this undesirable effect, the two germanium windows of the cell were replaced with uncoated Polymethyl Pentene (TPX) windows (Zifarelli et al., 2024). The low transmittance of TPX windows negatively affects the effective optical power at the gas cell exit window. The LITES spectral

scans obtained using the gas cell with the TPX windows, with a gas mixture of 240 *ppm* C_6H_6 in N_2, as well as the scans acquired in pure N_2 at different operating pressures, are reported in Fig. 4.20.
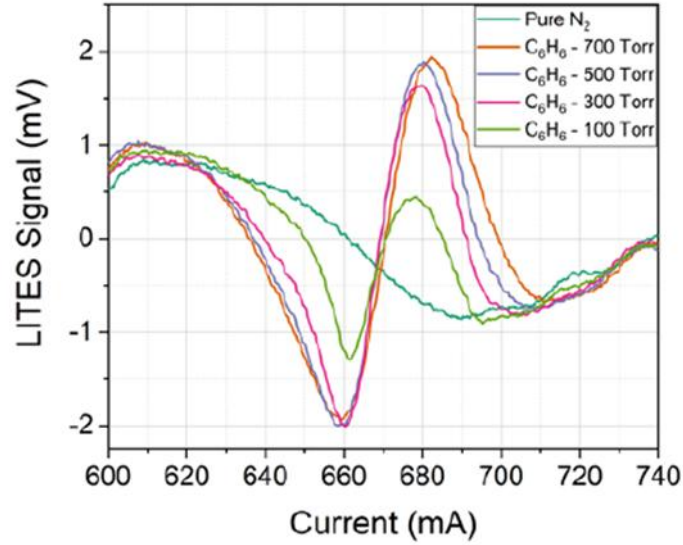

Fig. 4.20. LITES spectral scans obtained using two TPX windows at different operating pressure, targeting a concentration of 240 *ppm* C_6H_6 in N_2 and background measured in pure N_2 (Zifarelli et al., 2024).

Another important aspect to consider in LITES measurements is the spatial quality of the laser beam. When using a single focusing lens, a beam with poor spatial quality can negatively impact the size of the beam spot at the focal plane. For a given optical power, a larger beam spot on the QTF surface results in broader local heating accumulation (Ma et al., 2020). Consequently, the strain field is not efficiently excited.

4.3 Integration of a QEPAS sensor on a mobile rover

Nowadays, off-road mobile robots are widely employed in various applications, including disaster management activities, military operations and agriculture. A possible future development is the integration of a compact QEPAS sensor on an agricultural mobile rover to perform real-time monitoring activities in an agricultural field, to detect the presence of harmful gases. At the beginning of 2024, the company Thorlabs GmbH has commercialized the first "All-in a box" QEPAS sensor, a compact and complete system for methane detection (Zifarelli et al., 2022). The box architecture is ready to use and implements a stainless-steel box where optical components are fixed to keep the system aligned, improving the robustness to misalignment, and reducing its overall dimensions. Internal pressure and flow controllers direct the target gas to the commercial ADM01. The QEPAS box is equipped with all the electronic components inside the sensor box, including laser, laser controller and a DAQ-card for data collection and processing. The front panel of the box has two gas connection ports and simply connecting a small volume of target gas to the inlet port of the sensor, it can perform real-time measurements.

A custom agricultural mobile rover should be realized to carry the QEPAS box sensor in the field. Some features of this robot might be based on the MEGA MAXXII unmanned ground vehicle (UGV) (Ugenti et al., 2023). It is an all-terrain skid-steering electric tracked terrestrial rover, specially designed for agricultural applications. The tracks are energetic efficient and ensure good mobility in unstructured environments, having a large contact area with the ground (Devanna et al., 2022). The peculiarity of this rover lies in the presence of an articulated passive suspension system for each side track, that allows the ground wheels to move independently with respect to the vehicle body, ensuring high mobility (Galati et al., 2023). The rover is powered by an Absorbent Glass Mat (AGM) battery pack up to 1.5 kW of output power and is driven by two 24 VDC brushed motors with maximum torque of 80 Nm. The maximum reachable speed is 1 m/s and the robot's autonomy is about 4 h. The rover's CAD rendering with the main dimensions is shown in Fig. 4.21.
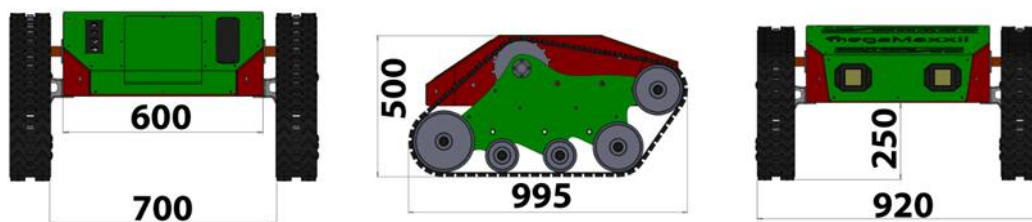

Fig. 4.21. Rover's CAD rendering with the main dimensions in mm.

The rover dimensions are: $955 \times 920 \times 500\ mm\ (L \times W \times H)$ and its mass is $\sim 110\ kg$. The rover comprises a central body and two side tracks. On each side, a rubber track is wrapped around the drive sprocket, the idler wheel, and the four ground wheels. The use of tracks ensures a ground pressure of $7\ kPa$ at maximum payload ($\sim 100\ kg$). Thanks to this design, body vibrations induced by the terrain irregularity are significantly reduced by $\sim 50\%$ with respect to a standard tracked robot (Galati et al., 2023). An embedded industrial computer with Ubuntu operating system installed, wireless connectivity and Bluetooth interfaces is mounted on the rover. The Robot Operating System (ROS) is run on the computer to generate locomotion commands over a RS232 serial port directly connected to the motor controllers. The rover will be able to autonomously navigate in an agricultural field, thanks to an ad hoc designed navigation system, according to pre-established routes (Paciolla et al., 2023). The upper surface of the rover can be used to place several sensors, such as a Light Detection and Ranging (LiDAR) sensor, an Inertial measurement unit (IMU), and different cameras that can be mounted at different heights and positions. The LiDAR sensor is useful for obstacle detection, the 9 Dof IMU is useful to retrieve the robot localization in the 3D space (position and orientation) and the cameras can be used for the perception of the surrounding environment. The accurate geo-localization system for the precise rover's localization is obtained from a dual GPS configuration that works in conjunction with an IMU. Moreover, the rover will be equipped also with active sensors for the evaluation of the main indicators of soil characteristics (pH, humidity, texture, nutrients, temperature, electrical conductivity, radionuclides) to determine vegetative indices.

Bibliography

Allan, D. W. (1966). Statistics of atomic frequency standards, Proc. IEEE, 54(2), 221–230.

Bazhenov, N.L., Mynbaev, K.D., Ivanov-Omskii, V.I. (2005). Temperature dependence of the threshold current of QW lasers. Semiconductors 39, 1210–1214 (2005). current of QW lasers. Semiconductors 39, 1210–1214.

Behringer, M. (2007). High-power diode laser technology and characteristics. In High Power Diode Lasers: Technology and Applications, 5-74. New York, NY: Springer New York.

Blake, W.K. (1974). The radiation from free-free beams in air and in water, J. Sound Vib., 33, 427–450.

De Palo, R., Elefante, A., Biagi, G., Paciolla, F., Weih, R., Villada, V., ... & Patimisco, P. (2023). Quartz-enhanced photoacoustic sensors for detection of eight air pollutants. Advanced Photonics Research, 4(6), 2200353.

Devanna, R. P., Milella, A., Marani, R., Garofalo, S. P., Vivaldi, G. A., Pascuzzi, S., ... & Reina, G. (2022). In-field automatic identification of pomegranates using a farmer robot. Sensors, 22(15), 5821.

Giglio, M., Patimisco, P., Sampaolo, A., Scamarcio, G., Tittel, F. K. & Spagnolo, V. (2016). Allan Deviation Plot as a Tool for Quartz-Enhanced Photoacoustic Sensors Noise Analysis, 63, 4 555.

Giglio, M., Menduni, G., Patimisco, P., Sampaolo, A., Elefante, A., Passaro, V. M., & Spagnolo, V. (2019). Damping mechanisms of piezoelectric quartz tuning forks employed in photoacoustic spectroscopy for trace gas sensing. physica status solidi (a), 216(3), 1800552.

Kinjalk, K., Paciolla, F., Sun, B., Zifarelli, A., Menduni, G., Giglio, M., ... & Spagnolo, V. (2024). Highly selective and sensitive detection of volatile organic compounds using long wavelength InAs-based quantum cascade lasers through quartz-enhanced photoacoustic spectroscopy. Applied Physics Reviews, 11(2).

Ma, Y., He, Y., Patimisco, P., Sampaolo, A., Qiao, S., Yu, X., ... & Spagnolo, V. (2020). Ultra-high sensitive trace gas detection based on light-induced thermoelastic spectroscopy and a custom quartz tuning fork. Applied Physics Letters, 116(1).

Paciolla, F., Pace, N., Barile, G., Patimisco, P., Valenza, F., & Pascuzzi, S. (2023). Autonomous navigation simulation of an agricultural robot during soil fertilization in open fields. In 2023 IEEE International Workshop on Metrology for Agriculture and Forestry (MetroAgriFor), pp. 640-645. IEEE.

Paciolla, F., Zifarelli, A., Spagnolo, V., Patimisco, P., Sampaolo, A., Giglio, M., ... & Baranov, A. N. (2022). Benzene and Toluene Detection with a Quartz-Enhanced Photoacoustic Sensor. In 2022 IEEE International Symposium on Medical Measurements and Applications (MeMeA), pp. 1-2. IEEE.

Patimisco, P., Sampaolo, A., Mackowiak, V., Rossmadl, H., Cable, A., Tittel, F. K., & Spagnolo, V. (2018). Loss mechanisms determining the quality factors in quartz tuning forks vibrating at the fundamental and first overtone modes. IEEE transactions on ultrasonics, ferroelectrics, and frequency control, 65(10), 1951-1957.

Ruxton, K., Chakraborty, A.L., Johnstone, W., Lengden, M., Stewart, G. & Duffin, K. (2010). Tunable diode laser spectroscopy with wavelength modulation: Elimination of residual amplitude modulation in a phasor decomposition approach, Sensors Actuators B Chem. 150, 367–375.

Ugenti, A., Galati, R., Mantriota, G., & Reina, G. (2023). Analysis of an all-terrain tracked robot with innovative suspension system. Mechanism and Machine Theory, 182, 105237.

Werle, P., Miicke, R. & Slemr, F. (1993). The limits of signal averaging in atmospheric trace-gas monitoring by tunable diode-laser absorption spectroscopy (TDLAS), Appl. Phys. B, 57 131–139.

Zifarelli, A., Mongelli, L. A., Paciolla, F., Kinjalk, K., Spagnolo, V., & Patimisco, P. (2024). Benzene detection using long wavelength QCL through LITES optical sensor. In Optical Sensing and Detection VIII (Vol. 12999, pp. 76-83). SPIE.

Zifarelli, A., Menduni, G., Giglio, M., Elefante, A., Sukhinets, A., Sampaolo, A., ... & Spagnolo, V. (2022). Compact and versatile QEPAS-based sensor box for simultaneous detection of methane and infrared absorber gas molecules in ambient air. Frontiers in Environmental Chemistry, 3, 926233.

Conclusions and future perspectives

The research activity carried out during my Ph.D. in Industry 4.0 was focused on the development of optical sensors for benzene detection targeting the absorption band centred at $14.85\ \mu m$ using an innovative, non-commercial QCL source. The developed sensing platforms were based on QEPAS and LITES techniques.

The developed QEPAS sensor employed as sensing element a spectrophone with resonance frequency and Q-factor of $12457.8\ Hz$ and 10648 at atmospheric pressure, respectively. The optimal operating parameters experimentally found were a modulation depth of $240\ mVpp$ and an operating pressure of $500\ Torr$. The developed QEPAS sensor response showed an excellent linearity ($R^2 = 0.99992$) in the investigated benzene concentration range, with a sensitivity of $8.9\ mV/ppm$. Considering a QEPAS peak signal of $890\ mV$, measured for a concentration of $100\ ppm$ of C_6H_6 in N_2 and a noise signal (1σ) of $0.117\ mV$, the obtained SNR was equal to 7607, corresponding to an estimated MDL of $13\ ppb$ for benzene detection with a lock-in time constant of $100\ ms$. At $40\ s$ of integration time, the MDL reaches its lowest value of $1.7\ ppb$.

The developed LITES sensor employed as sensing element a custom QTF with resonance frequency of $9780.9\ Hz$ and Q-factor of 10340 at atmospheric pressure, respectively. The optimum modulation depth and operating pressure experimentally found were $600\ mVpp$ and $700\ Torr$. The developed LITES sensor showed an excellent linear response ($R^2 = 0.9992$) in the investigated concentration range, with a sensitivity of $0.4\ mV/ppm$. For a concentration of $240\ ppm$ of C_6H_6 in N_2, a LITES peak signal of $96\ mV$ was obtained and a noise level (1σ) of $42\ \mu V$ was measured, resulting in an SNR of 2286 which corresponds to an estimated MDL of $105\ ppb$ with a lock-in time constant of $100\ ms$. Considering an integration time of $30\ s$, the MDL can be lowered to $42\ ppb$.

Future works will be focused on the development of portable QEPAS sensors for VOCs monitoring which can be used for breath analysis applications or which can be mounted on an off-road mobile rover to perform real-time and in situ measurements. Future improvements for the LITES sensor will focus on the use of multipass cells to enhance the light-sample interaction, on the laser sources developments to increase the emitted optical power and on the optimization of optical elements transmittance.